UNIVERSITÀ DEGLI STUDI FIRENZE

DOTTORATO DI RICERCA IN

ATOMIC AND MOLECULAR PHOTONICS

CICLO XXVIII

COORDINATORE Prof. Roberto Righini

Liquid crystals in woodpile photonic crystals: fabrication, numerical calculation and measurement

Relatori

Prof. Diederik Wiersma

Prof. Kestutis Staliunas

Candidata

Chih-Hua Ho

Anni 2012/2016

Liquid crystals in woodpile photonic crystals: fabrication, numerical calculation and measurement

---

A thesis submitted for the degree of Doctor of Philosophy in Physical Science of

Chih-Hua Ho

Supervisors:

Prof. Diederik S. Wiersma

Prof. Kestutis Staliunas

PhD in Atomic and Molecular Photonics
&
Departament de Física i Enginyeria Nuclear

Firenze, November 2015

UNIVERSITAT POLITÈCNICA DE CATALUNYA
BARCELONATECH

European Laboratory for Non-Linear Spectroscopy

將此篇畢業論文獻給天上的阿公，

您的道德典範與樸實性格將永遠烙印在我們心中

Contents

Preface III
Acknowledgements IV
Abstract V
PhD contribution list VI

Chapter 1 Light in woodpile photonic crystals 1
1.1 Properties of photonic crystal in general 2
1.1.1 Geometry of photonic crystal 2
1.1.2 Chromatic dispersion – frequency bandgap 4
1.1.3 Spatial dispersion – angular bandgap 5
1.1.4 Realization of woodpile photonic crystal – two photon lithography 6
1.1.5 Photonic crystals in nature 10
1.2 Analytical methods 12
1.2.1 Maxwell equations for electromagnetic waves 12
1.2.2 Plane wave expansion 13
1.2.3 Finite-difference time-domain 16
1.3 Anomalous diffraction and refraction 19
1.3.1 Negative refraction, flat-lensing and super-prism 19
1.3.2 Negative diffraction and self-collimation 21
1.3.3 Spatial filtering 23
1.4 Summary 27
Chapter 2 Light in liquid crystals 32
2.1 Properties of liquid crystal in general 32
2.1.1 Chemical structures and phase transition 32
2.1.2 Birefringence 36
2.1.3 Surface anchoring and liquid crystals alignment 37
2.1.4 Liquid crystals interaction with external field 38
2.2 Temperature dependence 43
2.2.1 General equations as function of temperature 43
2.2.2 Applications of thermal effect 44
2.3 Polarization and wavelength dependence 46
2.3.1 General equations as function of wavelength 46

2.3.2 Polarized optical microscopy 47
2.3.3 Polymer-Dispersed Liquid Crystals (PDLC) and related applications..... 49
2.4 Elastic and mechanical property – liquid crystalline elastomers 52
2.4.1 Configurations of Liquid Crystalline Elastomer (LCE) 52
2.4.2 Advanced functions of LCE and related stimulation 53
2.5 Summary 55
Chapter 3 Light controlled by LC infiltrated PhC 58
3.1 Introduction to numerical methods and experiment 59
3.1.1 Numerical methods 59
3.1.2 Experiment process – woodpile fabrication 64
3.1.3 Experiment process – infiltration 65
3.1.4 Experiment process – measurement setup 66
3.2 Switching controlled by external heating 67
3.2.1 Thermal control 67
3.2.2 Experiment results 68
3.3 Switching controlled by extra beam 74
3.3.1 Review of optical control 74
3.3.2 Experiment results 74
3.3.3 Numerical calculations 79
3.4 Nonlinear effect controlled by single beam (self-collimation) 85
3.4.1 Review of single beam nonlinear effect 85
3.4.2 Experiment results 86
3.4.3 Numerical calculations 91
3.5 Summary 98
Chapter 4 Conclusion 101
4.1 Future work – controlled by deformation 102

Preface

The work of my PhD project during the period September 12th 2012 – February 28th 2016 is presented in this thesis.

Most of the work was performed at LENS - European Laboratory for Non-Linear Spectroscopy, Università degli Studi di Firenze (UniFI), Italy. A six months research visit was implemented at Universitat Politècnica de Catalunya (UPC), Spain.

The project is mainly supported by the Erasmus Mundus Doctorate Program Europhotonics (Grant No. 159224-1-2009-1-FR-ERA MUNDUS-EMJD) for 3 years and also financed by ICTP - International Centre for Theoretical Physics (TRIL - Training and Research in Italian Laboratories) for 6 months. The project is supervised by:

- Diederik Wiersma, Professor, LENS, Università degli Studi di Firenze, Firenze, Italy
- Kestutis Staliunas, Professor, UPC, Universitat Politècnica de Catalunya, Barcelona, Spain

Acknowledgements

Firstly, I would like to thank Prof. Diederik Wiersma and Prof. Kestutis Staliunas for giving me the opportunity to join EMJD program between LENS and UPC as a PhD student and for their patient guidance during the whole project. I am deeply indebted to Prof. José Trull and Prof. Crina Cojocaru, who supervised the cooperative work at UPC, for the valuable time they spent on helping me with the equipment in the lab. I would like to express my sincere appreciation to researchers Prof. Piotr Wasylczyk from University of Warszaw, Dott.ssa Camilla Parmeggiani and Dott. Matteo Burresi from LENS of their scientific insights from time to time during my PhD.

Secondly, thanks to the creative and hardworking colleagues Dott.ssa Sepideh Zakeri, Dott. Mupparapu Rajeshkumar, Dott. Romolo Savo, Dott. Filippo Pratesi, Dott. Daniele Martella, Dott. Assegid Flatae, Dott. Anjani Kumar Tiwari, Giacomo Cerretti, Sara Nocentini, Lorenzo Cortese, Lorenzo Pattelli, Francesco Utel, Dmitry Nuzhdin, and Łukasz Zinkiewicz for the time working together at LENS and the care upon daily life. Also I would like to show my thankfulness to the warm-hearted and efficient colleagues Dott.ssa Lina Maigyte, Dott. Vytautas Purlys, Shubham Kumar, Waqas Ahmed, Prof. Ramon Herrero and Prof. Muriel Botey for exchanging their experiences upon doing research at UPC. Special thanks to Mr. Mauro Giuntini for his detailed instructions on electronics. Also to Prof. Francesco Saverio Cataliotti, Prof. Costanza Toninelli, and Prof. Francesca Intonti for their assistance at various angles during my studies. Sincere thanks to Prof. Pi-Gang Luan from National Central University, Prof. Irena Drevenšek Olenik from University of Ljubljana and Prof. Heinz S. Kitzerow from University of Paderborn for proof-reading parts of this thesis and sharing pieces of advice with me.

謝謝連芹、曾瑩、李貝、紫薇、小亮、晶云、梨花、金紅、振超、章顯、胡亮、曾浩、韓爸、萍姐、炳霞、曉云、斐雯、之芸、廖瑩、宜君學姐、怡君、鈺潔、鈺潔媽媽、Milu、Agnieszka Szarkowska、Hania、Tomasz Klay、Karolina Jagodnicka、Valeria Zubieta-Lupo和Marta Cappella在國外生活與工作上的幫助, 因為你們的打氣以及信任, 我才能順利走完博士這條漫漫長路。

Lastly, I would like to thank my parents, grand parents, sisters, and all my friends in Spain, Italy, Taiwan and all over the world, for giving me great encouragement during the past 3.5 years of my PhD. Thanks for your infinite patience and kindness. Thank God for his mercy, grace and guidance on peace, forgiveness and inner balance.

Abstract

Both experimental and numerical studies on Liquid Crystal (LC) infiltrated woodpile Photonic Crystal (PhC) are implemented in this thesis.

The most well-known optical phenomenon of PhC is photonic bandgap (PBG). It is observed either in frequency or in spatial domain. The former means for a chromatic plane wave propagating though PhC that a range of frequencies do not transmit but reflect. The later means for a monochromatic focused beam passing though PhC that certain angular components do not transmit but deflect or reflect.

The most well-investigated optical phenomenon of LC is birefringence. It is due to the strong dielectric anisotropy LC possesses. When the applied stimulations (e.g. electric/ optical field or external heater) are present, the orientation of LC molecules and different refractive indices (e.g. polarization or temperature dependent) are observed. The presence of LC inside PhC not only reduces index contrast (where angular BG appears) but also brings the tunability to such LC-PhC composite device. Therefore band-stop angular filter and sensitive refractometer for liquid material are potential applications controlled by multiple external stimulations.

In this thesis, the related physical properties of PhCs and LCs are introduced beforehand. The fabrication of woodpile PhC is also demonstrated. Direct Laser Writing lithography technique is adopted to build microstructures with high resolution up to hundreds of nanometers. A tunable band-stop filter controlled by polarization and temperature is investigated in linear regime. To bridge our investigation to nonlinear regime, dye-doped LC is used to create graded indices inside LC medium corresponding to intensity. Numerical calculations are conducted to the experimental observations.

To sum up, LC-PhC composite device possesses very promising features as demonstrated which could be applied into tunable elements in integrated optical systems and its abundant nonlinear properties remains to be explored carefully.

PhD contribution list

Publications

[1] *"Controllable light diffraction in woodpile photonic crystals filled with liquid crystal", Appl. Phys. Lett.* ***106****, 021113, (2015)*

[2] *"High-Resolution 3D Direct Laser Writing for Liquid-Crystalline Elastomer Microstructures", Adv. Mater.* ***26****, 2319–2322 (2014)*

[3] "*Nonlinear beam propagation in photonic crystals filled with liquid crystal*", *In preparation, (2015)*

Attended Spring/ Summer School, Visit and Workshop

[1] N4E Hybrid Nanophotonics Workshop, Southampton (GB), March 26-27, 2013

[2] Erasmus Mundus Spring School (DE), April 8-10, 2013, Contribution: Poster

[3] Controlling the propagation of waves in complex media, Cargèse (FR), May 27-June 1, 2013

[4] Visit cooperative institute UPV, Valencia (ES), 10-17 June, 2013, Contribution: Presentation

[5] Erasmus Mundus Spring School (FR), March 31-April 3, 2014, Contribution: Poster

[6] Controlling the propagation of waves in complex media, Cargèse (FR), July 1-12, 2014, Contribution: Poster

[7] Erasmus Mundus Spring School (FR), April 13-16, 2015, Contribution: Oral

[8] Conference on Lasers and Electro-Optics (DE), June 21-25, 2015, Contribution: Oral

[9] The 8th International Liquid Crystal Elastomer Conference (IT), October 2-7, 2015, Contribution: Poster

Chapter 1 Light in woodpile photonic crystals

The idea of photonic crystals (PhCs) originated with E. Yablonovitch [1] and S. John [2] in 1987. They proposed and later built an artificial periodic structure from dielectric material at the wavelength scale. For visible light, the scale is hundreds of nanometers while for microwaves it is centimeters. Actually the first experimental verification of photonic crystals were for microwaves as at that time is completely impossible to build a structure periodically modulated on range of visible light. PhCs are capable to influence light propagation dramatically. Since then the field attracted many researchers to devote themselves into related investigation. One upon the most famous phenomena is the Photonic Band Gap (PBG), which literally means that certain frequencies of light are prohibited to pass through this periodic structure. The concept is comparable to the electronic band gap in semiconductor physics. PBG is a chromatic effect in temporal domain, while in spatial domain very interesting new phenomena were discovered, like angular beam steering [3], near field focusing [4] and self-collimation [5], which have been intensively explored for recent decades. This chapter is denoted to overview of these peculiar wave propagation phenomena in photonic crystals.

In this chapter, we begin with a brief overview of general properties and geometries of PhCs of different dimensions. Woodpile structure for instance is one simple realization of three-dimensional PhC. We will overview different fabrication techniques, for instance two-photon lithography technique is now broadly used to produce various periodic prototypes.

Secondly we introduce simple theory based on the fundamental Maxwell's equations for electromagnetic wave. Based on these wave equations, plane-wave expansion (PWE) and finite-difference time-domain (FDTD) method are presented as numerical tools individually. PWE is typically used for calculation of frequency band gaps in while FDTD is applied for simulation of evolution of waves in specific systems.

To end up this chapter, several fascinating effects like spatial filtering, flat-lensing and

super-collimation caused by anomalous diffraction and refraction are demonstrated. These effects are strongly related to the contribution upon wave front modulation of PhCs for light propagation as discussed in forepart.

1.1 Properties of photonic crystal in general

1.1.1 Geometry of photonic crystal

Photonic crystals are artificial materials with periodic refractive index distribution on optical scale. Several designs of the periodic structures such as one-dimensional multi-layer structure, two-dimensional array of cylinders, and fully three-dimensional arrangement of spheres in different dimensions are presented below in Fig 1.1.1-1.

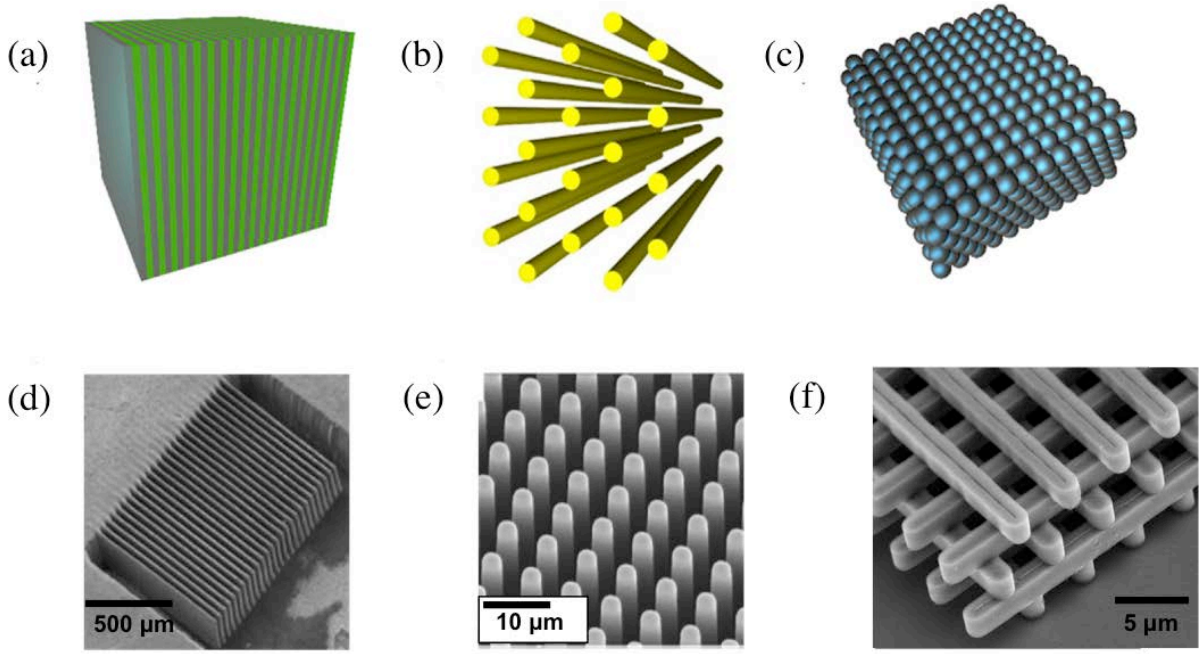

Fig 1.1.1-1 Schematics of 1D, 2D and 3D PhC design (a-c) [6], SEM images of real multi-layers [7], parallel rods [8], and woodpile periodic structures [9] (d-f).

To characterize the light propagation in these complex periodic systems, a few important parameters are introduced in advance: lattice constant a, filling factor f, and permittivity ε. The former means the repeating distance between each lattice point. The filling factor f represents how much the surface or volume dielectric rod occupies in the unit cell. The wave

front of propagation beam is modulated due to lattice geometry and band structure of these periodic systems.

Taking 2D PhC as an example, we first introduce two translation vectors $\boldsymbol{a_1}$ and $\boldsymbol{a_2}$ with non-zero angle in between. Lattice constants a_1 and a_2 are the lengths of these vectors. Then a unit cell (parallelogram in this two dimensional case) is composed of these two vectors. By reproducing unit cells in entire plane, we can easily describe a periodic structure with lattice points. Meanwhile the bases $\boldsymbol{b_1}$ and $\boldsymbol{b_2}$ in reciprocal space are defined under the orthogonality condition $\boldsymbol{a}_i \cdot \boldsymbol{b}_j = 2\pi\delta_{ij}$, which implies $\delta_{ij} = 1$ when $i = j$ and $\delta_{ij} = 0$ when $i \neq j$. Several typical lattice distributions in two-dimensional space are depicted in Fig 1.1.1-2. On the other hand, the introduction of longitudinal period $d_{\parallel}$ and transverse period $d_{\perp}$ is also convenient, characterizing longitudinal and transverse distance between adjacent rods along the beam propagation direction.

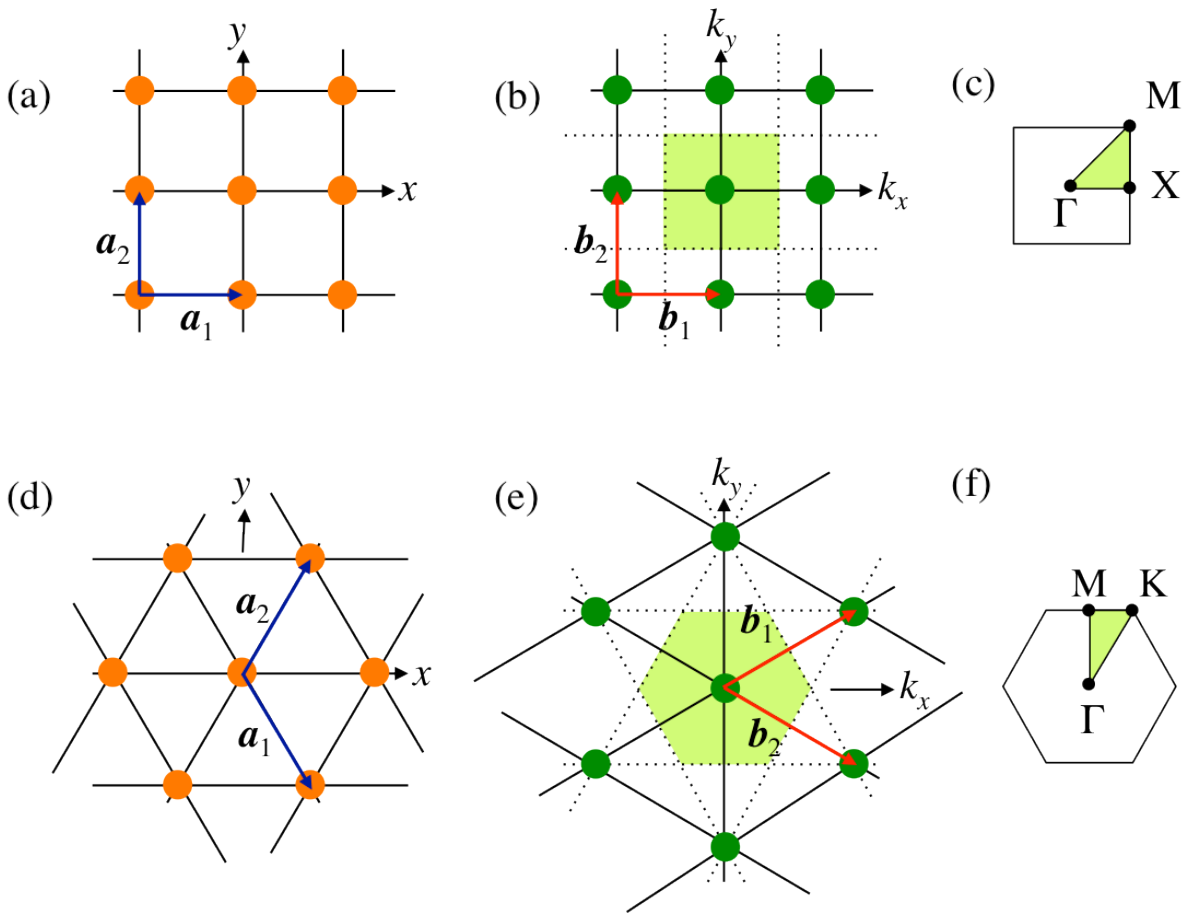

Fig 1.1.1-2 Square lattice (a) and triangular lattice (d) in real space, the corresponding reciprocal lattice (b) and (e) in *k* space, and the corresponding irreducible Brillouin zones (c) and (f).

Apart from the periodicity of lattice, when allocating dielectric rods upon these lattice points the properties of the individual scatterers are also important. Filling factor f is defined according to the area of a scatterer comparing to the area a unit cell of 2D PhC. For example, the filling factor for the dielectric rods with radius r in square lattice distribution is:

$$f_{\square} = \frac{\pi r^2}{a^2} \tag{1.1}$$

As for triangular lattice distribution,

$$f_{\Delta} = \frac{2\pi r^2}{\sqrt{3}a^2} \tag{1.2}$$

1.1.2 Chromatic dispersion – frequency bandgap

Dated back to 17th century, Newton firstly used prism to expand white light into colorful spectrum and thus discovered dispersion. The velocity of the light propagation in vacuum is constant and does not depend on wavelength (frequency). When light enters a medium, different wave components with different wavelengths propagate with different velocities. This effect is the chromatic dispersion. Rainbow after rain is one common example to be observed in nature. In optical system, chromatic aberration also occurs due to several refractions into many convex or concave lenses. The wavelength dependency of the refractive index of material is so called dispersion relation.

In photonic crystals, the dispersion relation is presented by relation between the photon frequency and wave vector. The emergence of photonic band gap can be linked to multiple scattering inside PhC. While light wave propagates within the periodic structures, each potential well (e.g. dielectric rod or air hole) is regarded as a new scatterer. The light fields before and after bouncing through these scatterers are summed and form the total field. For particular frequencies corresponding to constructive interference for back-reflection, the waves cannot propagate but reflect back. Such stop-band is called frequency bandgap [10]. Furthermore, if the frequency bandgap appears at all incidence angles, it is called complete photonic bandgap [9].

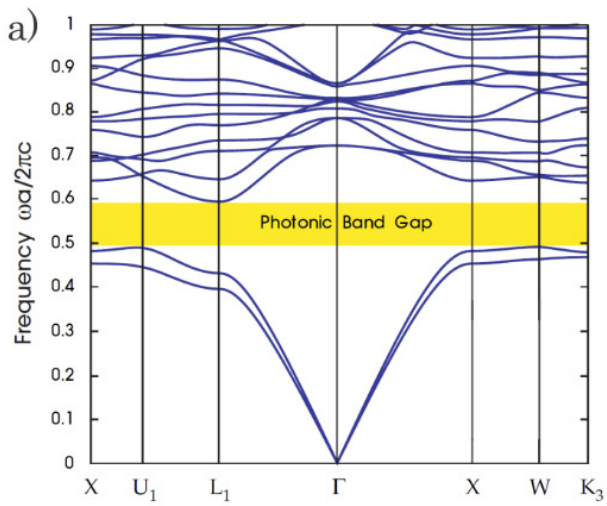

Fig 1.1.2 A complete photonic bandgap produced by a Yablonovite ("diamond like") structure [9]

The first three-dimensional band structure was theoretically calculated by Ho, Chan and Soukoulis in 1990 [11]. They predicted that complete PBG exists in 3D PhC with diamond lattice in face-centered cubic (FCC) geometry. One year later, Yablonovitch experimentally found a complete BG in microwave regime in 3D PhC of diamond-like structure [9]. By drilling the long holes along three lattice vectors of FCC lattice in dielectric medium (also by putting air spheres at lattice points), they were able to construct such diamond-like structure, which was later named Yablonovite.

1.1.3 Spatial dispersion – angular bandgap

In additional to frequency bandgap, another very appealing property of PhC is to shape the propagation of the light beam. H. Kosaka presented spatial dispersion diagram to interpret such beam shaping behavior in 1999 [5]. By taking a projection plane of certain reduced frequencies (usually marked as a/λ or $\omega a/2\pi c$), iso-frequency contours are plotted. The axes k_x and k_z represent the angle dependency of propagation wave. One example is demonstrated in Fig 1.1.3 b. For reduced frequency at 0.3446, light undergoes positive diffraction (like in propagation through usual homogenous media). For the dashed contours, it corresponds to negative diffraction at frequency around 0.5288. This spatial dispersion diagram is feasible for understanding optical phenomena like flat lensing, self-collimation and super prism effect [12]. The shaded areas correspond to angular bandgaps.

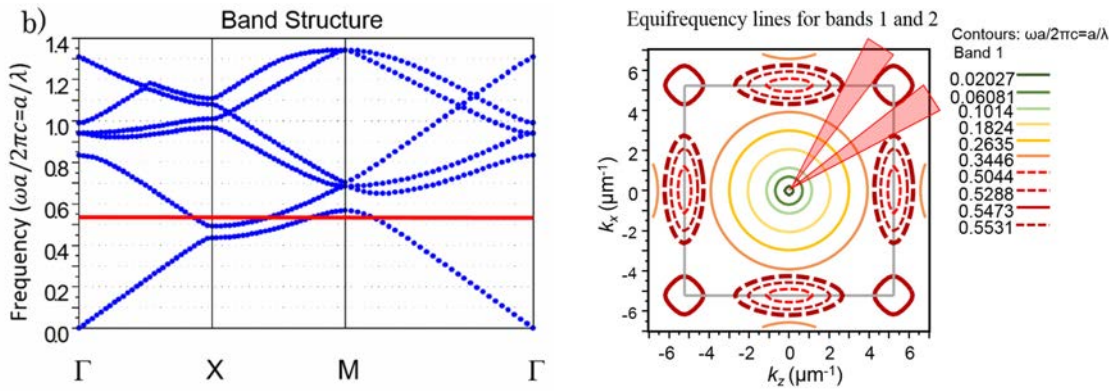

Figure 1.1.3 Band diagram of 2D PhC in 45° rotation of square lattice geometry (a) and iso-frequency contours of both first and second bands (b) [6]

1.1.4 Realization of woodpile photonic crystal – two photon lithography

First three-dimensional crystal, Yablonovite, was made by mechanical means, drilling the holes. This is possible for microwaves, as the holes are of order of mm. For visible (or infrared) the sizes of the holes should be of μm. Therefore only much later, when the fabrication technologies seriously advanced, it becomes possible to fabricate 3D PhC for the visible regime. Such modern technology is mainly based on two photon lithography.

Apart from Yablonovite, 3D PhC with diamond-like FCC geometry, experimentalists also tried so many different approaches with various design and materials to build PhC with broad bandgap. Through micromanipulation and templating, some researchers made diamond inverse opal of silicon [13]. Another approach involving material deposition, electronic-beam lithography, etching and planarization was adopted to create layer-by-layer FCC lattice of air cylinders in silicon [14].

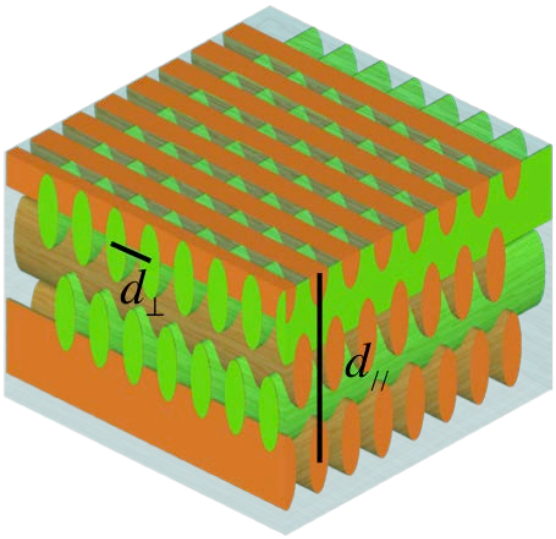

Fig 1.1.4-1 Schematic of one period woodpile photonic crystal

Woodpile structure is a 3D PhC consisting of piles of orthogonal gratings in each neighbor layer. Considering a half-period of the lattice shift in parallel layers, each four-layer arrangement is regarded as longitudinal period $d_{\parallel}$ while the grating interval in plane is regarded as transverse period $d_{\perp}$ of woodpile PhC as shown in Fig 1.1.4-1.

K. M. Ho [15] and H. S. Sözüer [16] predicted the full bandgap from numerical calculation in woodpile PhC in 1994. The corresponding experimental measurements were published afterwards by E. Özbay [17] in the same year. Although their work was realized in microwave regime (10-20 GHz), it presented the potential of scaling down the bandgap location to optical regime via producing smaller period PhC.

Two-photon (2-p) absorption opens a new era for high spatial resolution 3D lithography. Taking advantage from the quadratic dependence on laser intensity, 2-p absorption is confined into a small volume. By doping photon sensitive initiators into resins, the absorptive photons provide the energy to excite the polymerization process. During the process, a designed pattern is locally written into the material and meanwhile makes the exposed part insoluble. After dissolving the unexposed part in material, the 3D designed microstructure remains. In 1999 B. H. Cumpston demonstrated a new initiator with large 2-p absorption cross-sections [18], which opened the possibility to rapidly produce micro-woodpile PhC in optical regime with low cost.

Direct laser writing (DLW) is a micro-fabrication technique based on 2-p absorption. DLW system is composed of control program, ultrafast laser with modulator, focusing objective and 3D translation stage. The profile and power of focused laser beam, the exposure time and the precision of position coordinates determine the accuracy of designed microstructure. An additional optical microscope system is integrated to monitor the writing process as depicted in Fig 1.1.4-2. Advanced equipment such as motorized piezo-stage and galvo mirror enhances dramatically the scanning speed for even larger scanning area with submicron resolution [19]. Being commercialized by Nanoscribe company since 2007, this micro-fabrication technique is widely applied in photonics [20], microfluidics [21], micro-mechanics [22], life science [23] and many other fields.

In Fig 1.1.4-2 a commercial laser writing workstation (Photonic Professional, Nanoscribe GmbH) used in our lab is schematically described. The system is equipped with 780 nm femto second fiber laser of 100 MHz repetition rate of the source. After passing through half wave plate, the linearly polarized beam enters acousto-optic modulator (AOM). Controlled by electric signal, AOM modulates the output power by selecting 1st order diffraction [24]. A telescope fits the adjusting beam profile the aperture of objective. A quarter wave plate is used to provide circular polarization, which helps to eliminate the voxel asymmetry [25]. At the end, as highlighted in blue, the inverse microscope consisting of an autofocus system to focus the beam spot on the substrate surface is placed. The maximum scanning volume of a three-dimensional piezo stage is 300 μm x 300 μm x 300 μm. The writing speed is kept constant 100 μm/s.

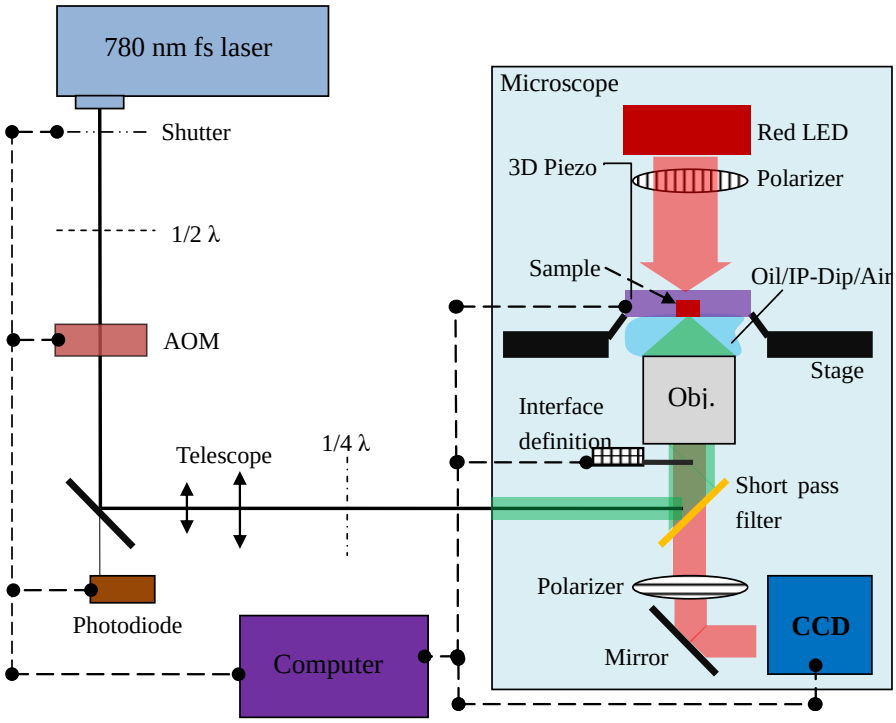

Fig 1.1.4-2 Schematic of DLW system [26]

There are several types of photon-sensitive material, so called photoresist. They are mainly categorized into positive and negative photoresists. The exposed part in positive resists is dissolved while in negative resists remain insoluble during developing process. Produced by Nanoscribe, IP-L, IP-G and IP-Dip are a group of acrylate based negative photoresist commonly used in photonics. IP-L, the liquid like resist, provides high resolution with tight focused beam voxel on the glass-resist interface by refractive index matching. IP-G, the gel like resist, becomes solid after pre-baking process. It is mainly used on top-down construction into the resist. IP-Dip is similar to IP-L but is utilized in an inverse configuration. The configuration not only shows the possibility to fabricate the microstructure of longer size, no more limited to working distance, but also reduces the depth-dependent spherical aberration.

For conventional oil immersion 100X NA 1.4 objective, the height of the designed structure is limited to be less than 40 microns considering objective's working distance and substrate thickness, as the writing direction is from glass-resist interface towards into the resist (i.e. bottom-up construction). In order to build tall woodpile PhC more than of 40 microns height, we used Dip-in Laser Lithography (DiLL) technology developed by Nanoscribe. DiLL technology not only replaces oil with photoresist as immersion medium but also reverses the

glass-resist interface. In this case, to inscribe a structure into resist the writing direction is changed into top-down configuration [Fig 1.1.4-3].

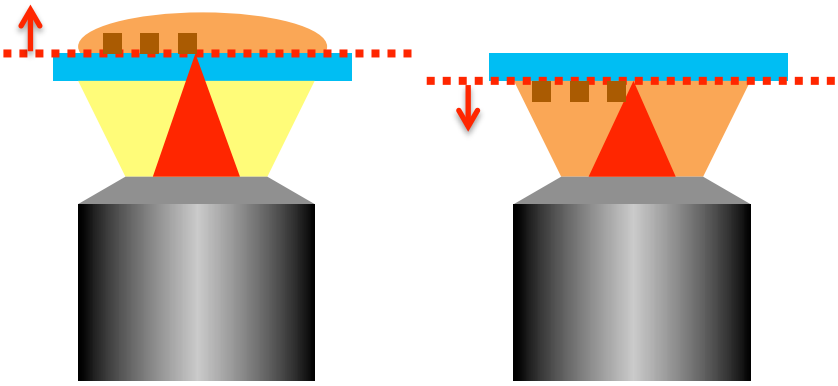

Fig 1.1.4-3 Schematics of conventional oil immersion DLW (a) and photoresist dip-in DLW (b)

1.1.5 Photonic crystals in nature

In addition to delicate artificial microstructures fabricated by lithography technique, scientists also investigate some periodic structures already existing in nature. The iridescence (or structural coloration) due to the periodicities on a wavelength scale appearing in sea mouse, butterfly, beetle and many living creatures is most widely observed phenomenon.

In order to understand basic principles of such structural color effect, a simple model of Bragg mirrors is useful. The Bragg mirror is a structure consisting of alternating layers of different dielectric materials, (e.g. one thin layer of air with refractive index n = 1 and one layer of chitin with n = 1.56). With the corresponding thickness of air and chitin layers, 10nm and 194 nm respectively, the ventral segments of *Chrysochroa vittata* are found to reflect red color for normal incidence while appear green for higher incidence angles [27]. Another related example, as shown in Fig 1.1.5-1, is the hierarchical microstructure on the wing of butterfly *Papilio palinurus*. Several 4 - 10 μm diameter microbowls lined with a multilayer stack of layers of air and chitin result in green color on the wings [28].

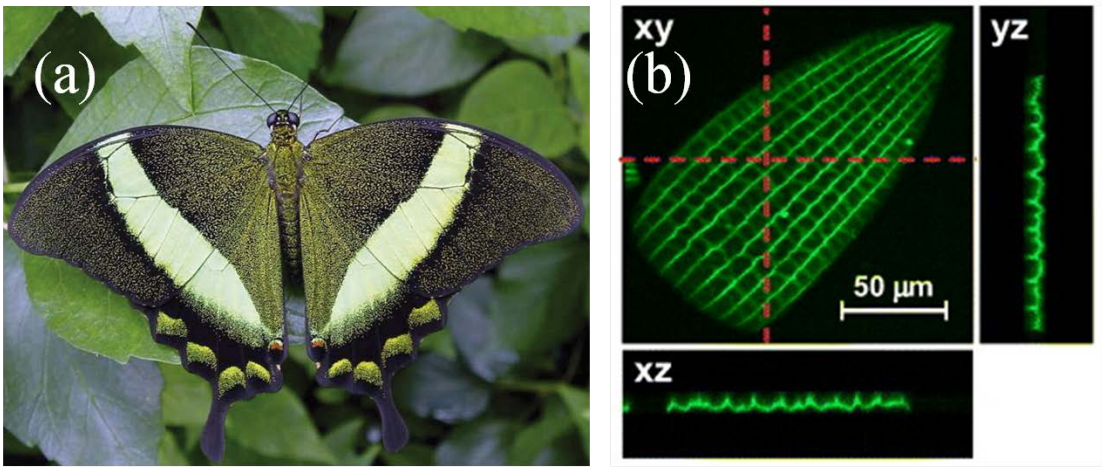

Fig 1.1.5-1 (a) Photo of butterfly *Papilio palinurus* [29] (b), hierarchical microstructure of *Papilio palinurus* in fluorescence reflection mode [30]

In addition to 1D multilayer stack, a pack of cilia arranged in 2D hexagonal structure from the locomotion organs of Ctenophore *Beroë cucumis* is also explored. Despite the low refractive index contrasts with the sea water, by accumulating many layers, the structure is able to reflect wide range of incident light. By varying the diameters of cilia in hexagonal arrangement, the selective color in corresponding reflection angles is possible [31].

Concerning the 3D PhC structure in nature, commonly investigated design upon close-assembling spheres of hydrated silica in FCC or hexagonal lattices, the similar opal microstructure is also found in the weevil *Metapocyrtus*. This periodic design leads to the color scales of the hue nearly the same from all the viewing angles [Fig 1.1.5-2].

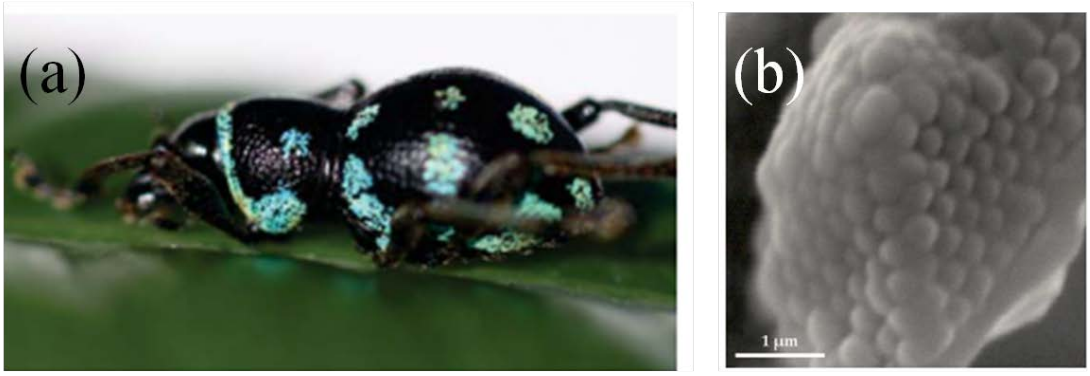

Fig 1.1.5-2 (a) Photo of weevil *Metapocyrtus* [32], (b) SEM of the opal structure and submicron spheres [33]

1.2 Analytical methods

1.2.1 Maxwell equations for electromagnetic waves

The fundamental description of propagation of electromagnetic waves in various media is given by Maxwell's equations. These equations related the electric field **E**, magnetic field **H**, electric displacement **D** and magnetic induction **B**.

$$\begin{aligned} \nabla \cdot \mathbf{D} &= 4\pi\rho_f \\ \nabla \cdot \mathbf{B} &= \mathbf{0} \\ \nabla \times \mathbf{E} &= -\frac{1}{c_{\mathbf{0}}}\frac{\partial \mathbf{B}}{\partial t} \\ \nabla \times \mathbf{H} &= \frac{1}{c_{\mathbf{0}}}\frac{\partial \mathbf{D}}{\partial t} + 4\pi\mathbf{J}_f \end{aligned} \tag{1.3}$$

also the charge density ρ_f, current density $\mathbf{J}_f$, and light speed in vacuum $c_{\mathbf{0}}$. In dielectric materials the charges and current are absent, i.e. $\rho_f = 0$ and $\mathbf{J}_f = 0$.

When light propagates in inhomogeneous but nondispersive medium, the permittivity and permeability are position dependent (i.e. $\varepsilon = \varepsilon(\mathbf{r})$ and $\mu = \mu(\mathbf{r})$) but frequency independent, the Maxwell's equations can be written in the form of the wave equations of **E** field and **H** field:

$$\begin{aligned} \nabla \times \left(\frac{\nabla \times \mathbf{E}}{\mu(\mathbf{r})}\right) + \frac{\varepsilon(\mathbf{r})}{c_0^2}\frac{\partial^2 \mathbf{E}}{\partial t^2} &= 0 \\ \nabla \times \left(\frac{\nabla \times \mathbf{H}}{\varepsilon(\mathbf{r})}\right) + \frac{\mu(\mathbf{r})}{c_0^2}\frac{\partial^2 \mathbf{H}}{\partial t^2} &= 0 \end{aligned} \tag{1.4}$$

When $\varepsilon = \mu = 1$, the (1.4) simply describes the wave propagation in free space. For the 2D system with the electromagnetic waves propagating in *xy* plane, the related parameters $\varepsilon = \varepsilon(x, y)$, $\mu = \mu(x, y)$, $\mathbf{E} = \mathbf{E}(x, y, t)$ and $\mathbf{H} = \mathbf{H}(x, y, t)$ are defined correspondingly. Generally the wave propagation can be decomposed into the superposition of E-polarized (TM) and H-polarized (TE) waves.

For TM wave with electric field $\mathbf{E} = E\hat{\mathbf{z}}$ and any dependence on z: $\partial\mu/\partial z = 0$ and $\partial E/\partial z = 0$,

$$\nabla\times\left(\frac{\nabla\times\mathbf{E}}{\mu}\right) = -\hat{\mathbf{z}}\nabla\cdot\left(\frac{\nabla E}{\mu}\right) \tag{1.5}$$

For TE wave with magnetic field $\mathbf{H} = H\hat{\mathbf{z}}$ and for $\partial\varepsilon/\partial z = 0$ and $\partial H/\partial z = 0$; the similar result is obtained:

$$\nabla\times\left(\frac{\nabla\times\mathbf{H}}{\varepsilon}\right) = -\hat{\mathbf{z}}\nabla\cdot\left(\frac{\nabla H}{\varepsilon}\right) \tag{1.6}$$

Using the relations (1.5) and (1.6), we can further simplify the wave equations (1.4) into:

$$\begin{aligned}\nabla\cdot\left(\frac{\nabla E}{\mu}\right) - \frac{\varepsilon}{c_0^2}\frac{\partial^2 E}{\partial t^2} &= \nabla\cdot\left(\frac{\nabla E}{\mu}\right) - \frac{1}{\mu c^2}\frac{\partial^2 E}{\partial t^2} = 0\\ \nabla\cdot\left(\frac{\nabla H}{\varepsilon}\right) - \frac{\mu}{c_0^2}\frac{\partial^2 H}{\partial t^2} &= \nabla\cdot\left(\frac{\nabla H}{\varepsilon}\right) - \frac{1}{\varepsilon c^2}\frac{\partial^2 H}{\partial t^2} = 0\end{aligned} \tag{1.7}$$

where $c = c_{\mathbf{0}}/\sqrt{\varepsilon\mu}$ means the light speed in medium.

1.2.2 Plane wave expansion

To describe the wave properties in periodic medium like PhC, a band diagram to characterize dispersion relation is essential. Plane wave expansion method is usually used to calculate the band diagram of PhC [34]. According to Bloch's theorem, the propagation modes in PhC can be interpreted as plane waves modulated by periodic medium. They can be related with wave vector $\mathbf{k}$ and the mode frequency $\omega(\mathbf{k})$. The unit of frequency is often normalized into $(\omega a/2\pi c)$ or (a/λ) with lattice constant a for most symmetric (square and triangular) lattices. Here we introduce the calculation of band diagrams for 3D and 2D PhC analytically.

A periodic dielectric medium with permittivity $\varepsilon(\mathbf{r})$ can be described as $\varepsilon(\mathbf{r}+\mathbf{R}) = \varepsilon(\mathbf{r})$, where $\mathbf{R}$ is lattice vector. Such periodic permittivity distribution allows the Fourier decomposition:

$$\varepsilon(\mathbf{r}) = \sum_{\mathbf{G}} \varepsilon(\mathbf{G})\, e^{i\mathbf{G}\cdot\mathbf{r}} \tag{1.8}$$

For a PhC composed of two different materials with dielectric constants ε_a and ε_b, the corresponding areas or volume are marked as A_a and A_b. The total cell areas or volume are $A_c = A_a + A_b$. With these parameters the Fourier coefficient of permittivity reads:

$$\begin{aligned}\varepsilon(\mathbf{G}) &= \frac{1}{A_c}\int_{A_c} \varepsilon(\mathbf{r})\exp(-i\mathbf{G}\cdot\mathbf{r})dA \\ &= \frac{(\varepsilon_a - \varepsilon_b)}{A_c}\int_{A_a} \exp(-i\mathbf{G}\cdot\mathbf{r})dA + \frac{\varepsilon_b}{A_c}\int_{A_c} \exp(-i\mathbf{G}\cdot\mathbf{r})dA\end{aligned} \tag{1.9}$$

Depending on the value of **G**, we can simplify equations as following:

$$\varepsilon(\mathbf{G}) = \begin{cases}(\varepsilon_a - \varepsilon_b)S(\mathbf{G}) & \text{if } \mathbf{G} \neq 0 \\ f\varepsilon_a + (1-f)\varepsilon_b & \text{if } \mathbf{G} = 0\end{cases} \tag{1.10}$$

where $f = A_a/A_c$ is the filling factor and $S(\mathbf{G}) = \frac{1}{A_c}\int_{A_a} \exp(-i\mathbf{G}\cdot\mathbf{r})dA$ is the structure factor [35].

To analyze the band diagram of 3D PhC, for simplicity we consider non-magnetic material ($\mu = 1$):

$$\nabla\times\left[\frac{1}{\varepsilon(\mathbf{r})}\nabla\times\mathbf{H}(\mathbf{r})\right] = \frac{\omega^2}{c^2}\mathbf{H}(\mathbf{r}) \tag{1.11}$$

According to Bloch's theorem, the propagation mode of magnetic field inside PhC can be written as:

$$\mathbf{H}(\mathbf{r}) = \sum_{\mathbf{G}} \mathbf{h}_{\mathbf{G}} e^{i(\mathbf{k}+\mathbf{G})\cdot\mathbf{r}} = \sum_{\mathbf{G}}\sum_{\lambda=1}^{2} h_{\mathbf{G}\lambda}\hat{\mathbf{e}}_\lambda e^{i(\mathbf{k}+\mathbf{G})\cdot\mathbf{r}} \tag{1.12}$$

where $\mathbf{k}$ is Bloch wave vector; The Fourier component $\mathbf{h}_{\mathbf{G}}$ of magnetic field $\mathbf{H}(\mathbf{r})$ is expressed as:

$$\mathbf{h}_{\mathbf{G}} = \sum_{\lambda=1}^{2} h_{\mathbf{G}\lambda}\hat{\mathbf{e}}_{\lambda} \tag{1.13}$$

with basis vectors $\hat{\mathbf{e}}_1 = \hat{\mathbf{e}}_1(\mathbf{k}+\mathbf{G})$ and $\hat{\mathbf{e}}_2 = \hat{\mathbf{e}}_2(\mathbf{k}+\mathbf{G})$ as function of $\mathbf{k}+\mathbf{G}$.

Based on Gauss's Law, here we choose the basis vectors satisfying the conditions below:

$$\hat{\mathbf{e}}_1 \cdot \hat{\mathbf{e}}_2 = (\mathbf{k}+\mathbf{G}) \cdot \hat{\mathbf{e}}_1 = (\mathbf{k}+\mathbf{G}) \cdot \hat{\mathbf{e}}_2 = 0$$
$$\hat{\mathbf{e}}_1 \times \hat{\mathbf{e}}_2 = \frac{(\mathbf{k}+\mathbf{G})}{|\mathbf{k}+\mathbf{G}|} \tag{1.14}$$

By substituting the expressions of permittivity and magnetic field into wave equations, the following equation is obtained:

$$\sum_{\mathbf{G}'} \varepsilon^{-1}(\mathbf{G}-\mathbf{G}')(\mathbf{k}+\mathbf{G}) \times [(\mathbf{k}+\mathbf{G}') \times \mathbf{h}_{\mathbf{G}'}] = -\frac{\omega^2}{c^2}\mathbf{h}_{\mathbf{G}} \tag{1.15}$$

Following the inner product with $\hat{\mathbf{e}}_{\lambda}$, the equation (1.15) converts to:

$$\sum_{\mathbf{G}'} \sum_{\lambda'=1}^{2} \varepsilon^{-1}(\mathbf{G}-\mathbf{G}')[(\mathbf{k}+\mathbf{G}) \times \hat{\mathbf{e}}_{\lambda}] \cdot [(\mathbf{k}+\mathbf{G}') \times \hat{\mathbf{e}}_{\lambda'}]\, h_{\mathbf{G}'\lambda'} = \frac{\omega^2}{c^2}\mathbf{h}_{\mathbf{G}\lambda} \tag{1.16}$$

which can be written in a compact form:

$$\sum_{\mathbf{G}',\lambda'} A_{\mathbf{G}\lambda,\mathbf{G}'\lambda'}\, h_{\mathbf{G}'\lambda'} = \frac{\omega^2}{c^2}\mathbf{h}_{\mathbf{G}\lambda} \tag{1.17}$$

where $A_{\mathbf{G}\lambda,\mathbf{G}'\lambda'} = \varepsilon^{-1}(\mathbf{G}-\mathbf{G}')[(\mathbf{k}+\mathbf{G}) \times \hat{\mathbf{e}}_{\lambda}] \cdot [(\mathbf{k}+\mathbf{G}') \times \hat{\mathbf{e}}_{\lambda'}]$ and can be rewritten in the matrix form $A_{\mathbf{G}\mathbf{G}'} = \varepsilon^{-1}(\mathbf{G}-\mathbf{G}')|\mathbf{k}+\mathbf{G}||\mathbf{k}+\mathbf{G}'| \begin{pmatrix} \hat{\mathbf{e}}_2 \cdot \hat{\mathbf{e}}_{2'} & -\hat{\mathbf{e}}_2 \cdot \hat{\mathbf{e}}_{1'} \\ -\hat{\mathbf{e}}_1 \cdot \hat{\mathbf{e}}_{2'} & \hat{\mathbf{e}}_1 \cdot \hat{\mathbf{e}}_{1'} \end{pmatrix}$.

From the equation (1.17), an eigenvalue problem can be formulated. Since $\varepsilon^{-1}(\mathbf{r})$ is real, it satisfies $\varepsilon^{-1}(\mathbf{G}'-\mathbf{G}) = \left(\varepsilon^{-1}(\mathbf{G}-\mathbf{G}')\right)^*$ which implies that $A_{\mathbf{G}'\lambda',\mathbf{G}\lambda} = A^*_{\mathbf{G}\lambda,\mathbf{G}'\lambda'}$ is a Hermitian matrix. The eigenvalues $\omega^2_{\mathbf{k}}$ are real and the eigenvectors are orthogonal. A band diagram for 3D PhC is obtained by solving the eigenvalue problem.

To calculate band diagram for 2D PhC is relatively simple. Concerning lack of z component for $\mathbf{k}+\mathbf{G}=(k_x+G_x)\hat{\mathbf{x}}+(k_y+G_y)\hat{\mathbf{y}}$, we assume $\hat{\mathbf{e}}_1=\hat{\mathbf{e}}_{1'}=\hat{\mathbf{z}}$. Since $\hat{\mathbf{e}}_2$ and $\hat{\mathbf{e}}_{2'}$ lay on *xy* plane, the inner product of basis vectors $\hat{\mathbf{e}}_1\cdot\hat{\mathbf{e}}_{2'}=\hat{\mathbf{e}}_{1'}\cdot\hat{\mathbf{e}}_2=0$ is obtained. Under such precondition, we can use scalar form to interpret wave properties:

$$A_{\mathbf{GG}'}=\begin{pmatrix} A^H_{\boldsymbol{GG}'} & 0 \\ 0 & A^E_{\boldsymbol{GG}'} \end{pmatrix} \tag{1.18}$$

where $\mathrm{A}^{\mathrm{E}}_{\mathrm{GG}'}=\varepsilon^{-1}(\mathrm{G}-\mathrm{G}')|\mathrm{k}+\mathrm{G}||\mathrm{k}+\mathrm{G}'|$ and $\mathrm{A}^{\mathrm{H}}_{\mathrm{GG}'}=\varepsilon^{-1}(\mathrm{G}-\mathrm{G}')(\mathrm{k}+\mathrm{G})\cdot(\mathrm{k}+\mathrm{G}')$.

By solving the eigenvalue problem of $\mathrm{A}^{\mathrm{E}}_{\mathrm{GG}'}$ and $\mathrm{A}^{\mathrm{H}}_{\mathrm{GG}'}$, a 2D PhC band diagram for TM and TE waves is obtained respectively [10].

1.2.3 Finite-difference time-domain

Apart from understanding wave propagation properties in wavevector-frequency domain, it is also possible to solve and to follow the full field propagation in time domain. Finite-difference time-domain method is therefore introduced [36]. FDTD is widely used to simulate the time evolution of waves in dielectric, metallic or plasma materials. This method is suitable to calculate the electromagnetic field in either periodic or non-periodic system.

Beginning with Ampere's law and Faraday's law in Maxwell's equations [37]:

$$\begin{aligned} \nabla\times\mathbf{H}&=\frac{\partial\mathbf{D}}{\partial t}+\mathbf{J}_e=\varepsilon\frac{\partial\mathbf{E}}{\partial t}+\sigma\mathbf{E} \\ \nabla\times\mathbf{E}&=-\frac{\partial\mathbf{B}}{\partial t}-\mathbf{J}_m=-\mu\frac{\partial\mathbf{H}}{\partial t}-s\mathbf{H} \end{aligned} \tag{1.19}$$

where $\mathbf{J}_e$ is electric current source and $\mathbf{J}_m$ is magnetic current source. The introduction of magnetic current source is for calculation convenience, despite the non-existence of magnetic monopole (i.e. $\mathbf{J}_m=0$).

The Maxwell's equations in rectangular coordinate system can be expanded into:

$$(\nabla\times\mathbf{H})\cdot e_i = \left(\varepsilon_o\varepsilon_r\frac{\partial}{\partial t}+\sigma\right)E_i$$
$$(\nabla\times\mathbf{E})\cdot e_i = -\left(\mu_o\mu_r\frac{\partial}{\partial t}+s\right)H_i \tag{1.20}$$

where σ is conductivity, s is magnetic conductivity and e_i is the unit vector with $i \in \{x, y, z\}$.

Since both magnetic and electric fields possess translation invariance along z axis (i.e. $\partial f/\partial z = 0$) for 2D PhC, we are able to decompose them into TM and TE modes. For TM wave ($H_z = 0$ and $E_x = E_y = 0$), the wave equations read:

$$\frac{\partial H_y}{\partial x}-\frac{\partial H_x}{\partial y} = \left(\sigma+\varepsilon_o\varepsilon_r\frac{\partial}{\partial t}\right)E_z$$
$$\frac{\partial E_z}{\partial y} = -\left(s+\mu_o\mu_r\frac{\partial}{\partial t}\right)H_x \tag{1.21}$$
$$\frac{\partial E_z}{\partial x} = \left(s+\mu_o\mu_r\frac{\partial}{\partial t}\right)H_y$$

While for TE wave ($E_z = 0$ and $H_x = H_y = 0$), the wave equations read:

$$\frac{\partial E_x}{\partial y}-\frac{\partial E_y}{\partial x} = \left(s+\mu_o\mu_r\frac{\partial}{\partial t}\right)H_z$$
$$\frac{\partial H_z}{\partial y} = \left(\sigma+\varepsilon_o\varepsilon_r\frac{\partial}{\partial t}\right)E_x \tag{1.22}$$
$$\frac{\partial H_z}{\partial x} = -\left(\sigma+\varepsilon_o\varepsilon_r\frac{\partial}{\partial t}\right)E_y$$

For numerical calculation, it is necessary to transform the differential equations into difference equations. The time and space domain are divided into steps and into grid points. If the time step and space grid is fine enough, the calculation results are very close to the results from the differential case with acceptable error.

Assume $f(x,y,z,t)$ is any function (either electric or magnetic field) after discretization, the time and space domain can be denoted by an integer n and a set of integer (i,j,k) respectively:

$$f^n(i,j,k) = f(idx, jdy, kdz, ndt) \tag{1.23}$$

The discretization of the partial derivatives of $f(x,y,z,t)$ with respect to time and to space is listed below:

$$\begin{aligned}
\frac{\partial f(x,y,z,t)}{\partial x} &= \frac{f^n(i+1/2\,,j,k) - f^n(i-1/2\,,j,k)}{dx} \\
\frac{\partial f(x,y,z,t)}{\partial y} &= \frac{f^n(i,j+1/2\,,k) - f^n(i,j-1/2\,,k)}{dy} \\
\frac{\partial f(x,y,z,t)}{\partial z} &= \frac{f^n(i,j,k+1/2) - f^n(i,j,k-1/2)}{dz} \\
\frac{\partial f(x,y,z,t)}{\partial t} &= \frac{f^{n+1/2}(i,j,k) - f^{n-1/2}(i,j,k)}{dt}
\end{aligned} \tag{1.24}$$

With the idea of transforming differential equations into difference form, K. S. Yee proposed Yee lattice model in 1966: every electric field component is surrounded by magnetic field components and each magnetic field component is surrounded by electric field components as illustrated in Fig 1.2.3 [38].

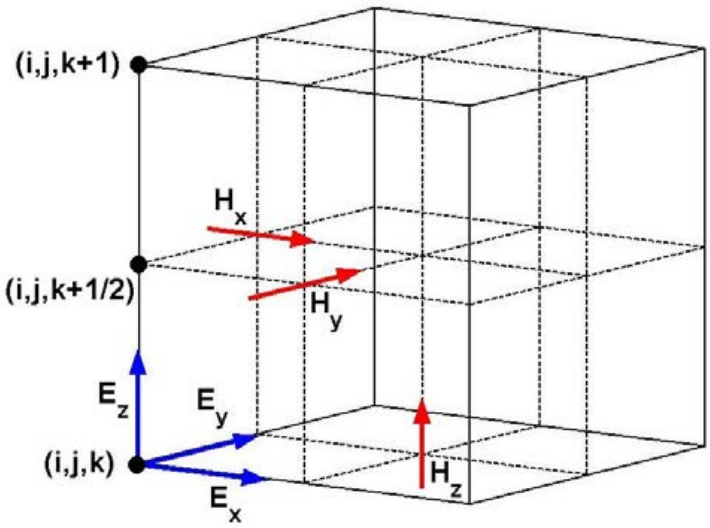

Fig 1.2.3 The grid points of electric and magnetic field components from Yee lattice [37]

Concerning the stability of time evolution of electromagnetic waves and tolerable error, the grid size *dx* in space and the time step *dt* are required to satisfy the following constraints [39]:

$$dx \leq \frac{\lambda}{20} \tag{1.25}$$

$$dt \leq \frac{1}{c}\left[\left(\frac{1}{dx}\right)^2 + \left(\frac{1}{dy}\right)^2 + \left(\frac{1}{dz}\right)^2\right]^{-1/2} \tag{1.26}$$

where λ is source wavelength and *c* is wave speed in medium.

1.3 Anomalous diffraction and refraction

1.3.1 Negative refraction, flat-lensing and super-prism

Using Snell's law in ray optics, one can describe the bending of light (due to velocity variance) at the interface between two media with different index of refraction. A simple relation holds: $n_1 sin\theta_1 = n_2 sin\theta_2$. A common example is observing fish in the river: the real location of a fish is always deeper than its virtual image. Commonly when the incident and the refraction angles at different sides of the surface are of the same sign, it is called positive refraction (or normal refraction). When the incident and the refraction angles are of different sign (one goes to the right, other to the left), it is called negative refraction (one type of anomalous refraction, NR). The special phenomena based on negative refraction such as super-prism and flat-lensing are observed in PhCs.

The negative refraction occurs mainly in two separate situations. In the first case in dielectric structures, the NR appears at the band gap edge of particular dispersion relation to produce negative slopes of iso-frequency lines [40] [41] [42]. To create such particular iso-frequency curve, the lattice constant is close to the scale of incident wavelength. As illustrated schematically in Fig 1.3.1-1, when the transverse projection of wave vector becomes large enough, the group velocity in PhC is distorted and redirected with the iso-frequency curve of

PhC. Therefore the positive (normal) refraction appears at small angles of incidence while the negative refraction (anomalous) shows up at large angles of incidence.

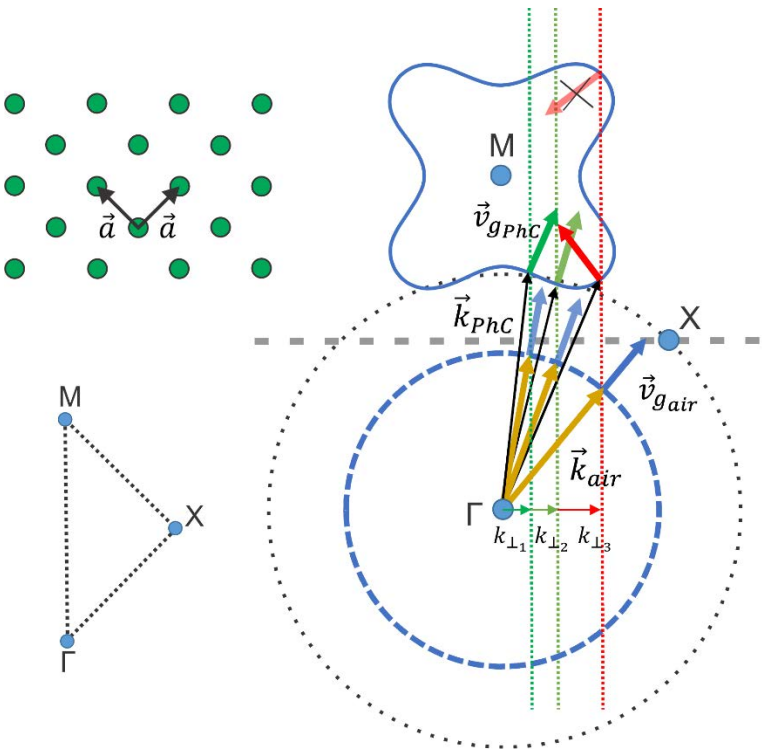

Fig 1.3.1-1 Particular iso-frequency curve for 2D PhC with square lattice geometry and the appearance of negative refraction at large angle of incidence[6]

Another situation where negative refraction can occur is the artificial metallic structures (meta structures) consisting of artificial electric and magnetic dipole resonators. Light propagation in such left-handed materials features in opposite propagations of wave vector and energy flow as shown in Fig 1.3.1-2. When the wavelength of incident beam are much larger than the size and distance between these artificial electric and magnetic dipoles (i.e. it satisfies long wavelength limit), the PhC is described as effective medium with negative permittivity and permeability which leads to negative refractive index, i.e. $n_{eff} = \sqrt{\varepsilon}\sqrt{\mu} < 0$ [43] [44].

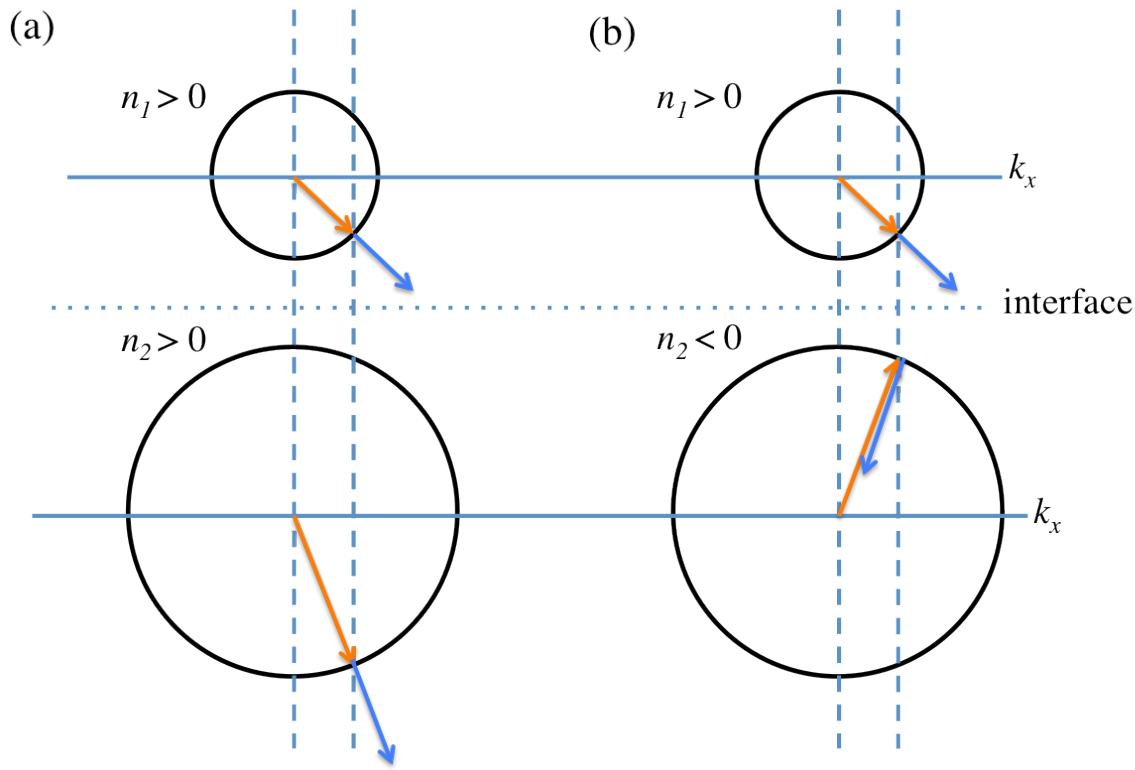

Fig 1.3.1-2 Iso-frequency curves for (a) positive refraction with wave vector (orange arrow) and energy flux (blue arrow) heading in the same direction (b) case of negative refraction with wave vector and energy flux heading in the opposite directions

1.3.2 Negative diffraction and self-collimation

When light propagates into a homogeneous medium, it spreads and diverges. In order to minimize the spatial dispersion after propagating certain distance and also to align light into particular direction, an optical collimator is needed. The simplest example to interpret the idea of collimation is by putting a light bulb at the focal length of a convex (positive) lens. In ray optics, the ray tracks are corrected from off-axis into parallel (to the optical axis) direction. While in wave optics, the concave wave fronts are gradually flattened out.

It is common to apply the concept of collimation in examining laser alignment in optical system as well, e.g. shearing interferometer. Composed of a wedged optical flat, a diffuser as monitor screen and a reference line, a shear interferometer can create graded optical path difference between the two reflections from front (first) and back (second) surfaces of the

optical flat. If the light is well aligned into plane-wave, the overlapping area of the first and second reflected beam appears parallel interference fringes to the optical axis. While for the case of diverging or converging beams, the interference fringes tilt into off-axis direction.

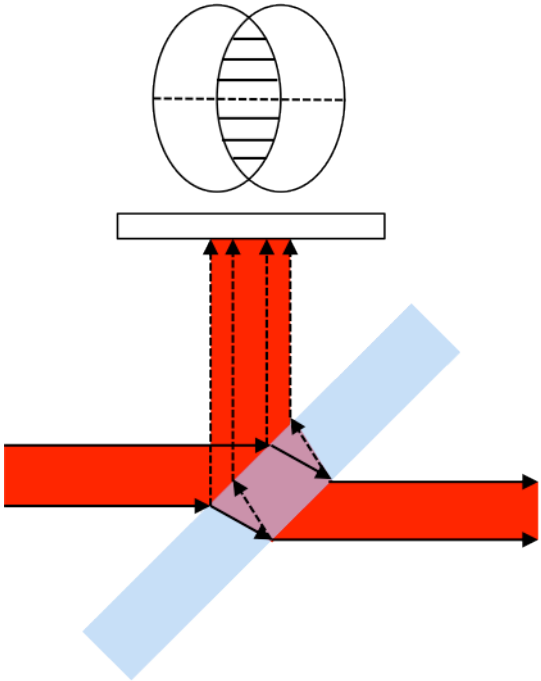

Fig 1.3.2-1 A side view of shear interferometer and a top view of the interference fringes appearing on the screen

The self-collimation can be interpreted through the concept of non-diffractive propagation [45]. Differently from the normal diffraction in homogeneous medium (i.e. diffractive broadening of light beams), non-diffractive propagation literally means light propagation without expansion in transverse direction. When a monochromatic beam propagates through homogeneous material, it leads to curving of wave fronts as the iso-frequency curve for diffractive medium is concave. However, with proper design of the PhCs (functioning as collimator), it is possible to modify iso-frequency curves and make the wave fronts not spreading through propagation.

Fig 1.3.2-2 illustrates the corresponding iso-frequency curves for positive, zero and negative diffraction. In the case of zero diffraction, the normal concave surface is shaped into flat plane, which implies all the wave vectors of incident beam have equal projection on propagation axis. For physics point of view, the phase delay does not appear between different angular components and the beam propagates as a plane wave without any changes. In the case of negative diffraction, the concave surfaces are modified into convex ones, which means that the projection for the on-axis wave vectors is even smaller than off-axis ones. Such negative

diffraction caused by PhC gives the opposite dephasing of the components of propagating beam. The flat-lensing effect experimentally observed [46] is due to the above described mechanism.

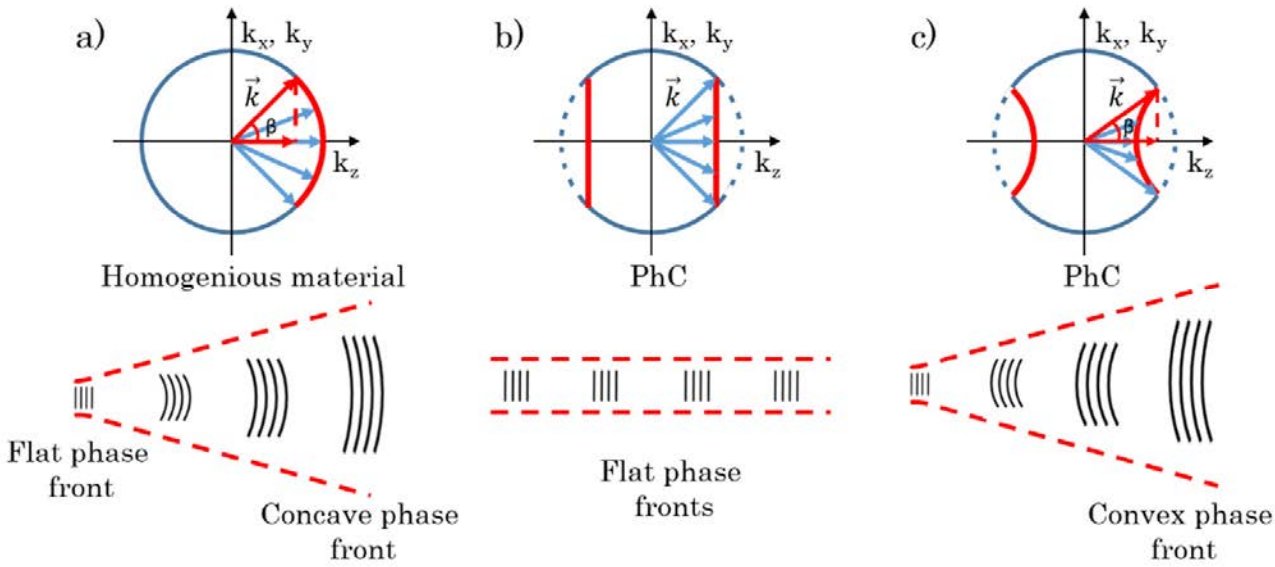

Fig 1.3.2-2 the iso-frequency curves in wave-vector domain and the shape of wave fronts in real space for positive (a), zero (b) and negative (c) diffraction respectively [6]

The realizations of self-collimation based on PhCs have been done both numerically [5] [45] and experimentally [47]. Several advanced designs are also presented for beam bending [48], splitting [49] and routing [50]. By truncating the PhC along $\Gamma - \mathrm{X}$ direction (where k_x lying outside of iso-frequency curve for air appears), a total internal reflection occurs for a self-collimated beam propagating along $\Gamma - \mathrm{M}$ direction [48]. Moreover, by creating a tiny air trench with diverse thickness inside bulk of PhC, it can function as a beam slitter with different transmission and reflectance ratios [50].

1.3.3 Spatial filtering

If the complex light field distribution is Fourier analyzed, the spatial Fourier components (or angular components) can be considered as plane waves traveling in different directions [51]. The low spatial frequencies correspond to the wave vectors propagate in small angles to the optical axis while the high spatial frequencies correspond to the wave vectors propagate in

large angles. The spatial filtering is practically realized by adding a slit or an iris in the focal plane to pass certain range of angular components.

Generally spatial filtering can be classified into low-pass, high-pass and band pass filtering. The low-pass filter blocks large angular components and allows small angular components to pass. The high-pass filter is the opposite, which allows large angular components to propagate while prohibits small angular components to pass. The band-pass filter refers to allowing certain ranges of angular components to pass while the rest ones being blocked. The inverse band-pass (or band-stop) filter, on the contrary, refers to blocking a range of angular components while letting the rest pass. A simple schematic is presented in Fig 1.3.3-1.

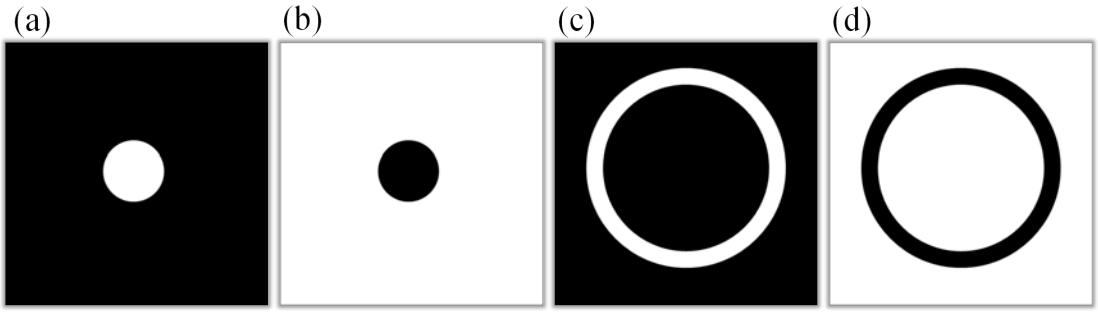

Fig 1.3.3-1 Schematics of low-pass (a), high-pass (b), band-pass (c) and band-stop (d) filters

A fundamental example to demonstrate spatial filtering is by inserting horizontal or vertical slit as done by Abbe in 1893 and Porter in 1906. The experiment is composed of a grid as object, a convex lens, light source and a slit. If we put a slit horizontally, the image is formed by the vertical structure of the grid. While by rotating slit 90°, we are able to observe the horizontal structure of the grid in the image.

In the optical regime, the spatial filtering can be achieved by photonic crystals in more sophisticated way, see the recent review of PhC spatial filtering [52]. Derived from the Bragg condition and transfer matrix method, 1D PhC multilayer structure can function like band-pass spatial filter (assembling upon prism) [53] or omnidirectional and multiple channeled filter (containing a defect layer with negative refractive index) [54]. The mechanism is mainly based on the destructive interference between the propagating beam and multiple reflections of the incident beam. A common type of multilayer film, quarter-wave stack with thickness of each layer equal to a quarter of effective wavelength in the dielectric media. Since the midgap frequency and the reflected waves from every single layer are in phase, the gap-midgap transmission is maximized.

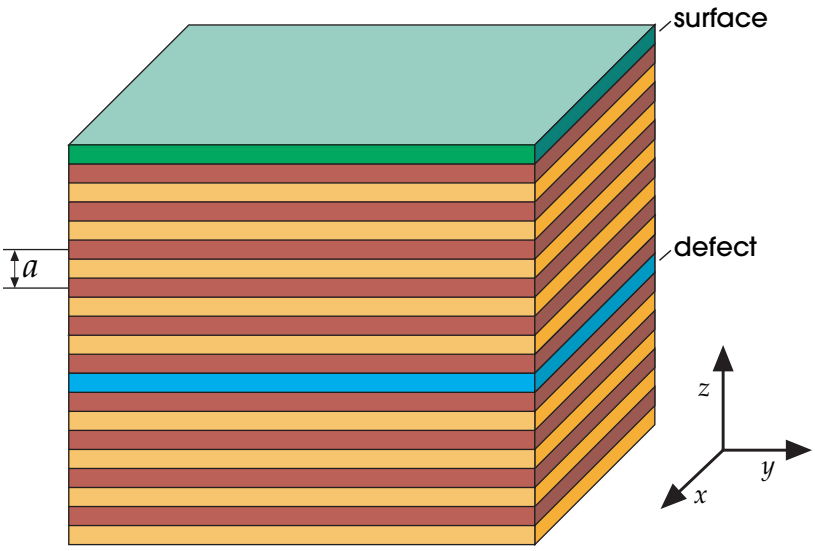

Fig 1.3.3-2 Schematic of 1D PhC multilayer film with a layer of defect [9]

Unlike multilayer films, which do not possess periodic dielectric regions in the off-axis direction, the 2D PhC structure is often more practical to open a wide angular band gap. By arranging high-contrast dielectric rods in symmetry of 2D square lattice, scientists have demonstrated sharp switching between wide-angle ranges ($\theta > 20°$) of total transmission and reflection, i.e. a potential candidate for band-pass and band-stop filters [55]. Extended experimental work is presented afterwards [56]. Compared with simulation results of plane-wave and Gaussian-beam excitations, horn-antenna excitation of microwave regime is employed in experiment. The angular band gap opens at incidence angles ranging from 20° - 30° [Fig 1.3.3-3 (b)].

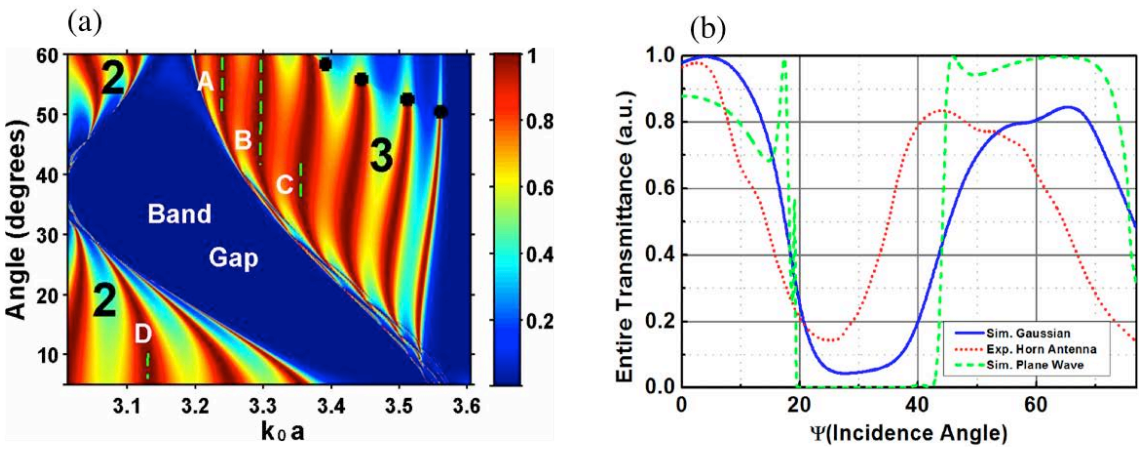

Fig 1.3.3-3 (a) Zero-order transmittance of 2D dielectric PhC in square lattice symmetry with the corresponding parameters: d/a = 0.4, $\varepsilon_r = 11.4$, $\varepsilon_h = 1$ and N = 8, where a is lattice vector, d is diameter of rods, ε_r and ε_h

are permittivity of rod and host medium, N is number of rod layers. The dashed vertical lines relate to $T \approx 1$ [55] (b) Transmittance for various excitations at the same frequency f = 21.763 GHz ($a/\lambda = 0.5078$): Gaussian-beam (solid blue), plane-wave (dashed green) from simulation, and horn-antenna (dotted red) from experiment. The corresponding parameters are $\varepsilon_r = 9.61$, d = 3.1 mm, a = 7 mm and N = 8 [56]

Considering the required size of longitudinal period (the order of wavelength), generally to observe the spatial filtering in optical regime for instance, for visible light frequencies is not an easy task. The experiment discussed above (with angular band gap 20° - 30°) is in microwave regime, it is hardly practical for technology implementation. Therefore a gapless configuration for spatial filtering proposed [57] seems to be more suitable for visible optics. In Fig 1.3.3-4, the iso-frequency diagram for spatial filtering with and without angular band gaps, i.e. gapless filtering, are illustrated respectively.

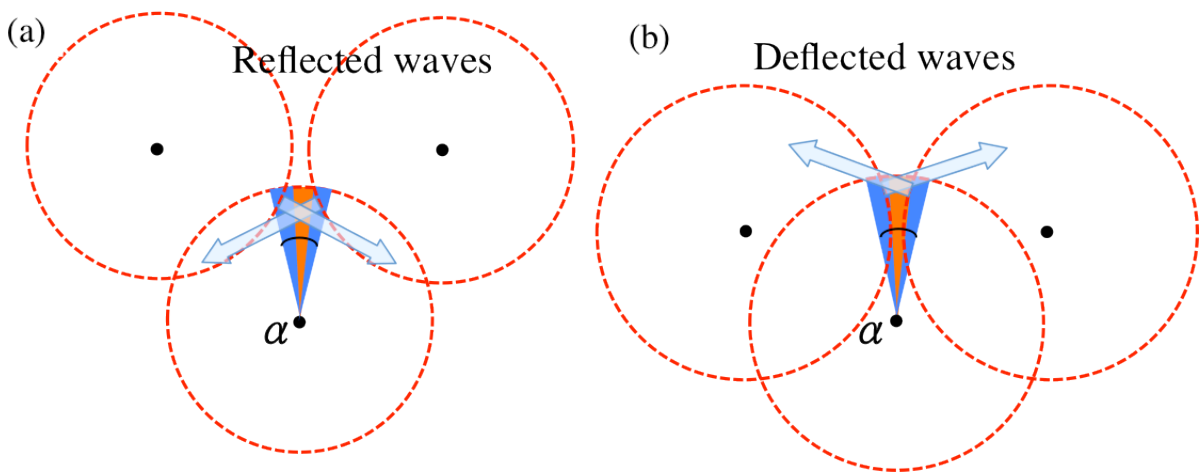

Fig 1.3.3-4 Iso-frequency curves of 2D PhCs: with angular band gap (a), and without angular band gap (b). The blue fan-shaped areas where the dispersion curves corresponding to a specific frequency overlap show the reflected (a) and deflected (b) waves. The central circle and lateral circles represent the spatial dispersion in homogeneous medium and the lowest harmonic components in 2D PhC respectively.

The dispersion curves (illustrated by central dashed circles) for beam propagation in homogeneous medium, where $|k| = 2\pi/\lambda = constant$, are depicted. For low-contrast refractive index or low filling fraction medium, the dispersion circles of scattered light are well centered at reciprocal lattice points. While for high-contrast index or high filling fraction medium, the big dispersion circles split in the cross sections. The crossing areas describe the bending and distortion of the wave fronts. The light dispersion strongly modifies on those cross section areas. Here we mark the entire angular spectrum of incident beam as α, and the blue fan-shaped areas are eliminated from the spectrum due to spatial filtering.

In Fig 1.3.3-4 (a), we highlight the angular band gap in blue. In these regions, Bloch modes for certain angular components do not exist. Hence the propagation along these directions is prohibited and consequently the wave reflects back. In Fig 1.3.3-4 (b), we demonstrate particular dispersion curves with strongly tilted sections. Unlike the previous case, the angular components aiming at these tilted sections are deflected into first diffraction maxima. It is so called gapless filtering without appearance of angular band gaps [58].

1.4 Summary

In this chapter we gave a short introduction to PhCs including the theoretical description of light propagation there, experimental measurements and sample fabrication. In order to comprehensively understand numerical calculations, several analytical methods (PWE and FDTD) for wave propagation properties in PhC are also discussed and demonstrated. Last but not least, diverse phenomena (such as super-prism, self-collimation and spatial filtering) of light in PhC and the related mechanisms (negative refraction, negative diffraction and angular band gap) are interpreted and developed.

References

[1] E. Yablonovitch, “Inhibited spontaneous emission in solid-state physics and electronics,” *Physical review letters*, vol. 58, no. 20, p. 2059, 1987.

[2] S. John, “Strong localization of photons in certain disordered dielectric superlattices,” *Physical review letters*, vol. 58, no. 23, p. 2486, 1987.

[3] H. Kosaka, T. Kawashima, A. Tomita, M. Notomi, T. Tamamura, T. Sato, and S. Kawakami, “Photonic crystals for micro lightwave circuits using wavelength-dependent angular beam steering,” *Applied Physics Letters*, vol. 74, no. 10, pp. 1370–1372, 1999.

[4] N. Fabre, L. Lalouat, B. Cluzel, X. Mélique, D. Lippens, F. de Fornel, and O. Vanbésien, “Optical near-field microscopy of light focusing through a photonic crystal flat lens,” *Physical review letters*, vol. 101, no. 7, p. 073901, 2008.

[5] H. Kosaka, T. Kawashima, A. Tomita, M. Notomi, T. Tamamura, T. Sato, and S. Kawakami, “Self-collimating phenomena in photonic crystals,” *Applied Physics Letters*, vol. 74, no. 9, pp. 1212–1214, 1999.

[6] L. Maigyte, “Shaping of light beams with photonic crystals: spatial filtering, beam collimation and focusing, PhD” *Universitat Politècnica de Catalunya*, 2014.

[7] C.-R. Yang, Y.-S. Hsieh, G.-Y. Hwang, and Y.-D. Lee, “Photoablation characteristics of novel polyimides synthesized for high-aspect-ratio excimer laser LIGA process,” *Journal of Micromechanics and Microengineering*, vol. 14, no. 4, p. 480, 2004.

[8] C. Kraeh, A. Popsecu, M. Schieber, H. Hedler, T. Bieniek, G. Wielgoszewski, M. Moczała, and J. Finley, “Fabrication of high aspect ratio microtube arrays for 2D photonic crystals,” *Materials Research Express*, vol. 1, no. 2, p. 026201, 2014.

[9] J. D. Joannopoulos, S. G. Johnson, J. N. Winn, and R. D. Meade, *Photonic crystals: molding the flow of light*. Princeton university press, 2011.

[10] P.-G. Luan and C.-C. Chen, **光子晶體—從蝴蝶翅膀到奈米光子學**. **五南圖書出版股份有限公司**, 2005.

[11] K. M. Ho, C. T. Chan, and C. M. Soukoulis, “Existence of a photonic gap in periodic dielectric structures,” *Physical Review Letters*, vol. 65, no. 25, p. 3152, 1990.

[12] H. Kosaka, T. Kawashima, A. Tomita, M. Notomi, T. Tamamura, T. Sato, and S. Kawakami, “Superprism phenomena in photonic crystals: Toward microscale lightwave circuits,” *Journal of lightwave technology*, vol. 17, no. 11, p. 2032, 1999.

[13] F. Garcıa-Santamarıa, C. Lopez, F. Meseguer, F. Lopez-Tejeira, J. Sanchez-Dehesa, and H. T. Miyazaki, “Opal-like photonic crystal with diamond lattice,” *Applied Physics Letters*, vol. 79, no. 15, pp. 2309–2311, 2001.

[14] M. Qi, E. Lidorikis, P. T. Rakich, S. G. Johnson, J. D. Joannopoulos, E. P. Ippen, and H. I. Smith, “A three-dimensional optical photonic crystal with designed point defects,” *Nature*, vol. 429, no. 6991, pp. 538–542, Jun. 2004.

[15] K. M. Ho, C. T. Chan, C. M. Soukoulis, R. Biswas, and M. Sigalas, “Photonic band gaps in three dimensions: new layer-by-layer periodic structures,” *Solid State Communications*, vol. 89, no. 5, pp. 413–416, 1994.

[16] H. S. Sözüer and J. P. Dowling, “Photonic band calculations for woodpile structures,” *Journal of Modern Optics*, vol. 41, no. 2, pp. 231–239, 1994.

[17] E. Özbay, A. Abeyta, G. Tuttle, M. Tringides, R. Biswas, C. T. Chan, C. M. Soukoulis, and K. M. Ho, “Measurement of a three-dimensional photonic band gap in a crystal structure made of dielectric rods,” *Physical Review B*, vol. 50, no. 3, p. 1945, 1994.

[18] B. H. Cumpston, S. P. Ananthavel, S. Barlow, D. L. Dyer, J. E. Ehrlich, L. L. Erskine, A. A. Heikal, S. M. Kuebler, I.-Y. S. Lee, and D. McCord-Maughon, “Two-photon polymerization initiators for three-dimensional optical data storage and microfabrication,” *Nature*, vol. 398, no. 6722, pp. 51–54, 1999.

[19] “http://www.nanoscribe.de/en/products/photonic-professional-gt/,” *Nanoscribe*.

[20] M. Thiel, J. Ott, A. Radke, J. Kaschke, and M. Wegener, “Dip-in depletion optical

lithography of three-dimensional chiral polarizers," *Optics letters*, vol. 38, no. 20, pp. 4252–4255, 2013.

[21] S. Kim, F. Qiu, S. Kim, A. Ghanbari, C. Moon, L. Zhang, B. J. Nelson, and H. Choi, "Fabrication and Characterization of Magnetic Microrobots for Three-Dimensional Cell Culture and Targeted Transportation," *Advanced Materials*, vol. 25, no. 41, pp. 5863–5868, 2013.

[22] D. Jang, L. R. Meza, F. Greer, and J. R. Greer, "Fabrication and deformation of three-dimensional hollow ceramic nanostructures," *Nature materials*, vol. 12, no. 10, pp. 893–898, 2013.

[23] A. M. Greiner, B. Richter, and M. Bastmeyer, "Micro-engineered 3D scaffolds for cell culture studies," *Macromolecular bioscience*, vol. 12, no. 10, pp. 1301–1314, 2012.

[24] D. J. McCarron, "A guide to acousto-optic modulators," Technical report, Durham University, 2007.

[25] H.-B. Sun and S. Kawata, "Two-photon photopolymerization and 3D lithographic microfabrication," in *NMR• 3D Analysis• Photopolymerization*, Springer, 2006, pp. 169–273.

[26] H. Zeng, "Light Driven Microscopic Robot, PhD" *Università degli Studi di Firenze*, 2014.

[27] J. P. Vigneron, M. Rassart, C. Vandenbem, V. Lousse, O. Deparis, L. P. Biró, D. Dedouaire, A. Cornet, and P. Defrance, "Spectral filtering of visible light by the cuticle of metallic woodboring beetles and microfabrication of a matching bioinspired material," *Physical Review E*, vol. 73, no. 4, p. 041905, 2006.

[28] P. Vukusic, J. R. Sambles, and C. R. Lawrence, "Structural colour: Colour mixing in wing scales of a butterfly," *Nature*, vol. 404, no. 6777, pp. 457–457, 2000.

[29] P. Vukusic, "Structural colour in Lepidoptera," *Current Biology*, vol. 16, no. 16, pp. R621–R623, 2006.

[30] M. Crne, V. Sharma, J. Blair, J. O. Park, C. J. Summers, and M. Srinivasarao, "Biomimicry of optical microstructures of Papilio palinurus," *EPL (Europhysics Letters)*, vol. 93, no. 1, p. 14001, 2011.

[31] V. L. Welch, J. P. Vigneron, and A. R. Parker, "The cause of colouration in the ctenophore Beroe cucumis," *Current Biology*, vol. 15, no. 24, pp. R985–R986, 2005.

[32] R. C. McPhedran and A. R. Parker, "Biomimetics: Lessons on optics from nature's school," *Physics Today*, vol. 68, no. 6, pp. 32–37, 2015.

[33] A. R. Parker, V. L. Welch, D. Driver, and N. Martini, "Structural colour: opal analogue discovered in a weevil," *Nature*, vol. 426, no. 6968, pp. 786–787, 2003.

[34] K. Sakoda, *Optical properties of photonic crystals*, vol. 80. Springer Science & Business

Media, 2004.

[35] C. Kittel, *Introduction to solid state physics*. Wiley, 2005.

[36] A. Taflove and S. C. Hagness, *Computational electrodynamics*. Artech house, 2005.

[37] K.-D. Chang, "廣義光子晶體元件之研究與分析, PhD" *National Central University*, 2007.

[38] K. S. Yee, "Numerical solution of initial boundary value problems involving Maxwell's equations in isotropic media," *IEEE Trans. Antennas Propag*, vol. 14, no. 3, pp. 302–307, 1966.

[39] F. Zheng, Z. Chen, and J. Zhang, "A finite-difference time-domain method without the Courant stability conditions," *Microwave and Guided Wave Letters, IEEE*, vol. 9, no. 11, pp. 441–443, 1999.

[40] M. Notomi, "Theory of light propagation in strongly modulated photonic crystals: Refractionlike behavior in the vicinity of the photonic band gap," *Physical Review B*, vol. 62, no. 16, p. 10696, 2000.

[41] C. Luo, S. G. Johnson, and J. D. Joannopoulos, "All-angle negative refraction in a three-dimensionally periodic photonic crystal," *Applied physics letters*, vol. 81, no. 13, pp. 2352–2354, 2002.

[42] C. Luo, S. G. Johnson, J. D. Joannopoulos, and J. B. Pendry, "All-angle negative refraction without negative effective index," *Physical Review B*, vol. 65, no. 20, p. 201104, 2002.

[43] V. G. Veselago, "THE ELECTRODYNAMICS OF SUBSTANCES WITH SIMULTANEOUSLY NEGATIVE VALUES OF ϵ AND μ," *Physics-Uspekhi*, vol. 10, no. 4, pp. 509–514, 1968.

[44] J. B. Pendry and D. R. Smith, "Reversing light with negative refraction," *Physics today*, vol. 57, pp. 37–43, 2004.

[45] K. Staliunas and R. Herrero, "Nondiffractive propagation of light in photonic crystals," *Physical Review E*, vol. 73, no. 1, p. 016601, 2006.

[46] L. Maigyte, V. Purlys, J. Trull, M. Peckus, C. Cojocaru, D. Gailevičius, M. Malinauskas, and K. Staliunas, "Flat lensing in the visible frequency range by woodpile photonic crystals," *Optics letters*, vol. 38, no. 14, pp. 2376–2378, 2013.

[47] R. Iliew, C. Etrich, U. Peschel, F. Lederer, M. Augustin, H.-J. Fuchs, D. Schelle, E.-B. Kley, S. Nolte, and A. Tünnermann, "Diffractionless propagation of light in a low-index photonic-crystal film," *Applied physics letters*, vol. 85, p. 5854, 2004.

[48] X. Yu and S. Fan, "Bends and splitters for self-collimated beams in photonic crystals," *Applied Physics Letters*, vol. 83, no. 16, pp. 3251–3253, 2003.

[49] M.-W. Kim, S.-G. Lee, T.-T. Kim, J.-E. Kim, H. Y. Park, and C.-S. Kee, “Experimental demonstration of bending and splitting of self-collimated beams in two-dimensional photonic crystals,” *Applied physics letters*, vol. 90, no. 11, p. 113121, 2007.

[50] M. Augustin, R. Iliew, C. Etrich, D. Schelle, H.-J. Fuchs, U. Peschel, S. Nolte, E.-B. Kley, F. Lederer, and A. Tünnermann, “Self-guiding of infrared and visible light in photonic crystal slabs,” *Applied Physics B*, vol. 81, no. 2–3, pp. 313–319, 2005.

[51] J. W. Goodman, *Introduction to Fourier optics*. Roberts and Company Publishers, 2005.

[52] L. Maigyte and K. Staliunas, “Spatial filtering with photonic crystals,” *Applied Physics Reviews*, vol. 2, no. 1, p. 011102, 2015.

[53]I. Moreno, J. J. Araiza, and M. Avendano-Alejo, “Thin-film spatial filters,” *Optics letters*, vol. 30, no. 8, pp. 914–916, 2005.

[54] K. Xu, X. Zheng, C. Li, and W. She, “Design of omnidirectional and multiple channeled filters using one-dimensional photonic crystals containing a defect layer with a negative refractive index,” *Physical Review E*, vol. 71, no. 6, p. 066604, 2005.

[55] A. E. Serebryannikov, A. Y. Petrov, and E. Ozbay, “Toward photonic crystal based spatial filters with wide angle ranges of total transmission,” *Applied Physics Letters*, vol. 94, no. 18, p. 181101, 2009.

[56] E. Colak, A. O. Cakmak, A. E. Serebryannikov, and E. Ozbay, “Spatial filtering using dielectric photonic crystals at beam-type excitation,” *Journal of Applied Physics*, vol. 108, no. 11, p. 113106, 2010.

[57] K. Staliunas and V. J. Sánchez-Morcillo, “Spatial filtering of light by chirped photonic crystals,” *Physical Review A*, vol. 79, no. 5, p. 053807, 2009.

[58] L. Maigyte, T. Gertus, M. Peckus, J. Trull, C. Cojocaru, V. Sirutkaitis, and K. Staliunas, “Signatures of light-beam spatial filtering in a three-dimensional photonic crystal,” *Physical Review A*, vol. 82, no. 4, p. 043819, 2010.

Chapter 2 Light in liquid crystals

Following the general categorizations most of the matters are classified into solid, liquid and gas. There are some exceptions such as superfluid, plasma and liquid crystals (LCs). Liquid crystals, as named in such way, mean an intermediate stage where matters behave like flowing liquids yet exhibit some characteristics of crystals, e.g. birefringence in crystalline solids.

LCs possess abundant physical properties including electro-optical, thermo-optical, opto-optical and even opto-mechanical properties. Therefore we can easily find many LCs applications in display technology. Apart from applications in daily life, great interests from academic field are also developed and widely applied into photonic elements and devices, such as tunable filters [1], soliton waveguides [2] and micro-actuators [3].

This chapter begins with brief introduction upon general properties of LCs. The classification of LCs, birefringence, phase transitions and alignment methods are presented as fundamental prerequisites. Later on we focus on the reactions of LCs towards change of external fields (electric or optical), temperature (thermal), and polarization (optical). The mechanical properties as applied in elastomer are also demonstrated. Finally we conclude this chapter by giving a short summary.

2.1 Properties of liquid crystal in general

2.1.1 Chemical structures and phase transition

From chemical point of view, most liquid crystal molecules are composed of two aromatic rings A and A' with linkage group X in between (Fig 2.1.1-1). On the edges of LC molecules, they are connected with a side chain R and terminal group R', for example alkyl (C_nH_{2n+1}) or alkoxy ($C_nH_{2n+1}O$). The names of LCs are often referred to the linkage group, for instance Schiff-base LC (–CH=N–). Concerning LCs' chemical stability, the central linkage group dominates. For Schiff-base LCs, they are very unstable while for ester, azo (–N=N–) and

azoxy LCs are rather stable but sensitive to moisture, temperature change and ultraviolet (UV) radiation. One of the most commonly used commercial LCs is pentylcyanobiphenyl (5CB), whose structure is simple and very stable due to lacking in central linkage group [4]. It is also the main reason we chose 5CB for our investigation upon nematic LCs.

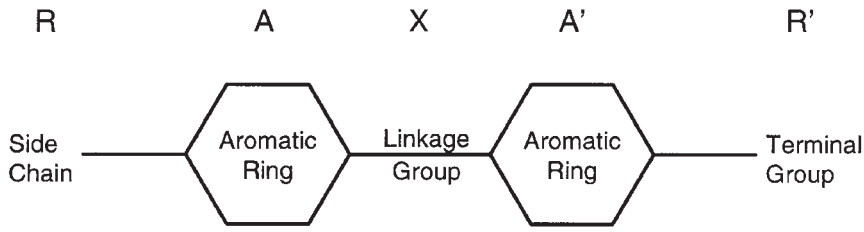

Fig 2.1.1-1 The basic structure of LCs [4]

Liquid crystal state is a mesogenic state between liquid and solid. Molecules in the liquid state are without intrinsic order while in the solid state they are extremely ordered. The LC state owns a certain level of order, which gives possibility to shape.

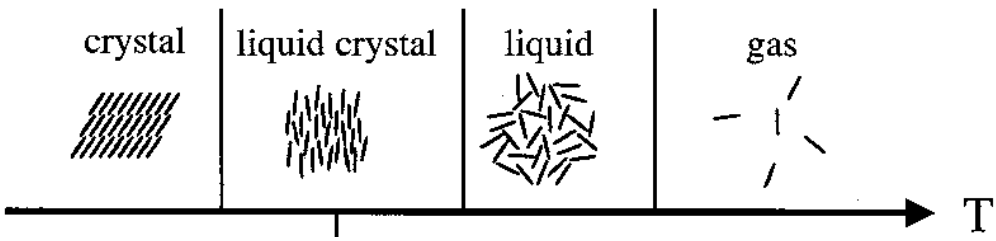

Fig 2.1.1-2 Temperature diagram for phase transition [5]

In order to describe the status of matter from random to order, an order parameter $S = (1/2)\langle 3cos^2\theta - 1\rangle$ is introduced to define the degree of order in different phases of LC. For instance, the order of nematic LCs usually varies between 0.5 – 0.9 and it decreases to 0 for the LCs when entering isotropic phase due to loss of orientation.

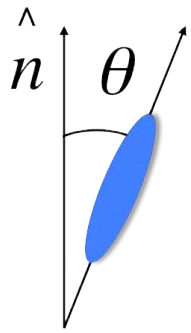

Fig 2.1.1-3 order parameter *S*

Concerning the mechanism of formation, liquid crystals are mainly classified into lyotropic, polymeric, thermotropic liquid crystals. Lyotropic phase is observed by increasing the concentration of amphiphilic molecules. Amphiphilic molecules first assemble into randomly distributed spherical bubbles to trap hydrophobic tails inwards while exposing the hydrophilic head toward water solvent. Then they will form long cylinders with hexagonal lattice arrangement and finally are separated by water layers in between. Soap is a common example of lyotropic LCs.

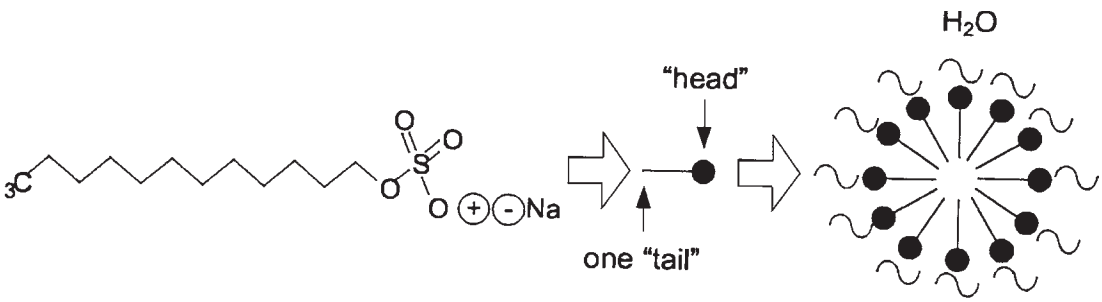

Fig 2.1.1-4 Schematic of soap forming micelles [4]

Polymeric LCs are formed by monomer units. Depending on the monomer structure, the degree of flexibility of polymeric LCs is various. For instance, vinyl type is more flexible compared to Kevlar polymer. Therefore polymeric LCs are usually classified regarding mesogenic monomer structure. Main-chain polymers are formed by monomers either directly linked along the molecule chain direction or with some short spacers. Side-chain polymers are built by pendant monomers attached to a polymeric chain. Polymeric LCs in general possess higher viscosity than monomers.

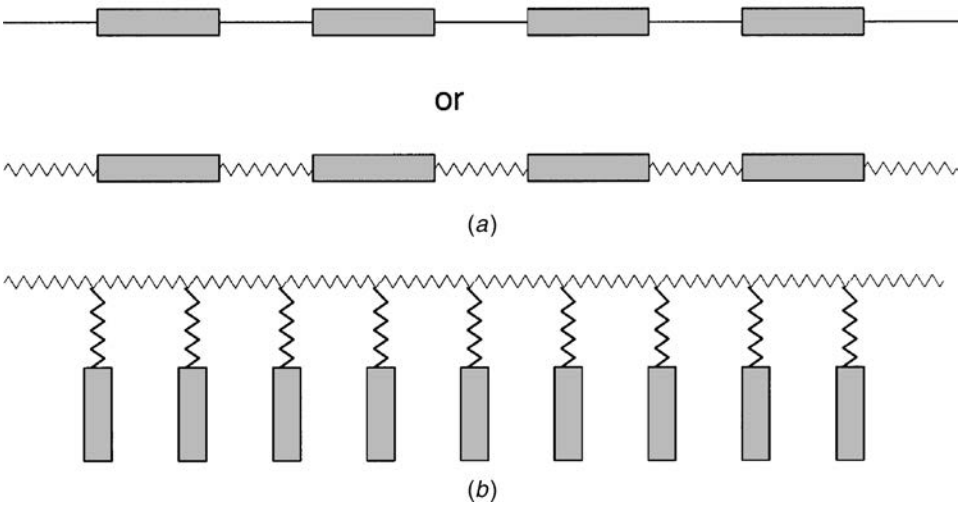

Fig 2.1.1-5 Main-chain (a) and side-chain (b) polymeric LCs [4]

Enhancing thermal motion destroys the order of molecules. Between crystalline solid and isotropic liquid, thermotropic LCs are often divided into large amount of mesophases referring to the orientation of LC molecules: those which exhibit only orientational order (N) and those which show additionally positional order (smectic, columnar etc.) Moreover, it is important to distinguish non-chiral mesophases (N, SmA, SmC, etc.) from chiral phases (N*, SmA*, SmC*, etc.). In nematic phase, the molecules are like liquids located in random position yet aligned along the director axis. Cholesteric LCs (chiral nematic LCs) are nematic LCs aligning in a helical way. By adding a chiral molecule to nematic LCs, they are formed after chemical synthesis. Smectic LCs are positionally ordered along one direction unlike nematic LCs are positionally random. For example, the molecules are oriented along the layer normal in the smectic-A phase while they are tilted away in the smectic-C phase.

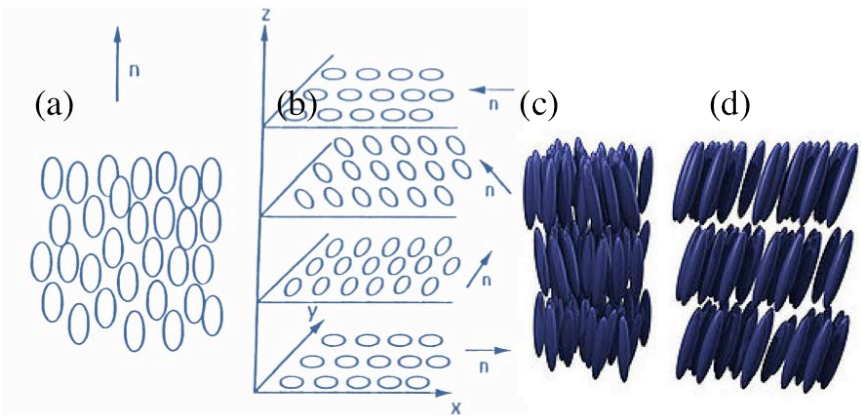

Fig 2.1.1-6 Alignment of LC molecules in nematic (a), cholesteric (b) [4], smectic-A (c), and smectic-C (d) [6] phases

2.1.2 Birefringence

Crystals are often defined as either isotropic or anisotropic materials concerning whether the optical behavior are equivalent along crystallographic axes. When light propagates into an isotropic crystal, the light passes with one velocity and is refracted at a constant angle in spite of the incident angle with respect to the crystallographic axes. When light enters an anisotropic crystal (e.g. quartz and calcite) with the incident angle parallel to the optical axis of crystal, light behaves in the same way as passing through isotropic crystals. However if light enters in other angles, the light is separated into two orthogonal polarizations travel with distinct velocities (Fig 2.1.2-1). This is called birefringence (double refraction).

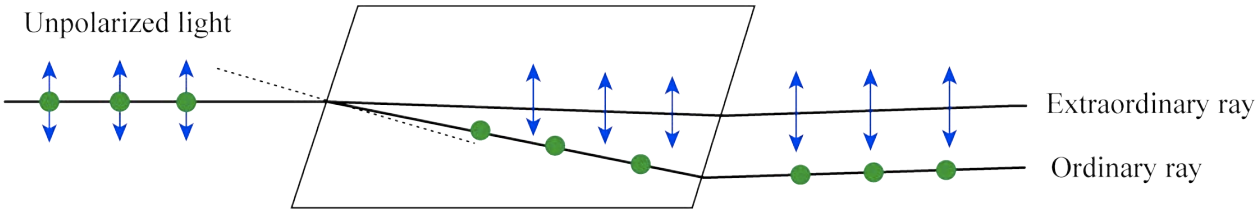

Fig 2.1.2-1 Polarization dependent refractive indices in birefringent materials [6]

The refractive index ellipsoid is introduced to describe such different light velocities (Fig 2.1.2-2). For uniaxial crystals, the refractive index for the light polarization parallel to the optic axis is regarded as extraordinary index n_e while for the vertical case is regarded as ordinary index n_o. When an unpolarized beam enters a LC and propagates perpendicular to the director, it will be split in an ordinary and an extraordinary beam. Both beams share the same propagation direction, but exhibit different phase velocities. To quantify birefringence, the difference between two featured indices $\Delta n = n_e - n_o$ is introduced. For $n_e > n_o$, it is defined as positive birefringence. For $n_e < n_o$, it is defined as negative birefringence.

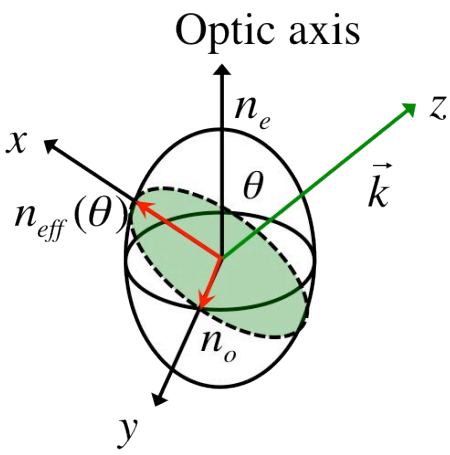

Fig 2.1.2-2 Refractive index ellipsoid of uniaxial crystals

2.1.3 Surface anchoring and liquid crystals alignment

Several types of molecular orientation are presented: degenerate planar, uniform planar, homeotropic and uniform tilted alignment. They can be achieved by different surface treatment. Uniform planar and homeotropic alignments are mostly used in LC applications. Uniform planar alignment means the long axes of molecules not only lie down on the substrate plane but also point along the rubbing direction. On the contrary, homeotropic alignment means the long axes of molecules stand and point towards the surface normal.

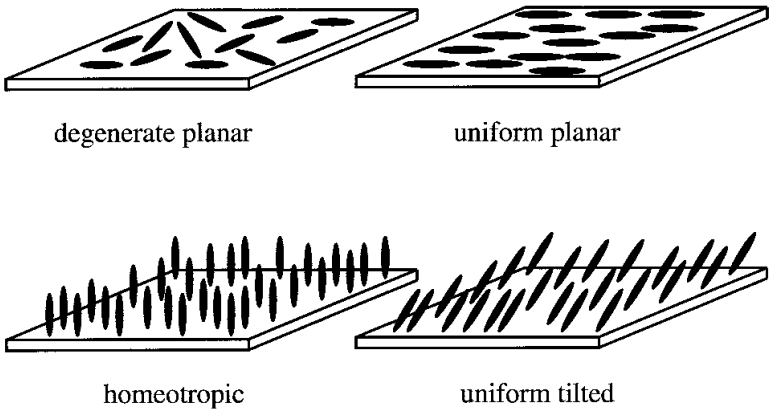

Fig 2.1.3-1 Different molecular orientations on the substrates [5]

To obtain uniform planar alignment, one of the most common methods is to rub a thin polymer film deposited on glass substrate with a piece of lens tissue. The coated polymer can be polyvinyl alcohol (PVA) or polyimide (PI 130, Nissan Chemical Industries). As for homeotropic alignment, a different polyimide (PI 1211, Nissan Chemical Industries) is used.

Bear in mind the micro-fabrication technique mentioned in Chapter 1, the polymer grating grooves written on substrates are also utilized to make uniform planar alignment.

With two slides of polymer-coated glass, we are able to create diverse alignment configurations for nematic LCs. In Fig 2.1.3-2, uniaxial, twisted and splayed configurations are demonstrated. A LC cell with uniaxial configuration is achieved by two pieces of uniform planar align glass rubbed in the parallel direction. A twisted configuration is two pieces of uniform planar align glass rubbed in two orthogonal directions. A splayed configuration is obtained by one piece of uniform planar align glass and one piece of homeotropic align glass. The LC molecules near the command substrates orient their long axes along either the rubbing direction (uniaxial and twist) or perpendicularly (splay) while the rest molecules experience gradual evolution towards the surface orientations.

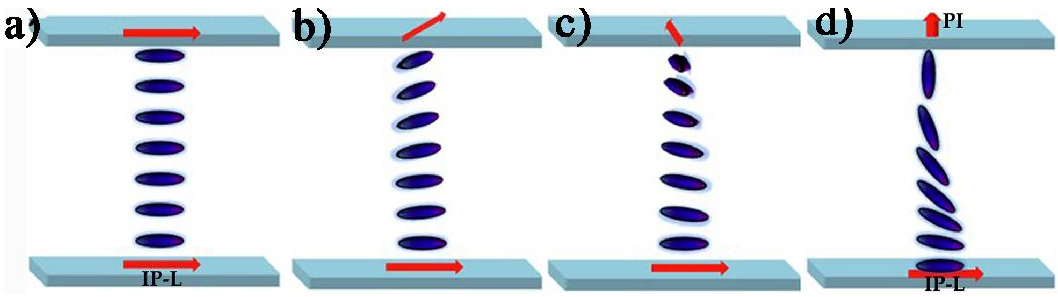

Fig 2.1.3-2 (a) Uniaxial, (b-c) twisted and (d) splayed configurations of nematic LC cell [7]

2.1.4 Liquid crystals interaction with external field

Differ from ordinary solids, LCs possess appealing elastic properties which give restoring force under any external perturbation field attempting to deform the alignments of LCs. Elastic constants are introduced to express the relation between deformation and restoring stresses. There are basically three elastic constants corresponding to various director axis deformations: splay (K_1), twist (K_2) and bend (K_3) deformations. Twist deformation illustrates a rotation of LC molecules following the direction of the torque while splay and bend deformations involves changes of the director axis of LCs as depicted in Fig 2.1.4. Concerning the rigid-rod shape of molecules, K_3 is usually the largest constant among the three factors in the typical order ~10 pN for nematic LCs.

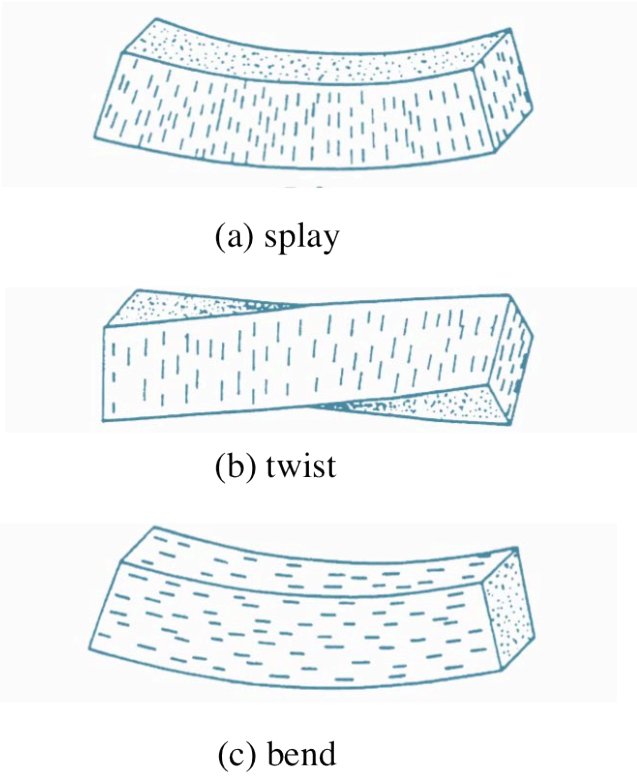

Fig 2.1.4-1 Splay (a), twist (b) and bend (c) deformations of LCs [4]

The free-energy densities (energy per volume) related to splay f_1, twist f_2 and bend f_3 deformations are developed by Frank in 1958:

$$f_1 = \frac{1}{2}K_1(\nabla \cdot \hat{n})^2 \tag{2.1}$$

$$f_2 = \frac{1}{2}K_2(\hat{n} \cdot \nabla \times \hat{n})^2 \tag{2.2}$$

$$f_3 = \frac{1}{2}K_3(\hat{n} \times \nabla \times \hat{n})^2 \tag{2.3}$$

The total distortion free-energy density including all the types of deformation is written into:

$$F_d = \frac{1}{2}K_1(\nabla \cdot \hat{n})^2 + \frac{1}{2}K_2(\hat{n} \cdot \nabla \times \hat{n})^2 + \frac{1}{2}K_3(\hat{n} \times \nabla \times \hat{n})^2 \tag{2.4}$$

It can be further simplified by making the one-constant approximation ($K_1 = K_2 = K_3 = K$) [4]:

$$F_d = \frac{1}{2}K[(\nabla \cdot \hat{n})^2 + (\nabla \times \hat{n})^2] \tag{2.5}$$

The free-energy is by the volume integral of the total distortion free-energy density over the LC domain. The alignment of LC can be determined by minimizing this parameter. When the external electric field is switched on, the perturbation term is added to the total free-energy density and taking the same integral again. The new alignment can be found after making its minimization.

When an electric field is applied to LC, in order to reach minimization of the total free-energy, a torque is formed upon the director of LC. The torque gives different rotations to the LC director referring to the dielectric anisotropy $\Delta\varepsilon = \varepsilon_{\parallel} - \varepsilon_{\perp}$ as illustrated in Fig 2.1.4-2. The displacement **D** is given by:

$$\mathbf{D} = \varepsilon_{\mathbf{0}}\varepsilon_{\perp}\mathbf{E} + \varepsilon_{\mathbf{0}}(\varepsilon_{\parallel} - \varepsilon_{\perp})(\hat{n} \cdot \mathbf{E})\hat{n} \tag{2.6}$$

The external perturbation term contributed to the total free-energy density of LC is expressed through the following form:

$$\mu_E = -\int_0^E \mathbf{D} \cdot d\mathbf{E} = -\frac{1}{2}\varepsilon_{\mathbf{0}}\varepsilon_{\perp}(\mathbf{E} \cdot \mathbf{E}) - \frac{\varepsilon_{\mathbf{0}}\Delta\varepsilon}{2}(\hat{n} \cdot \mathbf{E})^{\mathbf{2}} \tag{2.7}$$

By substituting the angle α between the electric field **E** and the director $\hat{n}$, it can be rewritten into:

$$\mu_E = -\frac{1}{2}\varepsilon_{\mathbf{0}}\varepsilon_{\perp}E^2 - \frac{\varepsilon_{\mathbf{0}}\Delta\varepsilon}{2}E^{\mathbf{2}}\cos^2\alpha \tag{2.8}$$

The minimum of energy is therefore obtained from taking minimization of μ_E. For the case $\Delta\varepsilon > 0$, the minimum of energy lies in $\alpha = 0$ while for $\Delta\varepsilon < 0$, the minimum of energy lies in $\alpha = \pi/2$.

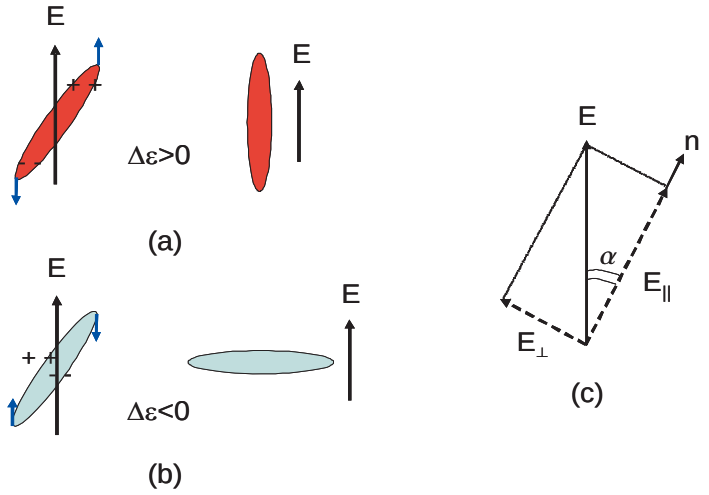

Fig 2.1.4-2 The parallel (a) or perpendicular (b) alignment to the applied electric field(c) depending on the sign of dielectric permittivity difference [8]

When the external torque from applied field is small, an elastic torque appears and keeps the molecules in their original positions. When the electric field reaches a threshold the director rotate and reorient toward being parallel (Fig. 3.11(a)) or perpendicular (Fig. 3.11(b)) to the direction of the electric field. This is called Fredericks transition.

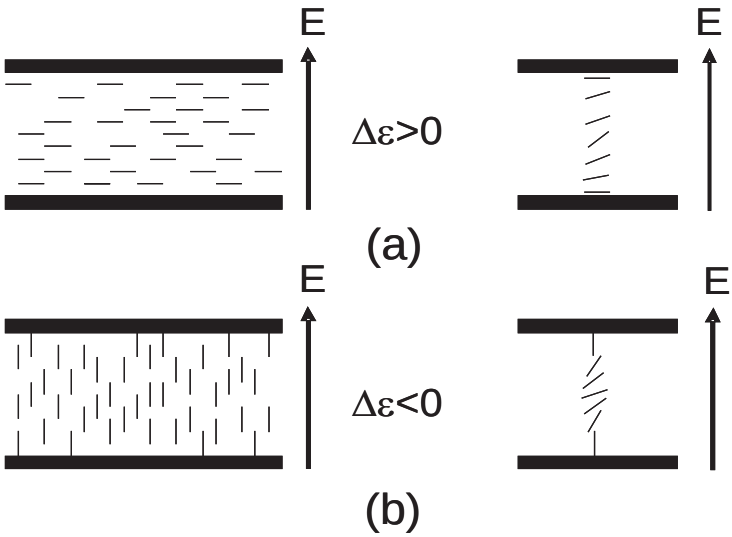

Fig 2.1.4-3 Reorientations of the director occurs when the external electric field appears in planar (a) or in homeotropic (b) cases [8].

By balancing the torques from both the elastic free-energy density and the contribution of the electric field, the Fredericks transition is written into following expression [4]:

$$E_{th} = \left(\frac{\pi}{d}\right)\left(\frac{K}{\varepsilon_0 \Delta\varepsilon}\right)^{1/2} \tag{2.9}$$

Or

$$V_{th} = \pi\left(\frac{K}{\varepsilon_0 \Delta\varepsilon}\right)^{1/2} \tag{2.10}$$

where d is the distance between the electrodes and K is the elastic constant corresponding to the various deformations. An example of LC response under applied electric field is demonstrated below in Fig 2.1.4-4.

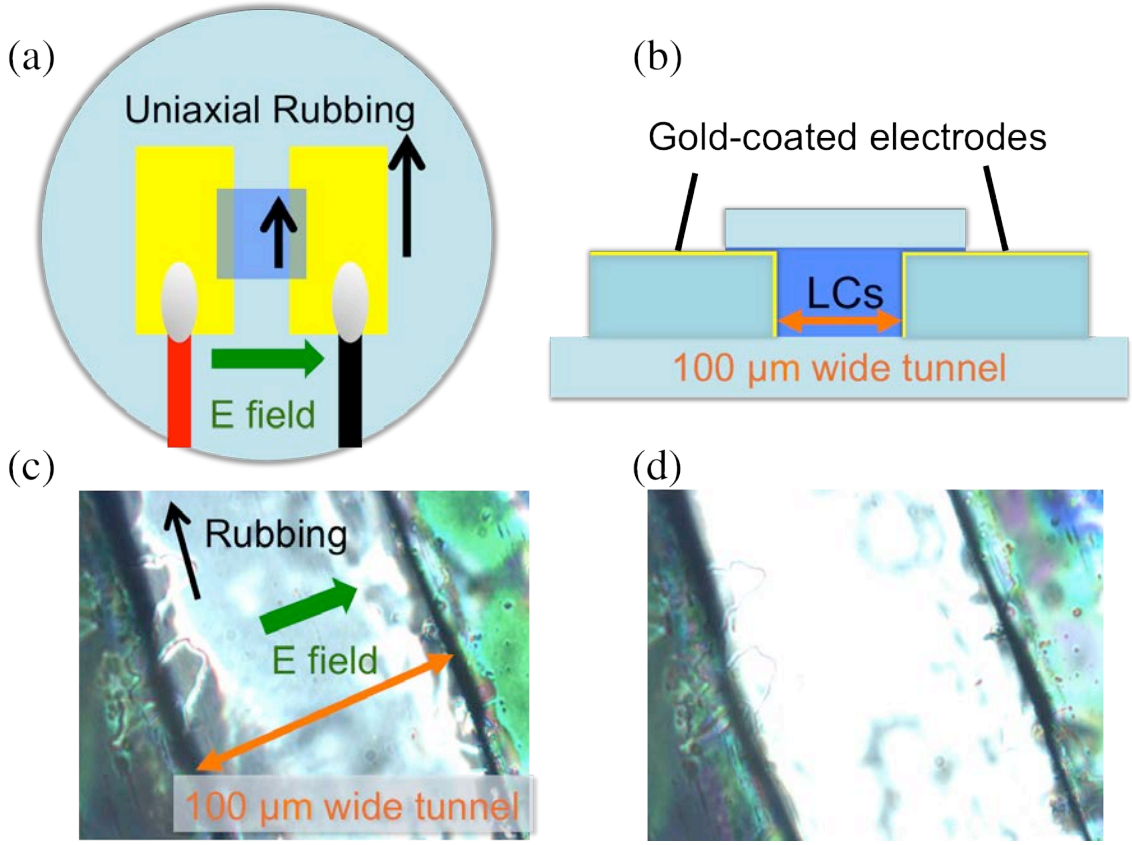

Fig 2.1.4-4 The uniaxial LC 5CB cell with planar gold-coated electrodes (a) top and (b) side view. When rotating the cell into 45° tilt, the birefringence observed (c) before and (d) after applying external electric field $0.5\ \mathrm{V}/\mu\mathrm{m}$ above Fredericks threshold under POM.

2.2 Temperature dependence

2.2.1 General equations as function of temperature

The temperature dependence of LC devices is very crucial. Concerning the change of order resulting from the thermal motion, a consequent change upon extraordinary and ordinary refractive indices n_e and n_o is expected. Usually the temperature gradient dn_e/dT of n_e is negative while for n_o it could be either positive or negative. For instance, the commercial LC 5CB own positive gradient while E7 possess negative gradient at room temperature.
The average refractive index is [9]:

$$\langle n \rangle = \frac{n_e + 2n_o}{3} \tag{2.11}$$

With the birefringence Δn introduced in 2.1.2, the extraordinary and ordinary refractive indices are expressed in the following form:

$$n_e = \langle n \rangle + \frac{2}{3}\Delta n \tag{2.12}$$

$$n_o = \langle n \rangle - \frac{1}{3}\Delta n \tag{2.13}$$

According to Haller's approximation upon the order parameter $S = (1 - T/T_c)^{\beta}$ [10], the birefringence can be interpreted as function of operating temperature:

$$\Delta n(T) \approx (\Delta n)_0 \left(1 - \frac{T}{T_c}\right)^{\beta} \tag{2.14}$$

where $(\Delta n)_0$ stands for the birefringence of the LC at T = 0 K, the clearing temperature T_c and material constant β differ various LCs. As reported by other research group, when increasing operating temperature the average refractive index $\langle n \rangle$ drops linearly [11]:

$$\langle n \rangle = A - BT \tag{2.15}$$

After substituting the linear relation of $\langle n \rangle$ (2.15) and the approximation of Δn (2.14) back to (2.12) and (2.13), the temperature-dependent LC indices are obtained:

$$n_e(T) \approx A - BT + \frac{2}{3}(\Delta n)_0 \left(1 - \frac{T}{T_c}\right)^{\beta} \tag{2.16}$$

$$n_o(T) \approx A - BT - \frac{1}{3}(\Delta n)_0 \left(1 - \frac{T}{T_c}\right)^{\beta} \tag{2.17}$$

which is also called the four-parameter model for the temperature effect upon the LC refractive indices [12]. A typical diagram of such temperature dependence is demonstrated below in Fig 2.2.1.

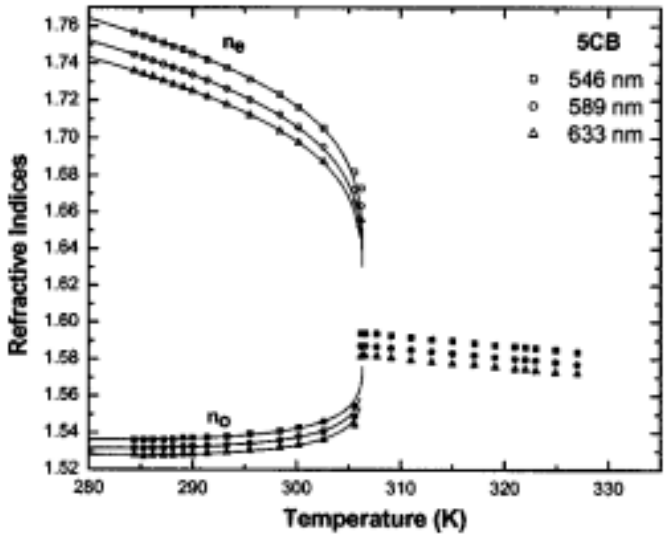

Fig 2.2.1 The refractive indices n_e and n_o of 5CB are measured as function of operating temperature [12]

2.2.2 Applications of thermal effect

The importance of the temperature effect deserves high attention especially for display technology. Referring to the thermal heating from the lamp (which often makes the operating temperature rise up to 50°C - 60°C), the properties of LCs at such condition are required in advance. Several related investigation upon increasing the temperature range of the LC nematic state has been reported. Using eutectic mixture method, a new LC mixture containing isothiocyanato tolanes is produced and stays in nematic state from 10.3°C to 141°C [13].

Moreover, the temperature dependence of LCs is widely exploited in tunable LC photonic integrated devices. In Fig 2.2.2-1, the performance of a photonic crystal fiber (PCF) filled with cholesteric LC is demonstrated. By varying the temperature below the phase transition point T_c=94°C, the guided modes change from green, yellow, off-state to blue. The scattering strongly contributes to the off-state when the temperature is close to the transition [14].

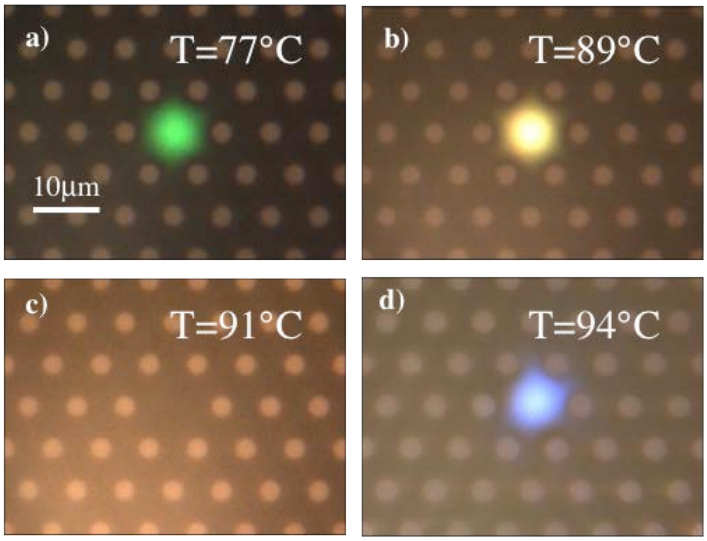

Fig 2.2.2-1 The spectrum shift of guided modes in PCF from (a) green, (b) yellow, (c) off-state to (d) blue [14].

Another promising application of LCs lies in nonlinear optics. By doping a small amount of dye (~ 1% wt.) into LCs, the dye can absorb the incident beam and heat up LCs. Although the presence of dye could bring either thermal enhancement or the optical Freedericksz effect (OFE), i.e. the reorientation angles appear as function of beam intensity when the optical field exceeds Freedericksz's threshold external electric field is adopted in order to freeze the director the torque of optical field cannot dominate. When LC is heated up, the negative temperature dn_e/dT of e-ray and positive dn_o/dT of o-ray bring interesting phenomena like defocusing and focusing respectively as found in Fig 2.2.2-2. Consequently a pure thermal nonlinear effect is observed [15].

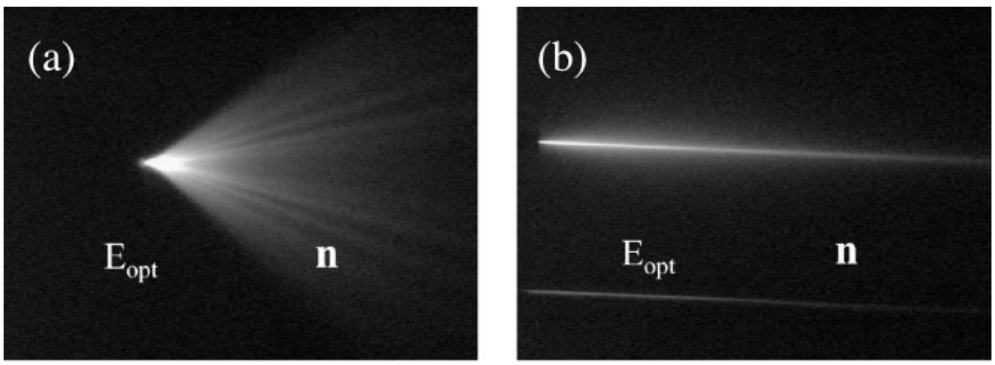

Fig 2.2.2-2 The e-ray defocusing (a) and the o-ray focusing (b) attributed to thermal nonlinear effect [15]

2.3 Polarization and wavelength dependence

2.3.1 General equations as function of wavelength

To describe normal dispersion in visible region, Cauchy's equation is commonly used for transparent materials such as isotropic liquids, fused silica and various types of glass [16]. However, to describe dispersion properties of anisotropic liquids, it is required to be extended. For LCs in the isotropic state, a traditional Cauchy's equation is used to illustrate the wavelength dependence:

$$n_i(\lambda) = A_i + \frac{B_i}{\lambda^2} + \frac{C_i}{\lambda^4} \tag{2.18}$$

where A_i, B_i, and C_i are Cauchy's coefficients for LCs in isotropic state.

For LCs in the nematic state, the extended Cauchy's equation can be expressed in similar form:

$$n_e = A_e + \frac{B_e}{\lambda^2} + \frac{C_e}{\lambda^4} \tag{2.19}$$

$$n_o = A_o + \frac{B_o}{\lambda^2} + \frac{C_o}{\lambda^4} \tag{2.20}$$

where $A_{e,o}$, $B_{e,o}$, and $C_{e,o}$ are Cauchy's coefficients for e-ray and o-ray in LC nematic state. These two equations also show the comprehensive temperature and wavelength dependence of LC refractive indices in the off-resonance region. For commercial LCs 5CB, these three fitting parameters are obtained from six data points from literature information and later compared with fifty data points measured in visible region at given temperature in order to validate this model [17]. The fitting curves for refractive indices as function of wavelength are depicted in Fig 2.3.1.

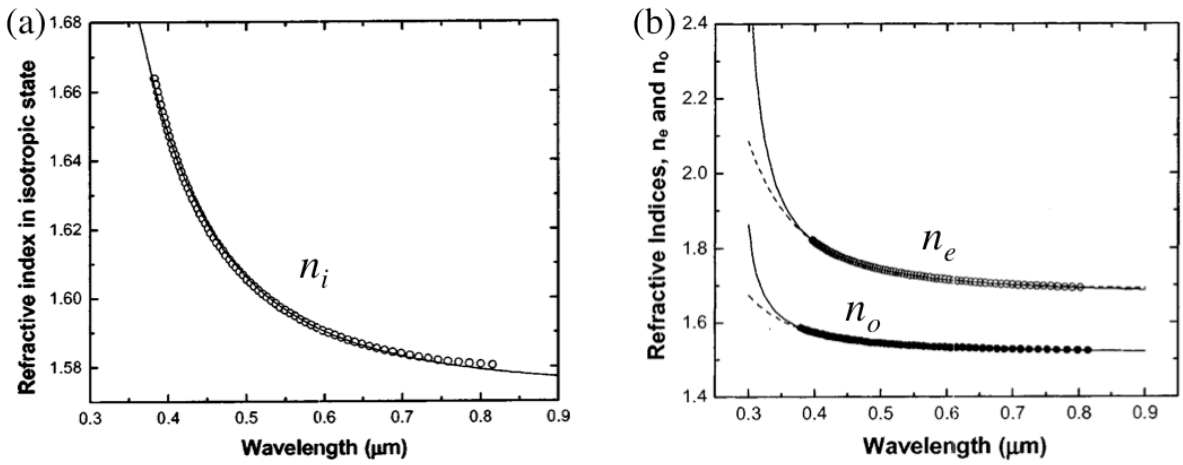

Fig 2.3.1 The refractive indices n_i(a), n_e and n_o(b) of 5CB are measured as function of input wavelength [17]

2.3.2 Polarized optical microscopy

Polarized optical microscopy (POM) is a useful microscope technique to investigate alignment of LCs. The experiment setup, as depicted in Fig 2.3.1, is generally composed of an unpolarized white lamp, the sample holder between two crossed linear polarizers (so called polarizer and analyzer), and the optional rotation stage.

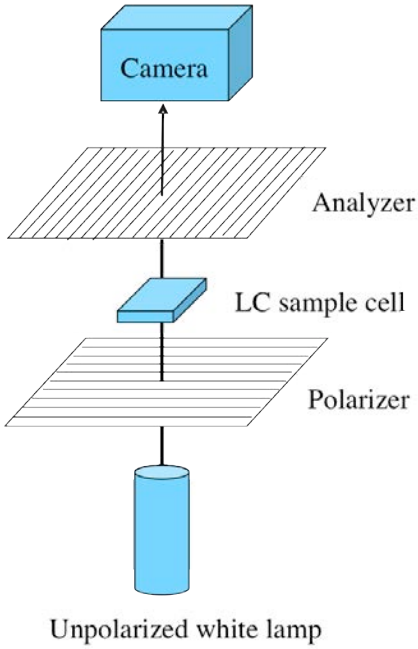

Fig 2.3.2-1 Schematic of polarized optical microscope for LCs investigation

When either LC sample is in isotropic state or the holder is empty, the analyzer blocks totally the orthogonal polarization of light selected by the polarizer. Hence a complete darkness is observed from eyepiece or CCD. On the other hand, if LC sample is in nematic state with dominant birefringence, the selected linear polarization from incident beam may rotate when propagating through the sample and pass the analyzer. Therefore colorful patterns from LCs are observed. The colors are caused by the various optical path differences OPD = $\Delta n \cdot d$, contributed by the optical birefringence Δn and the sample thickness d. It is also linked with the angle between the polarizers and the optical axis of the sample. Whether the order of LC alignment is good or not can be determined by observing the colors under POM.

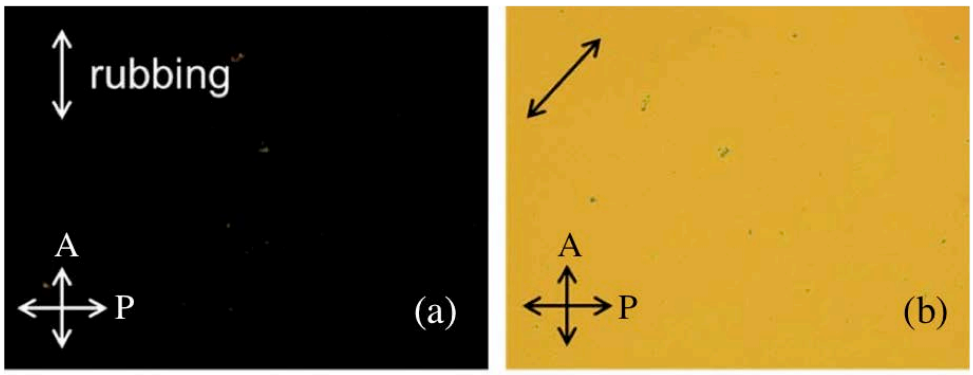

Fig 2.3.2-2 POM images of well uniaxial alignment from polymeric LCs in nematic state [18].

2.3.3 Polymer-Dispersed Liquid Crystals (PDLC) and related applications

Polymer-Dispersed Liquid Crystals (PDLCs) are commonly used for display purpose e.g. smart window. PDLC is a flexible material that can be polymerized to any desired size. The form of PDLC is usually a piece of plastic film without sealing requirement. Generally PDLC is composed of homogeneous prepolymer and LCs mixture. As the polymer gets cured, phase separation between LC liquid droplets and solid polymer reaches.

There are three common methods for preparing PDLC: polymerization-induced, thermally-induced, and solvent-induced phase separation [19]. Polymerization-induced phase separation begins when the initiators are activated by irradiation or other stimulation. When the polymerization proceeds, since the LC molecules are not linked to the polymer chain, they are separated and form droplets. Thermally-induce phase separation is suitable for the polymers possessing the melting point below the decomposition temperature. The mixture is formed by increasing the temperature above the melting point of polymer. With following cooling procedure at certain rate, the polymer becomes solid and LC droplets are generated. Solvent-induced phase separation describes that both LCs and the polymer are dissolved in specific solvent to form mixture. After the evaporation of solvent, the droplets of LC grow when the polymer is separated and becomes solid. To control the size of LC droplets, the crosslinking density of polymer, the polymerization rate, the cooling rate and the evaporation rate are very important factors. With the higher reaction rates and crosslinking density, the smaller domains of LC droplets are formed.

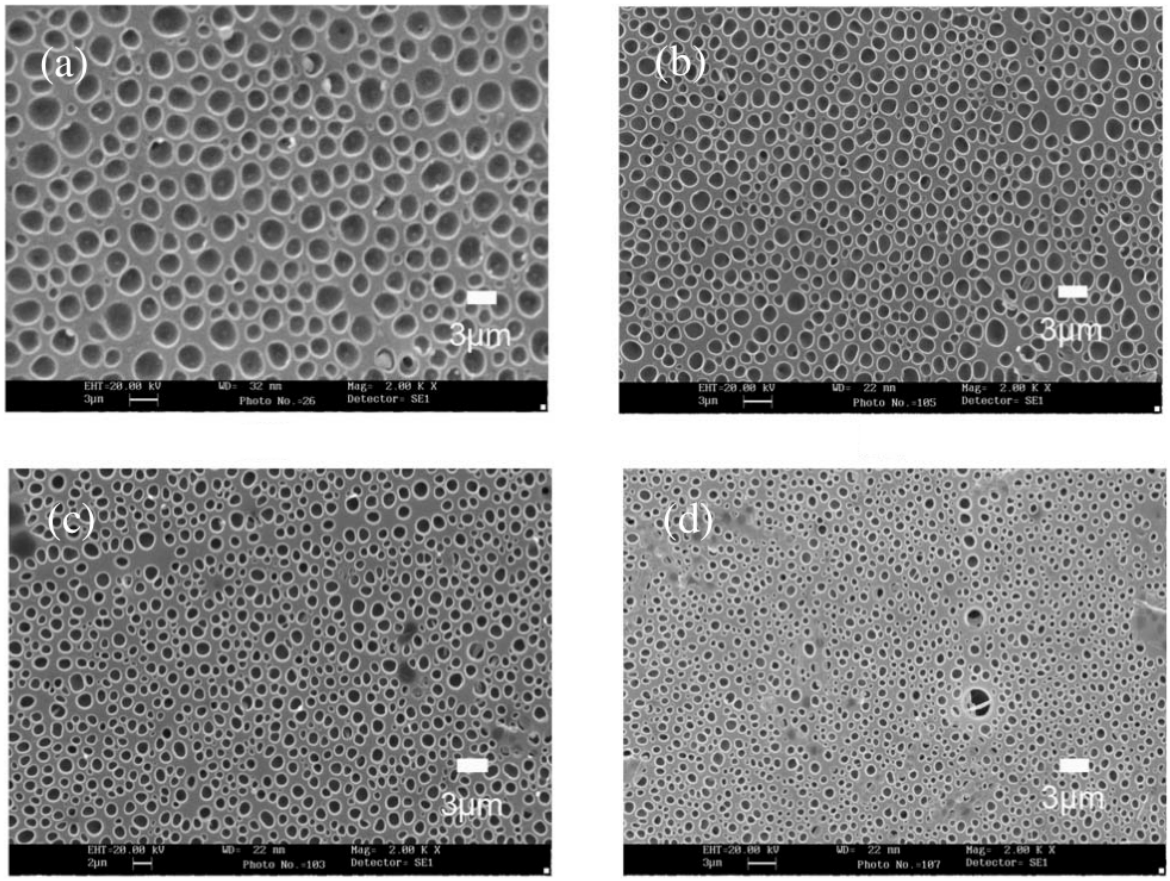

Fig 2.3.3-1 SEM images of the decreasing domains of LC droplets from (a) to (d) concerning the increased crosslinking density and polymerization rates [20]

The idea of PDLC is proposed to control the light scattering of LC droplets by external electric field for thin film display. The PDLC film is often sandwiched between two indium tin oxide (ITO) transparent electrodes. When the applied voltage is at off state, the optical axes of the micro LC droplets are randomly oriented and light scattering is huge. As a consequence, the PDLC film appears opaque. While when the voltage is on, the optical axes of LC droplets are well aligned along the electric field. The film therefore appears transparent. In short, by switching on and off the external field the incident light can be scattered or transmitted based on the alignment of LC droplets.

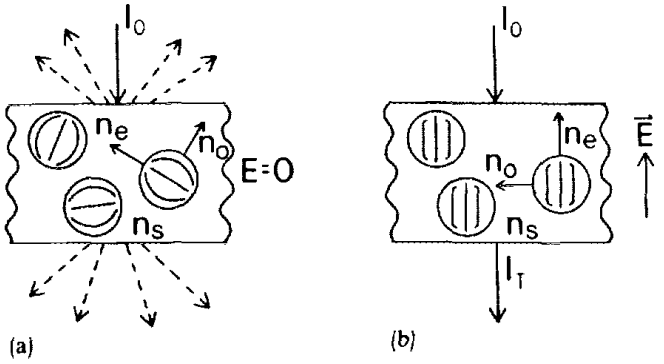

Fig 2.3.3-2 Schematic of random (a) and ordered (b) alignment under off and on state of external **E** field [21]

In addition to applying external electric field upon PDLC film, other advanced research has been carried out in photonic devices. For instance, the microvoid channels of 3D woodpile PhC are constructed by focusing femtosecond pulsed laser beam inside PDLC matrix. By impinging either electric or optical field into the composite sample, the alignment of LC droplets changes the effective refractive index and contributes to the stop band shift. Moreover, when increasing the doping ratio of LCs, the tuning of stop band location becomes even distinct [22] [23].

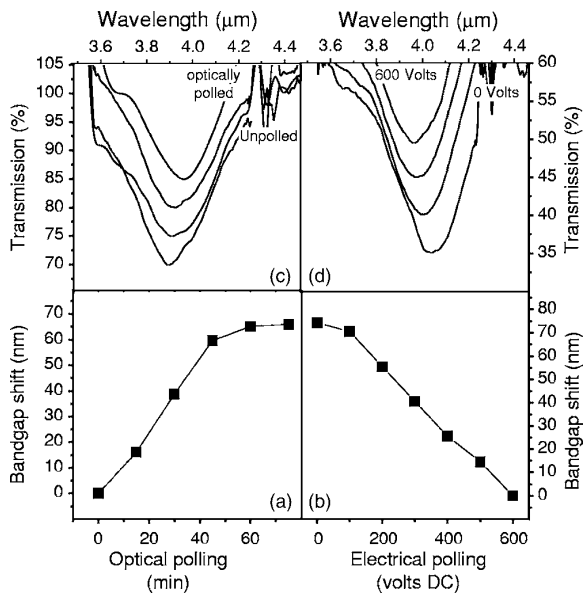

Fig 2.3.3-3 The stop band shift of PhC - PDLC composite attributed to external optical or electrical tuning [23].

2.4 Elastic and mechanical property – liquid crystalline elastomers

2.4.1 Configurations of Liquid Crystalline Elastomer (LCE)

As mentioned earlier in 2.1.1, polymeric LCs are categorized into main-chain or side-chain polymeric LCs. Generally no matter for main-chain polymeric LCs or side-chain polymeric LCs, they are composed of three structural elements: the backbone, the mesogen and the spacer. The rigidity of backbones is related to the glass transition temperature. In order to observe LC state at lower temperature, the backbone are required to be made more flexible, e.g. polysiloxane main chain [24]. The alignment of the mesogen is crucial to LC behavior. The existence of spacer between the backbone and the mesogen gives mesogen freedom to orient independently. Usually the increase of spacer length leads to decrease of glass transition temperature.

There are several shape configurations for the side-chain polymeric LC: side-on, end-on (oblate) and end-on (prolate) linking. The side-on and end-on (prolate) linking encourage elongation along the principal axis $\hat{n}$ similar to the case for the main-chain polymeric LC while the end-on (oblate) linking promotes the backbone flattening in the plane perpendicular to the director. Furthermore when cross-linking several chains of polymeric LCs into a network, liquid crystalline elastomers (LCE) are formed [25]. The elastic properties originate from the anisotropic chain conformation of the network. For instance, the external mechanical stress could bring uniform chain anisotropy i.e. reorientation behavior in the nematic state [26]. Moreover, without external field a network anisotropy could also be introduced by synthesis in advance [27].

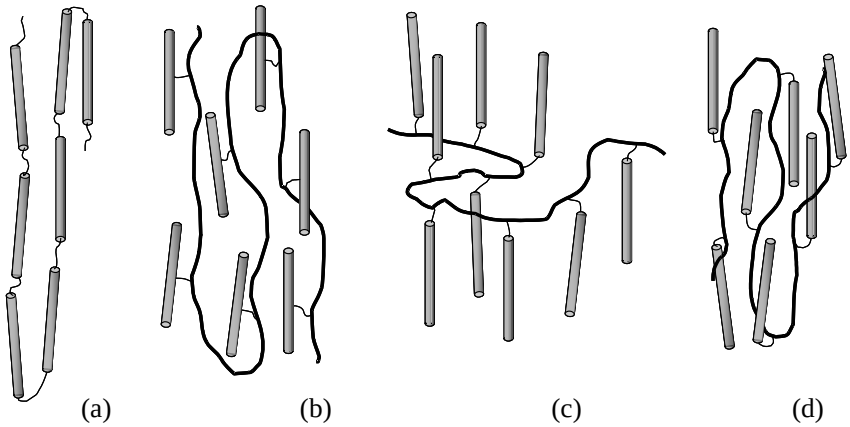

Fig 2.4.1 Different shape configurations of LC backbones. (a) the main-chain polymeric LC, (b) side-on, (c) end-on (oblate) and (d) end-on (prolate) of the side-chain polymeric LC [25]

2.4.2 Advanced functions of LCE and related stimulation

Several pre-alignment configurations of LCs introduced in 2.1.3 are adopted by either mechanical rubbing technique or chemical surface treatment on substrate for various purposes. To function as bending films, the uniaxial alignment could induce large motion in the presence of the pH or humidity difference upon upper and lower surfaces while the twisted and the splayed alignments do not require environmental gradients but 90° offset of preferred expansion directions from the opposite surfaces [28].

Apart from environmental gradients, light induced isomerization and heat are also common approaches to achieve film deformation. By adding photochromic molecules, such as azobenzene, to LC systems, the photo induced structural changes could induce LCE deformation. Controlled by alternative irradiation of UV (360nm) and visible light (450nm), at micro scale the molecular length first decreases when reaching *cis* state and later increases when retrieving *trans* state, while at macro scale it corresponds to the bending and flattening deformation of the LCE film [29]. Furthermore by varying the linear polarization directions of stimulated UV, the bending directions among the same LC film change correspondingly [30]. Several advanced functions in micro robotics like rolling [31] and cantilever [32] are realized and demonstrated in Fig 2.4.2-1 due to the same mechanism.

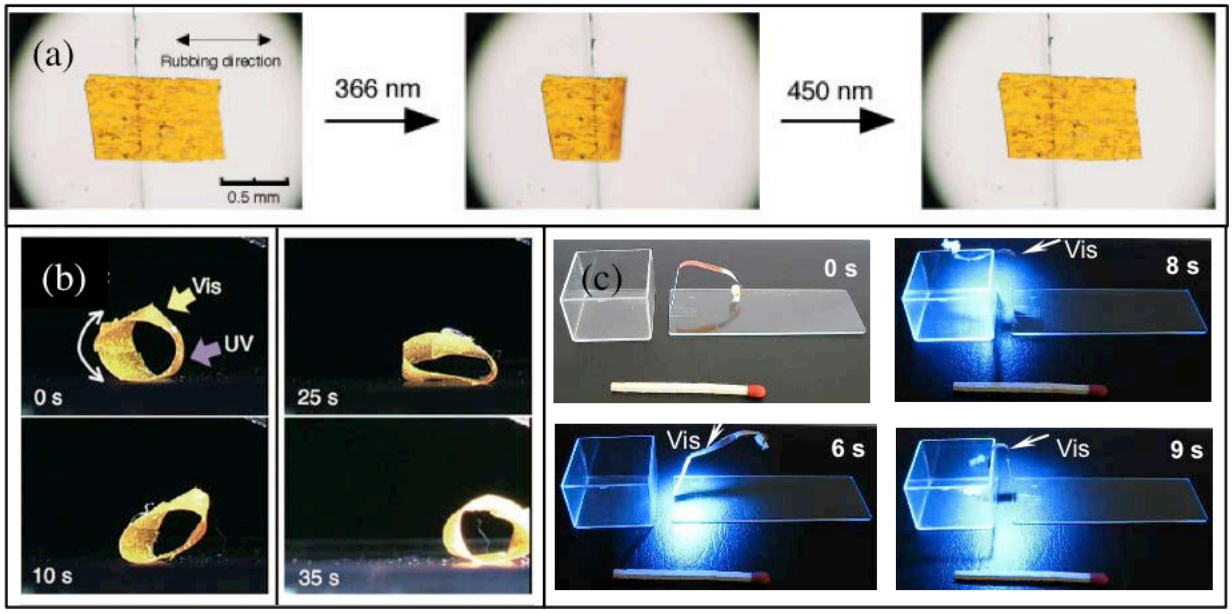

Fig 2.4.2-1 The various functions of LCE such as (a) bending and flattening [29] (b) rolling [31] (c) cantilever [32]

On the other hand, the light induced heat stimulation is rather simpler mechanism to create deformation. The fundamental concept is to make LCs reach phase transition by photon absorption and heat transfer. For example, single-walled carbon nanotubes (SWNTs) possess strong absorption in the visible/ near IR region and also behave as well thermal conductor to heat up LCE matrix in the SWNT-nematic-LCE nanocomposite. By switching on and off the IR stimulus, the nanocomposite film experiences reversible strain up to 30% [33].

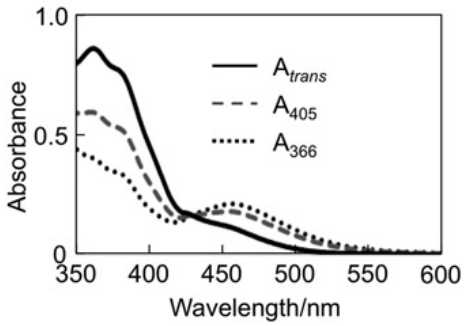

Fig 2.4.2-2 The spectrum change of LCE film under irradiation at various wavelengths [34]

To distinguish from two mechanisms, the absorption spectrum and the response time of LCE film are crucial tools. When azo dye absorbs UV and undergoes *trans* to *cis* transition, since the population of *trans*-form drops, an obvious decrease is observed at UV regime while an increase appears at visible regime consequently [34]. Concerning the response time of LCE

film, when turning off the stimulus the light induced heat approach gives rather quick reversible deformation while for the isomerization approach, the LCE film remains the same level of deformation but requires another wavelength as stimulus to regain original shape [7].

2.5 Summary

In this chapter we gave an overview of LC optical, thermal and elastic properties. By quickly going through dielectric anisotropy, four-parameter model for temperature effect, extended Cauchy's equation, and Fredericks threshold, several related pioneer works including stop band tuning in PhC-PDLC composite, light confinement in LC, and shift of guided modes in PCF are introduced. Furthermore, the mechanism and advanced functions of LCE are presented.

References

[1] J. Y. Hardeberg, F. Schmitt, and H. Brettel, "Multispectral color image capture using a liquid crystal tunable filter," *Optical engineering*, vol. 41, no. 10, pp. 2532–2548, 2002.

[2] M. Peccianti, C. Conti, G. Assanto, A. De Luca, and C. Umeton, "All-optical switching and logic gating with spatial solitons in liquid crystals," *Applied Physics Letters*, vol. 81, no. 18, pp. 3335–3337, 2002.

[3] A. Buguin, M.-H. Li, P. Silberzan, B. Ladoux, and P. Keller, "Micro-actuators: When artificial muscles made of nematic liquid crystal elastomers meet soft lithography," *Journal of the American Chemical Society*, vol. 128, no. 4, pp. 1088–1089, 2006.

[4] I.-C. Khoo, *Liquid crystals: physical properties and nonlinear optical phenomena*, vol. 64. John Wiley & Sons, 2007.

[5] I. Dierking, *Textures of liquid crystals*. John Wiley & Sons, 2006.

[6] "http://www.wikipedia.org/."

[7] H. Zeng, "Light Driven Microscopic Robot, PhD" *Università degli Studi di Firenze*, 2014.

[8] L. Scolari, "Liquid crystals in photonic crystal fibers: fabrication, characterization and devices, PhD" *Technical University of Denmark*, 2009.

[9] D.-K. Yang, *Fundamentals of liquid crystal devices*. John Wiley & Sons, 2014.

[10] I. Haller, "Thermodynamic and static properties of liquid crystals," *Progress in solid state chemistry*, vol. 10, pp. 103–118, 1975.

[11] J. Li, S. Gauzia, and S.-T. Wu, “High temperature-gradient refractive index liquid crystals,” *Optics express*, vol. 12, no. 9, pp. 2002–2010, 2004.

[12] J. Li, S. Gauza, and S.-T. Wu, “Temperature effect on liquid crystal refractive indices,” *Journal of applied physics*, vol. 96, no. 1, pp. 19–24, 2004.

[13] S. Gauza, H. Wang, C.-H. Wen, S.-T. Wu, A. J. Seed, and D. Roman, “High birefringence isothiocyanato tolane liquid crystals,” *Japanese journal of applied physics*, vol. 42, no. 6R, p. 3463, 2003.

[14] T. Larsen, A. Bjarklev, D. Hermann, and J. Broeng, “Optical devices based on liquid crystal photonic bandgap fibres,” *Optics Express*, vol. 11, no. 20, pp. 2589–2596, 2003.

[15] J. F. Henninot, M. Debailleul, F. Derrien, G. Abbate, and M. Warenghem, “(2D+ 1) Spatial optical solitons in dye doped liquid crystals,” *Synthetic metals*, vol. 124, no. 1, pp. 9–13, 2001.

[16] F. A. Jenkins and H. E. White, *Fundamentals of Optics*. McGraw-Hill, 1981.

[17] J. Li and S.-T. Wu, “Extended Cauchy equations for the refractive indices of liquid crystals,” *Journal of applied physics*, vol. 95, no. 3, pp. 896–901, 2004.

[18] Y. Arakawa, S. Nakajima, S. Kang, G. Konishi, and J. Watanabe, “Synthesis and evaluation of high-birefringence polymethacrylate having a diphenyl-diacetylene LC moiety in the side chain,” *Journal of Materials Chemistry*, vol. 22, no. 29, pp. 14346–14348, 2012.

[19] “http://plc.cwru.edu/.”

[20] T. Zhang, M. Kashima, M. Zhang, F. Liu, P. Song, X. Zhao, C. Zhang, H. Cao, and H. Yang, “Effects of the functionality of epoxy monomer on the electro-optical properties of thermally-cured polymer dispersed liquid crystal films,” *RSC Adv.*, vol. 2, no. 5, pp. 2144–2148, 2012.

[21] J. W. Doane, N. A. Vaz, B.-G. Wu, and S. Žumer, “Field controlled light scattering from nematic microdroplets,” *Applied Physics Letters*, vol. 48, no. 4, pp. 269–271, 1986.

[22] D. McPhail, M. Straub, and M. Gu, “Electrical tuning of three-dimensional photonic crystals using polymer dispersed liquid crystals,” *Applied Physics Letters*, vol. 86, no. 5, p. 051103, 2005.

[23] D. McPhail, M. Straub, and M. Gu, “Optical tuning of three-dimensional photonic crystals fabricated by femtosecond direct writing,” *Applied Physics Letters*, vol. 87, no. 9, p. 091117, 2005.

[24] H. Finkelmann, H.-J. Kock, and G. Rehage, “Investigations on liquid crystalline polysiloxanes 3. Liquid crystalline elastomers—a new type of liquid crystalline material,” *Die Makromolekulare Chemie, Rapid Communications*, vol. 2, no. 4, pp. 317–322, 1981.

[25] M. Warner and E. M. Terentjev, *Liquid crystal elastomers*, vol. 120. Oxford University

Press, 2003.
[26] J. Schätzle, W. Kaufhold, and H. Finkelmann, “Nematic elastomers: The influence of external mechanical stress on the liquid-crystalline phase behavior,” *Die Makromolekulare Chemie*, vol. 190, no. 12, pp. 3269–3284, 1989.
[27] J. Küpfer and H. Finkelmann, “Nematic liquid single crystal elastomers,” *Die Makromolekulare Chemie, Rapid Communications*, vol. 12, no. 12, pp. 717–726, 1991.
[28] K. D. Harris, C. W. Bastiaansen, J. Lub, and D. J. Broer, “Self-assembled polymer films for controlled agent-driven motion,” *Nano letters*, vol. 5, no. 9, pp. 1857–1860, 2005.
[29] T. Ikeda, M. Nakano, Y. Yu, O. Tsutsumi, and A. Kanazawa, “Anisotropic bending and unbending behavior of azobenzene liquid-crystalline gels by light exposure,” *Advanced Materials*, vol. 15, no. 3, pp. 201–205, 2003.
[30] Y. Yu, M. Nakano, and T. Ikeda, “Photomechanics: directed bending of a polymer film by light,” *Nature*, vol. 425, no. 6954, pp. 145–145, 2003.
[31] M. Yamada, M. Kondo, J. Mamiya, Y. Yu, M. Kinoshita, C. J. Barrett, and T. Ikeda, “Photomobile polymer materials: towards light-driven plastic motors,” *Angewandte Chemie International Edition*, vol. 47, no. 27, pp. 4986–4988, 2008.
[32] F. Cheng, R. Yin, Y. Zhang, C.-C. Yen, and Y. Yu, “Fully plastic microrobots which manipulate objects using only visible light,” *Soft Matter*, vol. 6, no. 15, pp. 3447–3449, 2010.
[33] L. Yang, K. Setyowati, A. Li, S. Gong, and J. Chen, “Reversible infrared actuation of carbon nanotube–liquid crystalline elastomer nanocomposites,” *Advanced Materials*, vol. 20, no. 12, pp. 2271–2275, 2008.
[34] M. Kondo, M. Sugimoto, M. Yamada, Y. Naka, J. Mamiya, M. Kinoshita, A. Shishido, Y. Yu, and T. Ikeda, “Effect of concentration of photoactive chromophores on photomechanical properties of crosslinked azobenzene liquid-crystalline polymers,” *Journal of Materials Chemistry*, vol. 20, no. 1, pp. 117–122, 2010.

Chapter 3 Light controlled by LC infiltrated PhC

There is a huge amount of work on LC integrated photonic devices. As shortly reviewed in Chapter 2, including LC cell [1], photonic crystal fiber [2], optical fiber [3] and polymer dispersed liquid crystal [4], liquid crystals are widely applied as tuning elements. Many devices as computer screens, mobile phones, etc. use this switching. Typically the size of cells for these widespread applications is of order of 5 - 25 μm and more [5]. In our work we follow more challenging task: embedding the LC in micro size (of order less than 1 μm) rods of photonic crystal and realizing LC-switching there. In this chapter we present our work on LC infiltrated woodpile PhC.

By using the direct laser writing 3D lithography technique, we first fabricate the polymer woodpile samples. Second we infiltrate the LC into PhC. For the molecules used (polymer: IP-Dip photoresist from Nanoscribe and LC: 5CB form Merck), the capillary forces suck the LC into the voids channels of the woodpile and fill all the voids completely. We use micro-pipette under polarized optical microscope to observe and control the process when capillary force brings LC molecules to enter void channels in the woodpile. Third, by assembling the measurement setup, we illuminate samples by laser (we use red: HeNe laser at 633 nm, green: DPSS laser at 532nm, tunable: Ti:Sapphire laser at 800nm) on the LC-PhC composite sample, control its temperature by hot plate, and record the transmission patterns.

First basic result is the tuning of spatial angular bandgap by the temperature, as externally controlled. The effect, from viewpoint of physics, is linear, since the transmission does not depend on the characteristics of the beam, for instance its intensity. These results here have been published in [6], which is one of major publications of the PhD results. Next in order to make the process nonlinear, we introduced small amount of absorber (dye: DO3 from Sigma-Aldrich) in infiltrated LC. The dye helps to absorb the radiation of the beam and thus makes the temperature of material dependent on intensity of the beam. Specifically we apply 532 nm semiconductor laser as a pump beam to heat the sample. The effect is nonlinear tuning of the transmission pattern. The nonlinear tuning has been achieved by the same

frequency (heating by green and probing by green) as well as by two frequencies (heating by green and probing by red). We do observe that the higher intensity at center of the pump beam makes the local refractive index change correspondingly and results in relevant wavefront modulation. These results are composed in second basic article of the thesis [7] (submitted).

Finally the attempts have been made to observe strongly nonlinear (solitonic) effect on self-confinement of intense beam. To clarify the effect is total nonlinear (i.e. the refractive index changes with beam intensity and affects the propagation itself), since the designed woodpile equips angular bandgap in visible regime, the experiment is further modified into single wavelength 532 nm playing role as both probe and pump beams.

3.1 Introduction to numerical methods and experiment

3.1.1 Numerical methods

<u>Paraxial model</u>

In order to understand spatial filtering, and to estimate the angles of spatial filtering lines, we first explore wave propagation in a medium with periodically modulated refractive index under paraxial model [8]:

$$\left[2ik_o\frac{\partial}{\partial z}+\nabla_\perp^2+2\Delta n(x,y,z)k_0^2\right]A(x,y,z)=0 \tag{3.1}$$

$A(x,y,z)$ is the slowly varying complex amplitude of the electric field in 3D space; (full electric field is: $E(x,y,z,t)=A(x,y,z)e^{ik_0z-i\omega_0t}+c.c.$) propagating along the longitudinal z-direction with the wave-number $k_0=n\omega_0/c$ (in a medium with average refraction index n and carrier frequency ω_0). $\nabla_\perp^2=\partial^2/\partial x^2+\partial^2/\partial y^2$ is the Laplace operator in the space transverse to the propagation direction where $r_\perp=(x,y)$ represents the

space perpendicular to the propagation direction and $k_\perp = (k_x, k_y)$ denotes the transverse components of the wave vector.

The refractive index profile for a rough estimation of the effects can be assumed to be harmonic function $\Delta n(x,y,z) = \Delta n_0/4\left(\cos(q_x x) + \cos(q_y y)\right)\cos(q_z z)$, where$q_i = 2\pi/d_i$ with $i \in \{x,y,z\}$ and Δn_0 is the maximum variation of the refractive index contrast. Next we expand the field by spatial harmonic components:

$$A(r_\perp, z) = \int e^{ik_\perp r_\perp}\left[A_0(k_\perp, z) + \sum_{m_x,m_y} A_{m_x,m_y}(k_\perp, z)e^{im_x q_x x + im_y q_y y - iq_z z}\right]dk_\perp \qquad (3.2)$$

In the expression above we consider only the dominant diffracted components $A_{m_x,m_y}(k_\perp, z)$ with $(m_x, m_y) = (\pm 1,0), (0,\pm 1)$, in addition to the zero component $A_0(k_\perp, z)$. This is justified by experimental observation where four diffraction maxima are clearly observed. By substituting the harmonic components into the wave equation, we obtain the following evolution of expansion coefficients along the propagation direction:

$$\frac{d}{dz}A_0 = -\frac{ik_\perp^2}{2k_o}A_0 + \frac{i\Delta n_0 k_o}{16}\sum_{m_x,m_y} A_{m_x,m_y} \qquad (3.3)$$

$$\frac{d}{dz}A_{m_x,m_y} = \left[\left(-\frac{i(k_x + m_x q_x)^2 + i\left(k_y + m_y q_y\right)^2}{2k_0}\right) + iq_z\right]A_{m_x,m_y} + \frac{i\Delta n_0 k_o}{16}A_0 \qquad (3.4)$$

The second equation (3.4) illustrates a coherent transfer of the radiation from the zero diffraction component $k_\perp = (k_x, k_y)$ to the diffraction components $(k_x + m_x q_x, k_y + m_y q_y)$. The first equation (3.3) describes an inverse process: the intensity increase of the zero order component due to back-scattering from non-zero diffraction components. The scattering is most efficient for the angles $k_\perp$ corresponding to the resonant interaction between the zero order and one or several of the diffracted components. The resonance condition can be expressed in following form:

$$(k_x + m_x q_x)^2 + \left(k_y + m_y q_y\right)^2 - 2q_z k_0 = k_x^2 + k_y^2 \qquad (3.5)$$

This condition leads to four dark crossing lines in $k_\perp$ space, with each line corresponding to a specific set of (m_x, m_y), i.e. to the coupling with a specific diffracted component. Physically speaking the emergence of dark lines represents the efficient (resonant) coupling with the related diffracted components. The pattern of the lines, i.e. the separation angle between each pair of parallel lines, can be controlled by modifying the parameters of the photonic structure for the same wavelength or varying the wavelength for the same structure. For example all four dark lines assemble at the center $k_x = k_y = 0$ for $q_x^2 = q_y^2 = 2\ {}_0 q_z$.

The resonance condition can be used to calculate the angles of the dark lines with respect to the optical axis. In particular for $(m_x, m_y) = (+1,0)$ the resonance line appears at the following location in angular space,

$$\frac{k_x}{k_0} = \frac{q_z}{q_x} - \frac{q_x}{2k_0} = \frac{q_\perp}{2k_0}(Q-1) \tag{3.6}$$

where the geometry parameter $Q = 2d_\perp^2 n/(\lambda d_\parallel)$, Eq. (3.6) is equivalent to:

$$\sin(\alpha) = \frac{\lambda}{2d_\perp}\left(\frac{2d_\perp^2 n}{\lambda d_\parallel} - 1\right) \tag{3.7}$$

here α describes the angles of the dark lines observed in our experiments. Here n is the average refractive index, $d_\parallel$ and $d_\perp$ are the longitudinal (along z axis) and the transverse periods (along x or y axis) of the modulation, λ is the wavelength of the incident wave. In order to obtain an observable and controllable filtering effect we designed and built the structures to filter at small angles $\alpha \ll 1$, which led to the particular geometry of the woodpile structure (the longitudinal and transverse periods). With the chosen periods (the longitudinal period $d_\parallel = 4\ \mu$m, and the transverse period $d_\perp = 0.85\ \mu$m), we expected to observe filtering at angles of a few degrees, which is convenient for experimental observations. Note that the expressions for the angles of filtering lines (3.5) - (3.7) have been obtained in paraxial approximation, which is strictly valid for $\lambda \ll d_\perp, d_\parallel$. Generally the full treatment results in filtering angles slightly different from calculated under paraxial approximation (see ref. [9]).

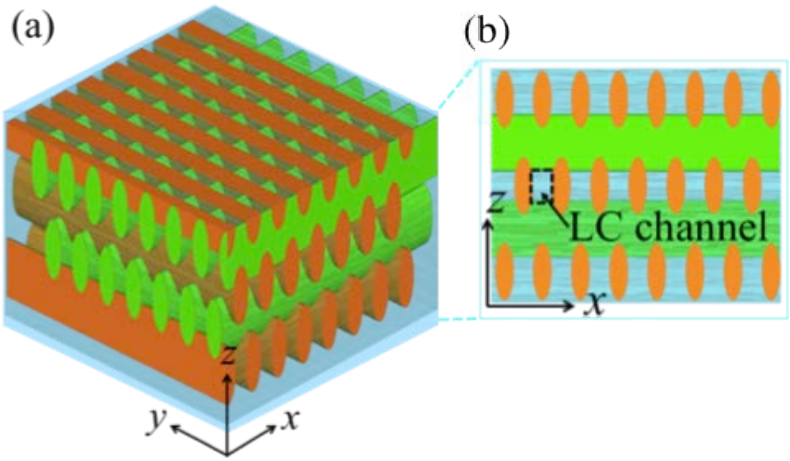

Fig 3.1.1-1 Schematic representation of LC infiltrated 3D woodpile (a). The inset illustrates the channels at indicated cross section in *xz* plane (b). The LC enters into the channels due to capillary forces. The indicated horizontal channels are interconnected by vertical channels (not visible from this perspective).

FDTD Simulation

For the numerical calculations we have used a commercial Finite Difference Time Domain (FDTD) software (CrystalWave, Photon Design). For the input source we used a monochromatic Gaussian beam, incident normally into the structure. A spatial filtering effect is obtained in the far field pattern of the transmitted beam for both the nematic and isotropic states of LC. In order to simplify the 3D calculations, the 3D hybrid woodpile-LC configuration was decomposed into separated 2D configurations. This is possible if the 3D refractive index distribution $n(x,y,z)$ can be decomposed into $n(x,y,z) = n_x(x,z) + n_y(y,z)$, which is (approximately) the case of woodpile photonic crystals. Then, in the paraxial approximation (which does not take into account the back-reflection, and assumes that the diffraction angles are not too large to the propagation direction *z*), the field can be factorized $A(x,y,z) = A_x(x,z) \cdot A_y(y,z)$. Therefore the 2D numerical calculations can be performed separately for both field quadratures, highly reducing computational efforts. Specifically the beam propagation patterns were calculated by 2D FDTD to obtain two 2D cross sections (*xz* and *yz* plane) as shown in Fig 3.1.1-1. After Fourier transform, the far fields of two field quadrature directions were obtained. The full 2D cross section of the transmitted pattern in far field is then recovered using the factorization property. Note that this approach is approximate and valid only in paraxial approximation $\lambda \ll d_\perp, d_\parallel$ and for decomposable woodpile structure, where the woodpiles just touch. Reality is different: the paraxial treatment

is on the limit, and also the woodpiles not just touch but usually fuse one into another. Therefore, speaking in advance, the experimentally observed distributions are not factorizable, however most frequently, almost factorizable.

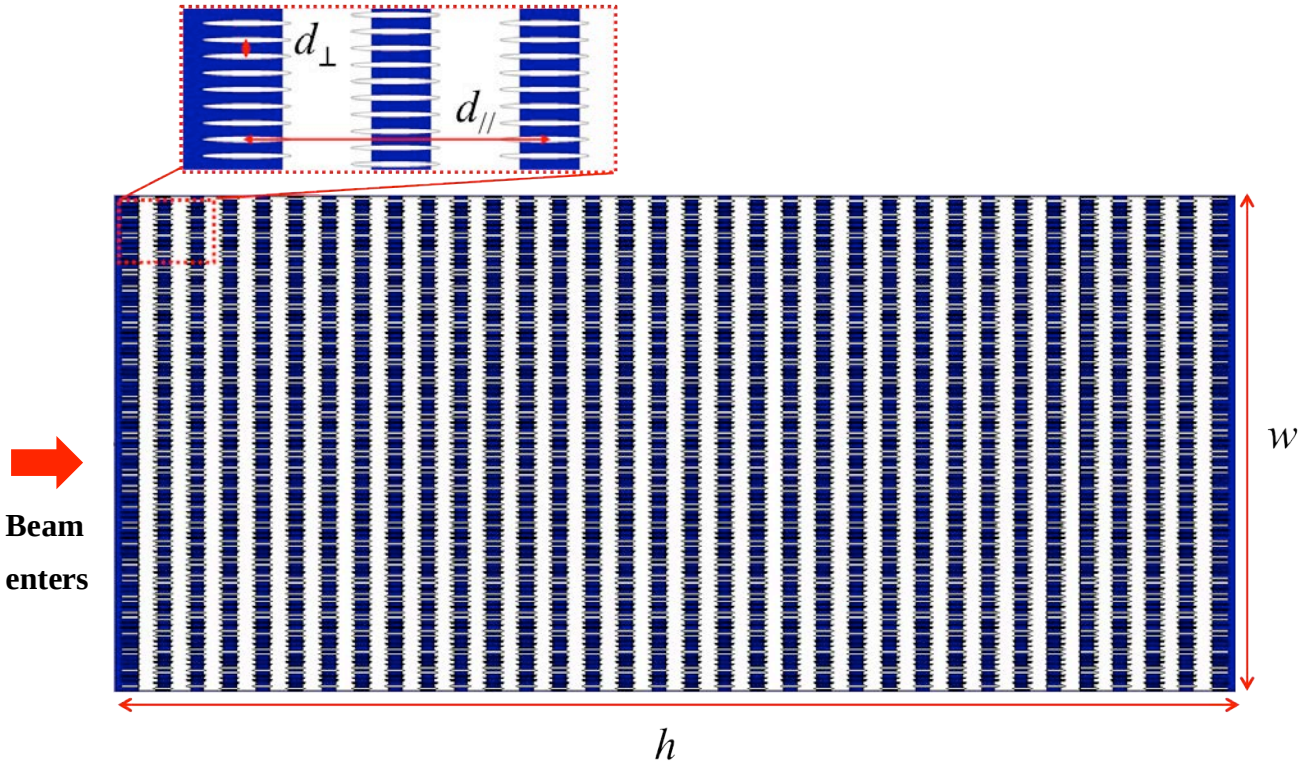

Fig 3.1.1-2 Design of woodpile structure and the refractive indices used in FDTD calculations. The woodpile height h = 68 μm and width w = 80 μm. Note that here the woodpile is "viewing on side". The inset on the top indicates the longitudinal period $d_{\parallel} = 4\ \mu$m and transverse period $d_{\perp} = 0.85\ \mu m$. White and blue regions refer to the different refractive indices for polymer structure n_p and liquid crystal background n_{LC} (either n_e, n_o or n_i).

Given the longitudinal and transverse periods of polymer rods in lattice with triangular symmetry as shown in Fig 3.1.1-2, we further slightly modify the parameters (wavelength, refractive index, and incident beam waist) in order to optimally adjust to experimental results. With this adjustment we compensate the discrepancies appearing due to the factorization procedure. Typical field distributions observed by FDTD calculation are given in Fig 3.1.1-3.

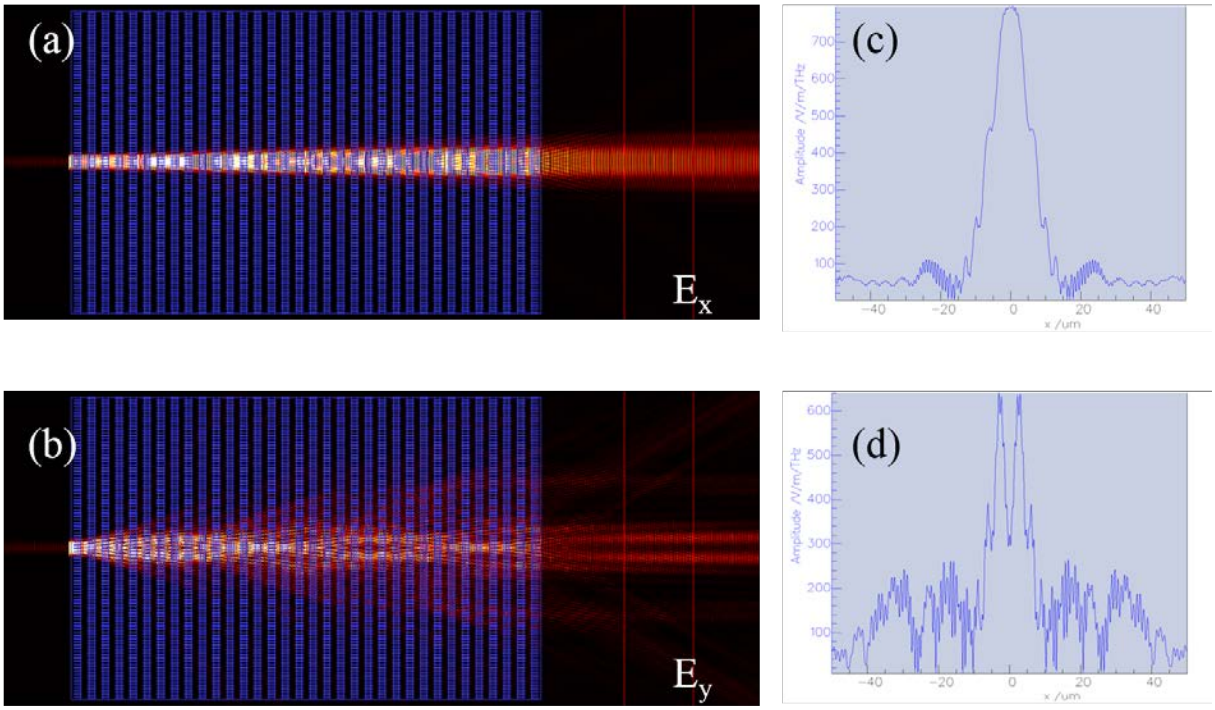

Fig 3.1.1-3 The electric field distributions obtained by FDTD calculations for TE (o-polarization) (a) and for TM (e-polarization) (b) for 633 nm. The 1D near field distribution behind the photonic crystal (along red cut line) in transverse direction for TE (c) and TM (d) polarizations.

3.1.2 Experiment process – woodpile fabrication

The woodpiles were fabricated by Direct Laser Writing (DLW) using a negative photoresist, IP-Dip (we used commercial equipment by Nanoscribe GmbH). The tightly focused femtosecond laser beam (130 fs pulse duration, 780 nm wavelength, 100 MHz repetition rate) 100x objective (NA 1.3) results in a solidification volume of ellipsoidal shape (0.25 μm width and 1.25 μm height with aspect ratio of 0.2) due to two photon absorption polymerization. A sample translation writing speed is chosen as 100 μm/s and the laser power is measured to be 5.8 mW in front of the objective. Fig 3.1.2 shows the Scanning Electron Microscope (SEM) images of the woodpile, which is composed of the gratings of polymer piles stacking in the longitudinal direction with four layers resulting in one period (every second layer is half-period shifted and every adjacent layer is 90°- rotated). The woodpile contains 17 periods in a total height of 68 μm, hence it shows 11% shrinkage on the top layers.

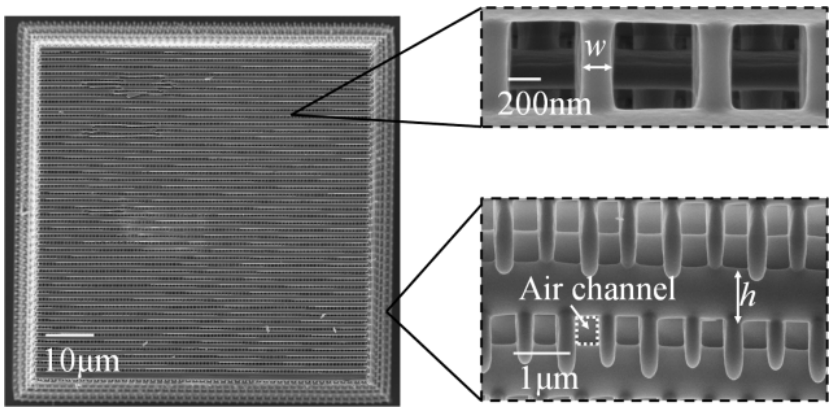

Fig 3.1.2 SEM images of the fabricated woodpile structure before filling the air channels with LC.

3.1.3 Experiment process – infiltration

A micropipette is used to infiltrate the LC material (5CB, Sigma Aldrich) into the woodpiles with the help of a 3-axis translation stages as schematically illustrated in Fig 3.1.3. Strong capillary force results in complete filling of the woodpile voids, while surface anchoring induces self-orientation of the LC molecules. The majority of LC molecules orient parallel to the surface (along channels). The multiple layers consist of alternate polymer woodpiles (n_p = 1.54 at 632.8nm) and LC tubes (n_e = 1.709, n_o = 1.53, n_i = 1.588 at 632.8nm), where n_e and n_o represent refractive indices for the extraordinary and ordinary polarizations of LC in the nematic phase and n_i is the average index for any linear polarizations of LC in isotropic phase.

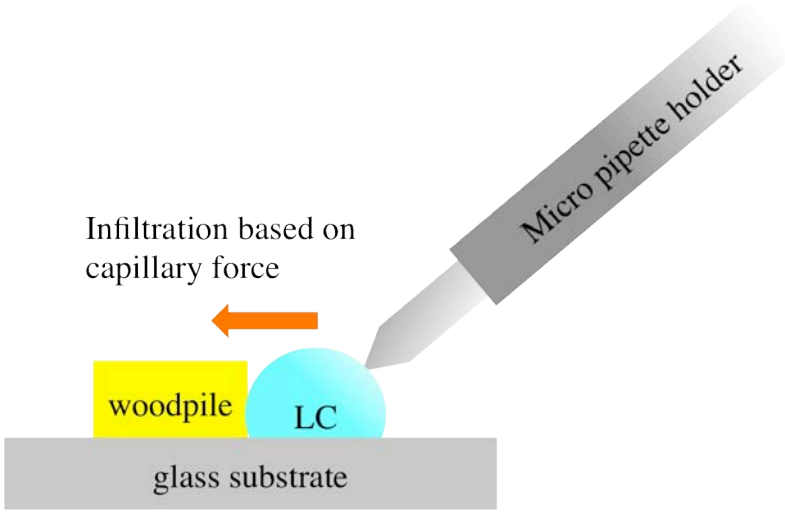

Fig 3.1.3 Schematic illustration of LC infiltration into woodpile based on capillary force

In the isotropic phase, the molecules are oriented completely randomly. In the nematic phase, the orientation along the channels results in periodic orientation structure. Generally the orientation in nematic phase is complicated due to interconnection of differently oriented channels. Therefore during our measurement, several rich and complicated diffraction patterns are observed and demonstrated in following sections.

3.1.4 Experiment process – measurement setup

In the experiment we focused a continuous 632.8 nm HeNe laser beam into the woodpile samples using a 50x long working distance objective. The numerical aperture (NA) of the objective is 0.55. The focused beam waist is around 2 μm. The method of recording the far field emission pattern, using spatial filtering, is schematically illustrated in Fig 3.1.4(a). A heating stage with resolution 0.1°C is used to precisely control the sample temperature, in order to switch the LC component between the nematic and isotropic states.

The measured far field diffraction pattern is shown in Fig 3.1.4 (b). The diffraction maxima appear at the angle of 49° corresponding to the lateral periodicity of the structure. For a quantitative characterization of the transmitted pattern we recorded only its central part (zero diffraction maximum) by placing the screen (camera) at a distance of 30 cm behind the sample. The recording of the far field pattern is confined in a maximum angle of 5.6° (Fig 3.1.4(c)). A spatial filter composed of two 10x objectives and a 25 μm diameter pinhole is used to expand the diameter of incident beam (for broader angular spectrum). A half-wave plate was used to switch the polarization of incident beam between *x* and *y* directions.

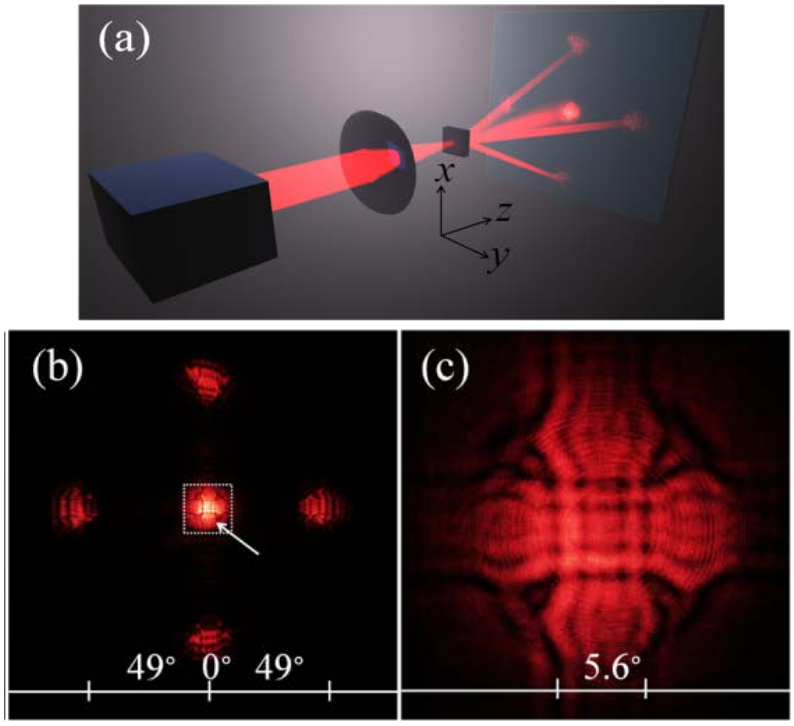

Fig 3.1.4 Schematically shown experimental setup (a), and typical distribution of transmission pattern containing central (zero) diffraction spot, and four first order diffraction spots (b) and the zoom of its central part (c).

3.2 Switching controlled by external heating

3.2.1 Thermal control

As mentioned in Section 2.2, when applying external heater and changing the temperature of LC sample, the thermal motion of the molecules would change the orientation of LC molecules. Therefore the optical properties of composite LC-PhC structure would change due to the change of refractive indices of LCs. The typical phase transitions as tuning tools are transitions between the nematic and isotropic states, which demonstrate clear dielectric anisotropy and isotropy respectively. The commercial LC 5CB used in our experiment has positive index thermal gradient dn_o/dT for ordinary polarization but negative gradient dn_e/dT for extraordinary polarization as reported by Li [10]. Concerning the slope, the decrease of n_e is steeper compared to the increase of n_o, therefore the average index of the LC-PhC composite medium decreases after reaching the isotropic state. The sharpness of dark filtering lines increases with the enhancement of the index contrast. By using this sensibility to the

index contrast from such device, we can tune the angular bandgaps (the angles of filtering lines) and change the diffraction patterns. On the contrary, the location of filtering lines could also reveal the information (like average refractive index) for sample filled by unexplored LC material (unknown n_o and n_e).

3.2.2 Experiment results

Temperature and Polarization dependence

Fig 3.2.2-1 shows the measured far field spatial filtering patterns within zero diffraction maxima. The distributions show a clear presence of dark lines - deflected angular components within the central maximum, which depend on the polarization of the light and the LC state. In the nematic phase (22°C), refractive index variations of 0.01 ($n_p - n_o$) and 0.169 ($n_e - n_p$) differ strongly in each woodpile layer. For the X-polarized beam, the angle of the horizontal filtering lines is measured to be 1.8°, and of the vertical filtering lines 5° from the optical axis (Fig 3.2.2-1 (a)). For the Y-polarized beam the angles of horizontal and vertical filtering lines are interchanged (Fig 3.2.2-1(b)). In the isotropic phase (40°C), a low refractive index variation of 0.048 ($n_i - n_p$) shows smaller contrast of the filtering lines. The transmission pattern is observed for filtering angles at 1.2° and 2.8° in both directions (Fig 3.2.2-1(d)). Such 90°- rotation invariant pattern shows no change by rotating the polarization of incident beam.

The experimentally recorded patterns correspond well to those obtained by numerical FDTD calculations, as shown in Fig. 3.2.2-1 The results for the X-polarized beam (Fig 3.2.2-1(a) and (e)) show filtering angles in the *x* and *y* directions. The y-averaged 1D intensity distributions (Fig 3.2.2-1(i-l), along the *x* direction) show a good agreement between the experimental results (blue), 5° in the *x* direction (Fig 3.2.2-1(i)) and 1.8° in the *y* direction, and the simulated ones (red), 4.5° (Fig 3.2.2-1(i)) and 2°, respectively. The patterns of the Y-polarized beam (Fig 3.2.2-1(b), (f) and (j)) are simply rotated 90° comparing to the ones for the X-polarized beam. The transmission pattern of 45°- polarization light is an average between patterns of the X- and Y- polarizations. In the isotropic phase, the polarization nonsensitive filtering angles are obtained at 1.2° and 2.8° in both directions, compared to two filtering lines at 3.5° and 5.2° in calculations. Note that double filtering angles were obtained in this case both in experiment and numerical simulations. The reason for two filtering lines is possibly, higher order resonance, with higher diffraction orders. The mode expansion (3.2) considers

only first harmonics of index modulation. Possibly the higher modulation harmonics come into play, resulting in higher order diffraction mode and correspondingly the other filtering lines are at small angles. The slight discrepancy of filtering angles between the experimental and numerical results, could be due to imperfections like shrinkage, and thermal expansion of the fabricated structure. The real structure shows some rounded edges at the junctions of the woodpiles, which brings some discrepancy from the decomposition condition $n(x,y,z) = n_x(x,z) + n_y(y,z)$ used in numerical simulations. Further possible reason for this small discrepancy is that the diffraction angles are relatively large, around 50°, which violates the paraxial condition.

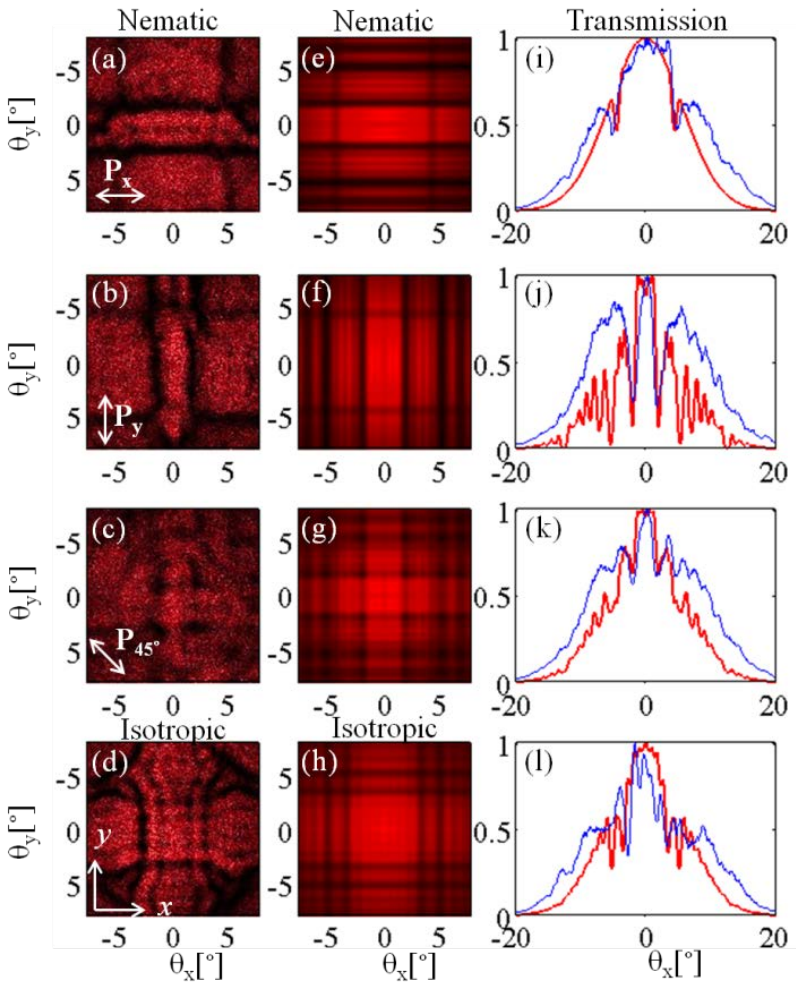

Fig 3.2.2-1 2D far field distributions of the central part of transmitted beam as obtained by measurement (a,b,c,d) and FDTD calculations (e,f,g,h). The right column (i,j,k,l) compares the 1D intensity distributions along the *x* direction (integrated along the *y* direction) obtained from experiments (blue-solid) and from FDTD numerics (red-solid). The rows correspond to: the X-polarized beam (a,e,i); the Y-polarized beam (b,f,j); and 45°-polarized beam (c,g,k). The bottom row (d,h,l) corresponds to the isotropic phase of the LC (independent on polarization)

Wavelength dependence

The wavelength dependence enters through the geometry parameter $Q = 2d_{\perp}^{2}n/(\lambda d_{\parallel})$; According to Eq. (3.7), the filtering angle is wavelength dependent. When the parameter Q is close to 1 (it happens at around 570 nm for given longitudinal and transverse periods), the filtering angle decreases to zero and therefore parallel dark lines are merged into one (see Fig 3.2.2-2) [11]. On the contrary, when Q is more different from 1, larger or smaller, the filtering angle increases and makes dark crossing lines separated.

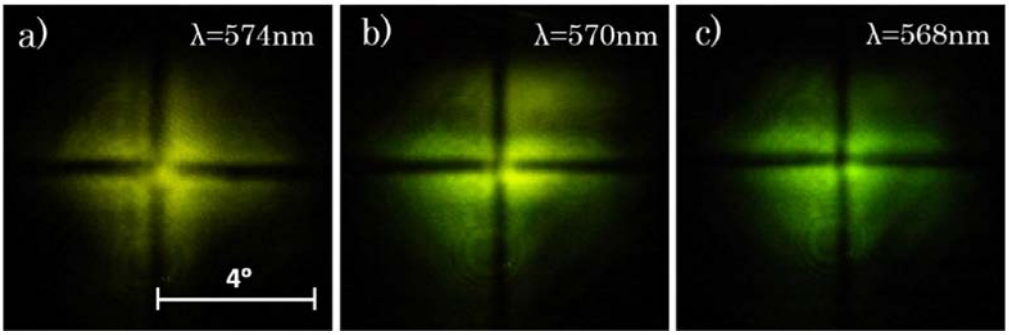

Fig 3.2.2-2 Angular filtering patterns observed in PhC made of fused silica glass bulk at (a) 574 nm, (b) 570 nm, and (c) 568 nm where dark parallel lines merges into one [11]

Apart from the nearly-parallel crossing lines (in square shape) observed in usually used polymer matrix (see Fig 3.2.2-3 (a) and (d)). In Fig 3.2.2-3 we also demonstrated the more complicated angular filtering patterns of LC-PhC composite sample at 532 nm and 633 nm in the nematic and isotropic states respectively. Due to the anisotropy of refractive indices of LCs in the nematic phase, the shape of crossing lines is of rectangle shape, i.e. the transverse cross-sections show either larger or smaller filtering angles in the vertical or horizontal directions. On the other hand, the isotropic refractive index of LC gives equivalent filtering angles in both vertical and horizontal directions in the isotropic phase.

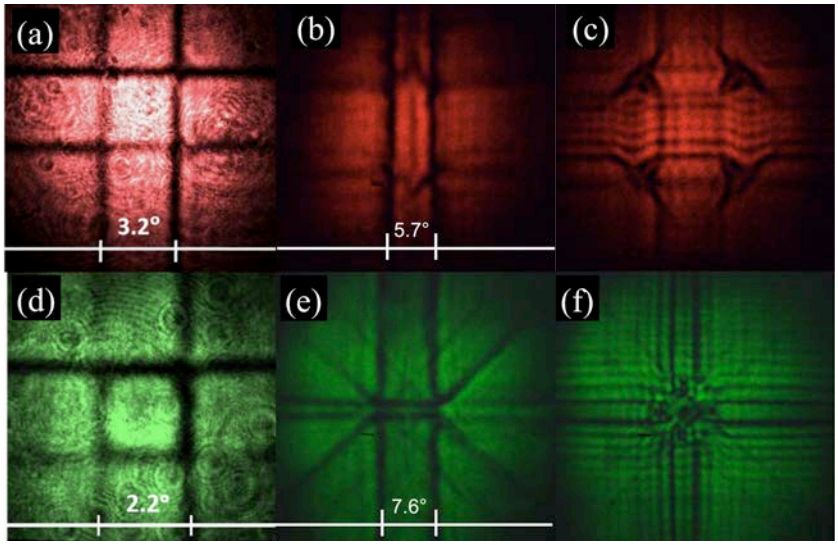

Fig 3.2.2-3 Typical square filtering patterns observed in PhC made of fused silica glass bulk at 633nm (a) and at 532nm (d) [11]. Complicated patterns observed in LC-PhC composite for 633 nm at nematic (b) and isotropic (c) states; for 532 nm at nematic (e) and isotropic (f) states. The polarization of the incident beam is kept Y-polarized.

Note that in some cases (especially the diagonal dark lines in (b) and (e) panels of Fig 3.2.2-3) the patterns are less factorizable. Note that only horizontal and vertical lines appear in factorizable patterns. To facilitate the investigation of the wavelength dependence, we use a supercontinuum source pumped by a 800nm Ti:Sapphire Laser in our experimental measurements. Several wavelengths with 10 – 20 nm per step (505 nm, 526 nm, 532 nm, 553 nm, 573 nm, 593 nm, 614 nm, 632 nm, 654 nm) are chosen by a monochromator. The beams are focused with 50x 0.55 NA objective onto the sample. The far field distributions are recorded with a paper screen and photo camera behind the sample.

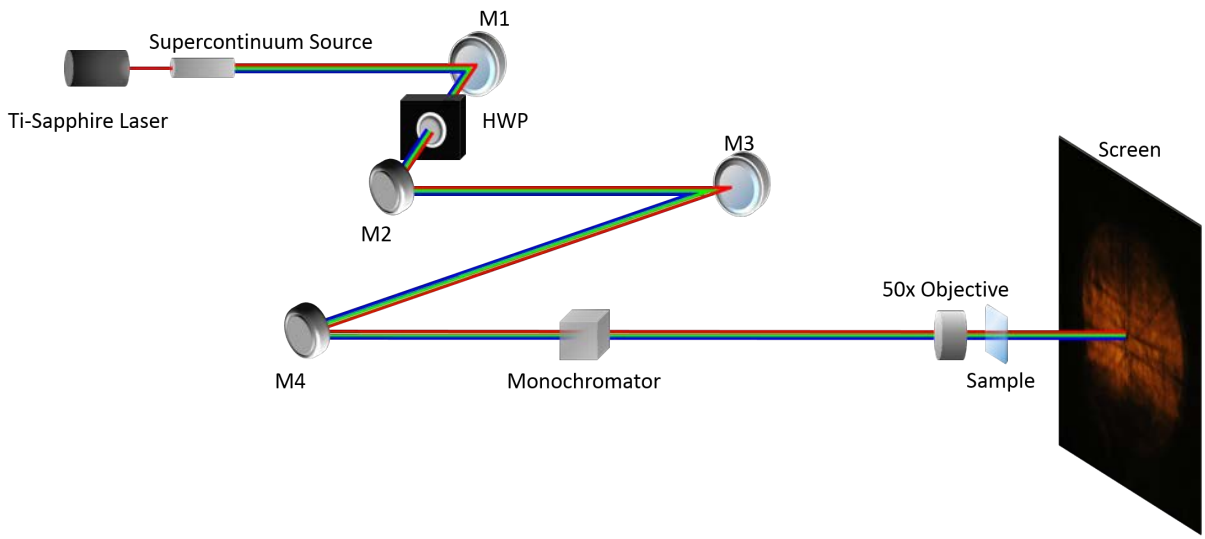

Fig 3.2.2-4 Schematics of optical system for measurement setup with a monochromator to select different wavelengths from the output of supercontinuum source

Our measurement results are demonstrated in Fig 3.2.2-5, the colorful filtering patterns (scanning from blue to red through nearly all the visible) clearly show the parallel dark lines approaching and expanding in either the vertical or horizontal directions for LCs in the nematic phase.

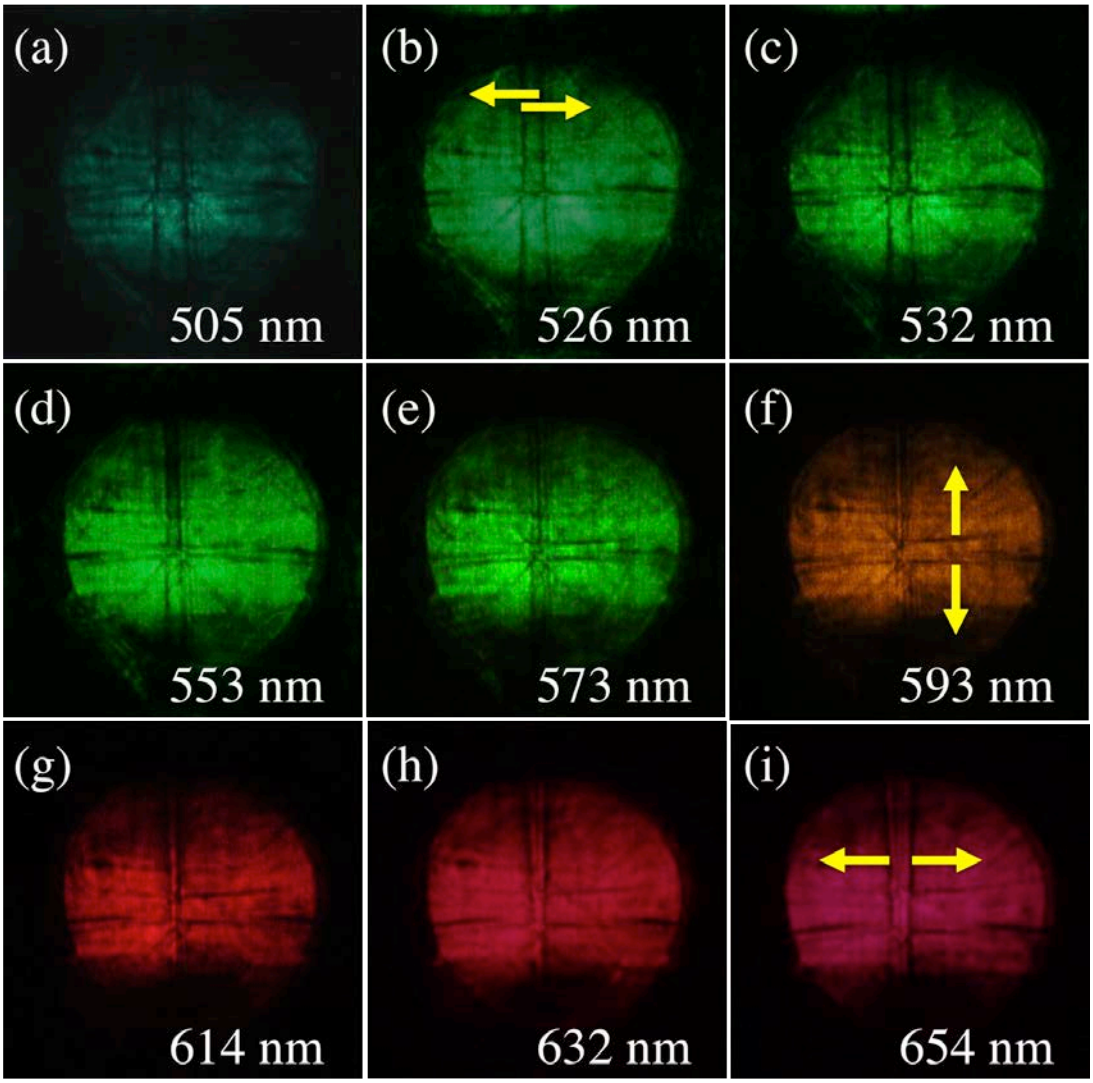

Fig 3.2.2-5 2D far field distributions of the central part beam observed in LC-PhC composite by varying the wavelengths of incident beam: (a) 505 nm, (b) 526 nm, (c) 532 nm, (d) 553 nm, (e) 573 nm, (f) 593 nm, (g) 614 nm, (h) 632 nm, (i) 654 nm which give firstly approaching and later expanding dark filtering lines in the nematic state. The polarization of the incident beam is kept Y-polarized. Arrows indicate the variation of the positions of dark lines with increasing wavelength.

3.3 Switching controlled by extra beam

3.3.1 Review of optical control

As a natural extension of the work described in the previous section, we consider next the use of an extra intense laser to tune the diffraction pattern. Dye-doped liquid crystals are material widely used to achieve different purposes e.g. heating [12] [13] or lasing [14] [15] among various photonic devices. In this section, the heating was achieved by an external powerful beam (specifically of green color) and the switching was observed for weak red color beam. One can consider the effect as linear switching, the external heater substituted by a laser beam. One can consider this as a nonlinear effect since here the linear light superposition effect is violated, and transmission of one beam depends on the intensity of another one.

General definition see for the instance [16], the change of the refractive index depending on the intensity of light is the key to distinguish between linear and nonlinear effect. If the change of the index is proportional to the applied field, the consequent response remains linear such as Pockels effect (also called electro-optic effect) observed in crystalline. While the change of the index is proportional to the square of the field, the consequent response is nonlinear, e.g. the DC Kerr effect observed in liquids or amorphous solids.

Being specific, the optical Kerr effect (also called AC Kerr effect) is a self-induced response by light. Due to the strong electric field of light, the variation of material index is proportional to the intensity of incident beam, therefore nonlinear effects such as self-focusing/ defocusing and self-phase modulation are observed correspondingly. The intensity distribution of laser beam is generally in Gaussian shape. It makes the host medium (such as LCs) to form a Gaussian refractive index profile when intense beam passes through. Hence such gradient-index profile could compensate diffraction and result in confinement to light, so called self-focusing effect.

3.3.2 Experiment results

<u>The phase transition achieved by external heater</u>

In order to compare the difference between heating achieved by external heater and green

laser respectively, here we recorded carefully how the filtering patterns evolve when the temperature increases. Fig 3.3.2-1 shows that the sharpness of vertical filtering lines observed at nematic phase first decreases and becomes barely visible at the transition point due to scattering associated with two phases co-existence. After reaching the isotropic phase, the filtering angles became equal along both horizontal and vertical directions.

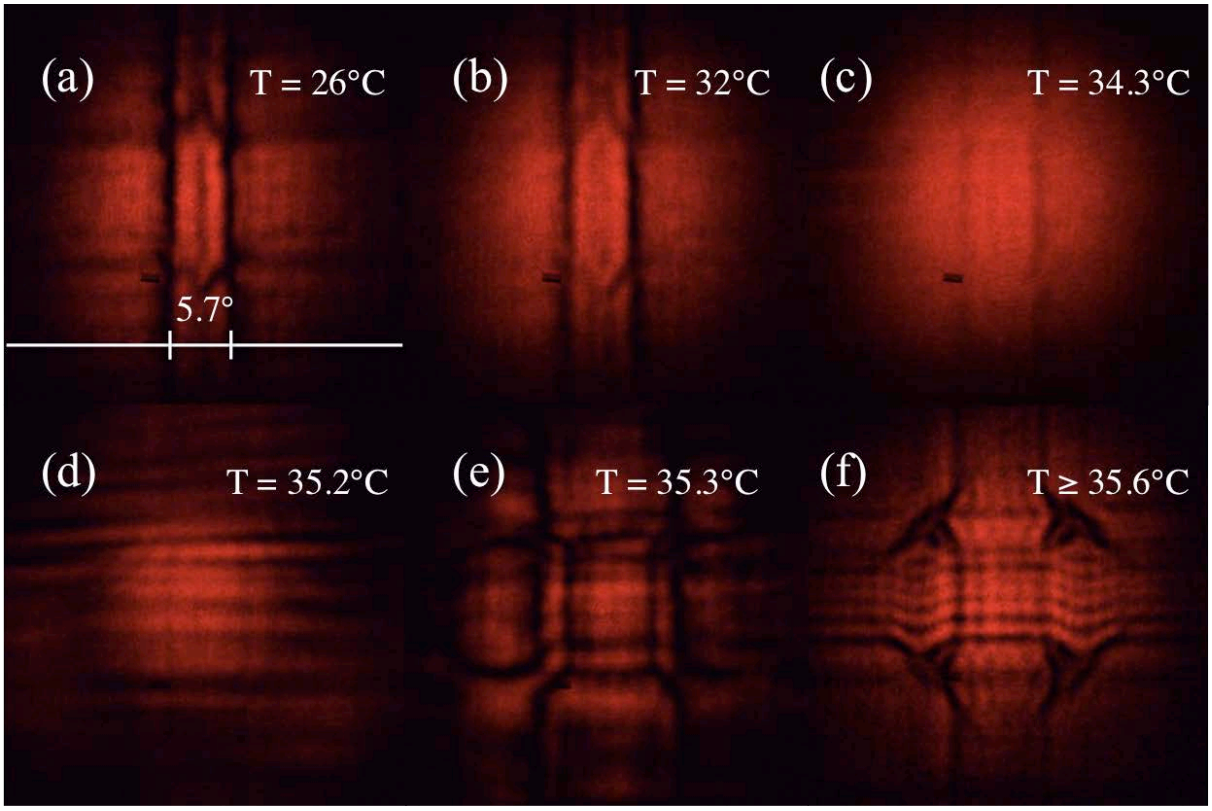

Fig 3.3.2-1 Snapshots taken from the video record of far field transmission pattern for temperature gradually increasing with rate 1°C/ min. The angular transmission patterns gradually change from those typical to the nematic (a) to the isotropic state (f), the temperature was changed isotropically with the external heater warming from 26°C to 36°C. When the temperature rises, the sharpness of dark lines first decreases (b), becomes barely visible (c) and then evolves into the square symmetric patterns (e-f). The polarization of the incident beam is kept Y-polarized.

The measurement setup is schematically shown in Fig 3.3.2-2. In order to expand the diameter of the probe (red) beam (to be able to record broader angular spectrum), a spatial filter (SF) composed of two 10x objectives and a 25 μm diameter pinhole is used. The half-wave plate (HWP) is added to control the linear polarization of incident beam.

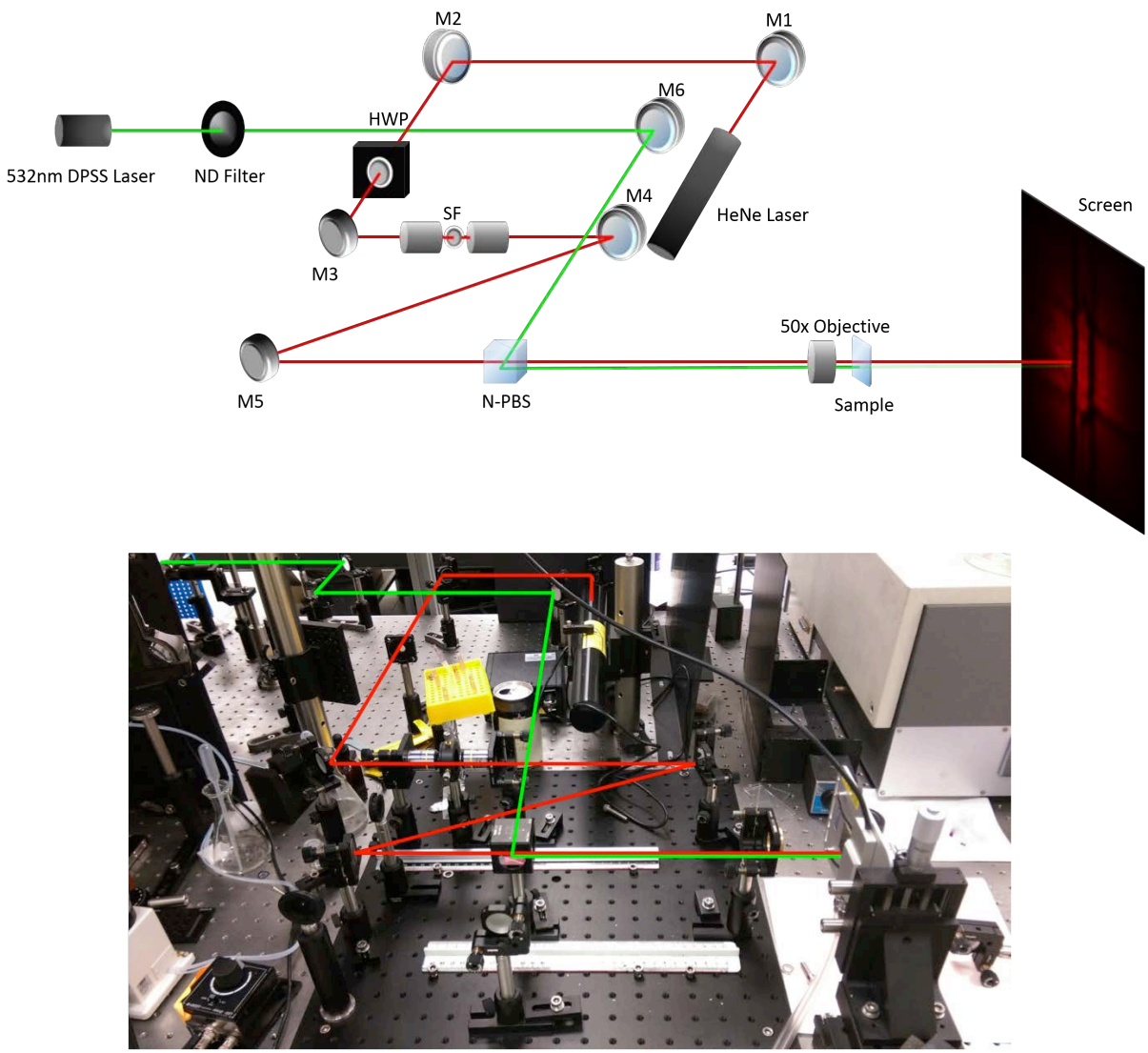

Fig 3.3.2-2 Schematics of optical system (a) and real photograph (b) of measurement setup with spatial filter functioning as beam expander

The phase transition achieved by Green laser excitation

The LCs background of our composite sample used here is doped with 2% wt. commercial DO3 dye (Sigma-Aldrich). Like its color appearing in orange, the dye molecules strongly absorb the light in green region and locally heat the sample by releasing energy. Although the presence of dye generally increase the average refractive index of the composite medium, due to the low concentration the influence on the refractive index is simply negligible.

When the intensity of the green (excitation) laser is low, the filtering patterns in the nematic state remain rectangular and symmetric in vertical and horizontal directions as shown in Fig 3.3.2-3 (a) and (b). However when we further enhanced the intensity, the square symmetric

transmission pattern appeared as shown in Fig 3.3.2-3 (e) and (f). The drawback of the green laser excitation scheme is that when the intensity is enhanced too much, it first gives the superposition patterns of two beams and later damages the sample due to the burning of dye.

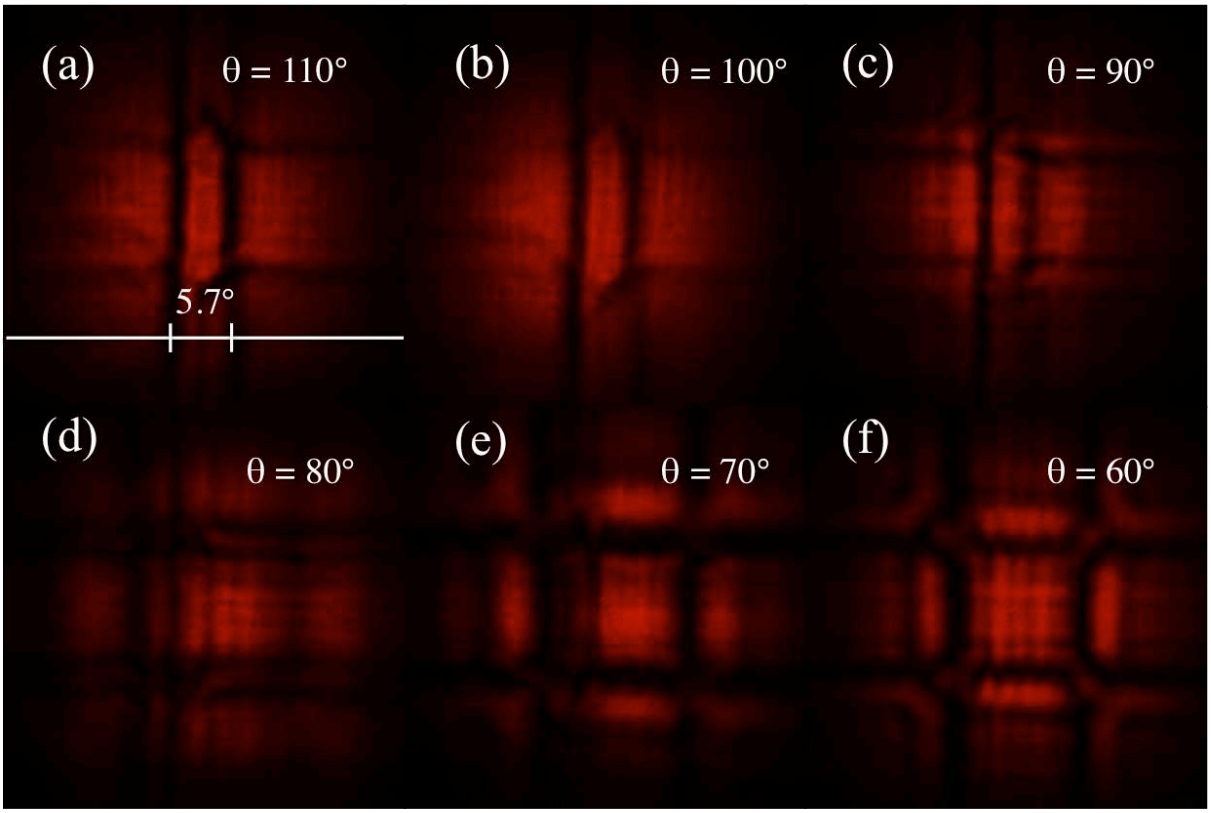

Fig 3.3.2-3 2D far field distributions of the central part of the beam when temperature increases locally by rotating 10° per step of the ND filter whose optical density is a linear function of θ. The angular filtering patterns change from the ones typical to the nematic phase (a) to the isotropic state (f) with pump (532 nm) and probe beams (633nm). When the intensity of green laser increases, the sharpness of dark lines starts to decrease (b), following several transition patterns (c-d), then evolves into the square symmetric patterns (e-f). Similar patterns are observed between (b) and Fig 3.3.2-1(b), also (f) and Fig 3.3.2-1(e). The polarization of the incident beam is kept Y-polarized.

From the comparison between Fig 3.3.2-1 and Fig 3.3.2-3, we found that the benefits of tuning angular filtering with green laser and ND filter are: 1) each temperature step change could be very small (less than 0.1°C) and relatively continuous in order to observe rich variety of the dynamic filtering patterns near the transition point. 2) The local heating position could be well controlled by adjusting the green beam excited location with the reflective mirror.

The measurement setup is depicted in Fig 3.3.2-4. A continuous ND filter is used to control the intensity of CW 532 nm DPSS laser beam. The spatial filter inserted here is to clean the green Gaussian beam. The 532 nm pump beam's absorption length is smaller than the sample height, i.e. it can be absorbed mostly inside LC while the weak signal transmits to the screen. Both pump (green) and probe (red) beams are guided to the sample through a non-polarizing 50:50 beam splitter (N-PBS). The excited power for the 2% dye-doped LC is 0.04 - 0.16 mW when the beam is focused into about 2.5 μm (FWHM) which corresponds to the irradiance around 0.81 – 3.26 kW/ cm^2.

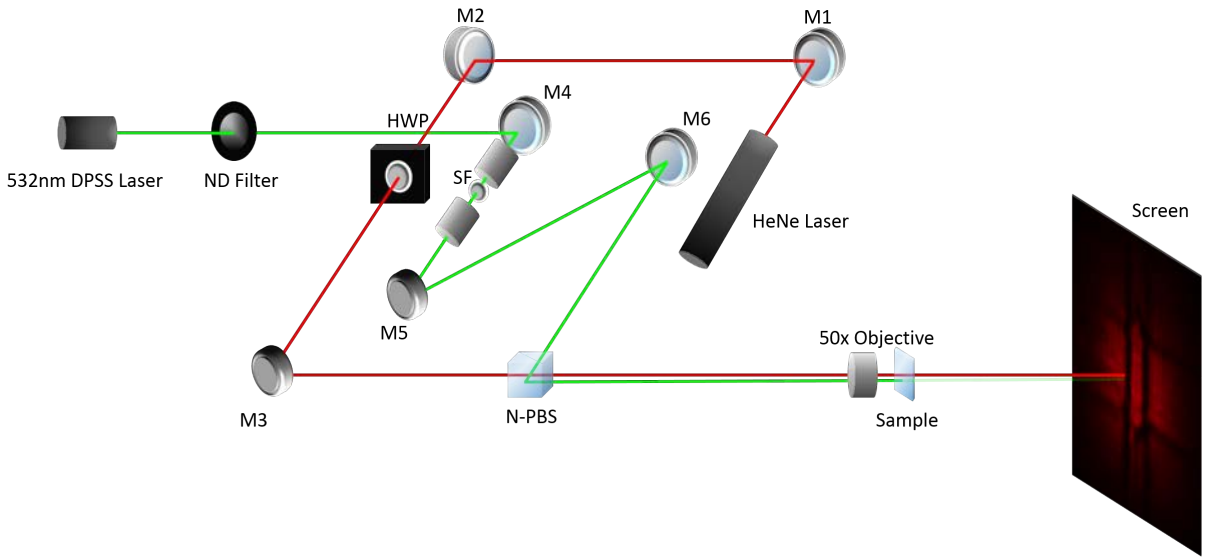

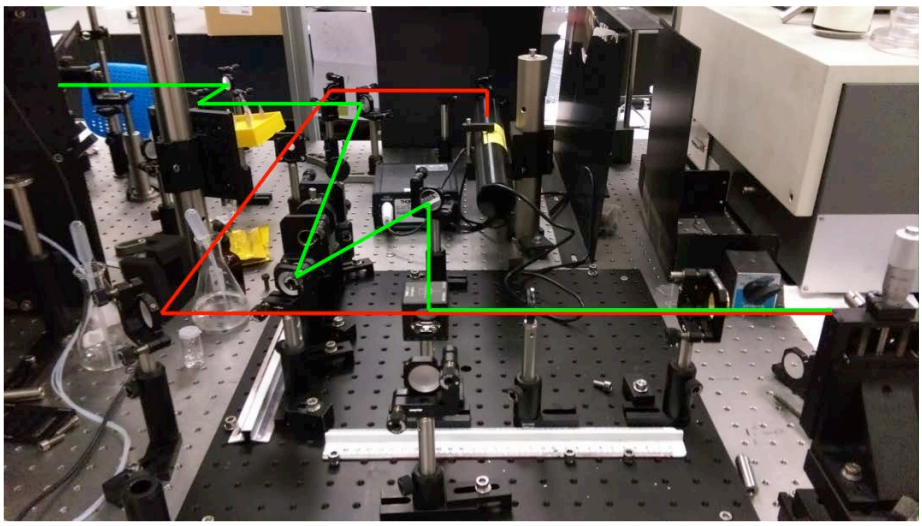

Fig 3.3.2-4 Schematics of optical system (a) and real photograph (b) of measurement setup with external green beam used for heating of LC.

3.3.3 Numerical calculations

In order to explore the phase transition, and especially inhomogeneous phase transition as excited by external (green) laser beam, we performed series of FDTD calculations assuming the incident beam waist 2 μm, wavelength 633 nm, and the refractive indices correspondingly. The calculated near field and far field distributions are presented above in Fig 3.1.1-3 and Fig 3.2.2-1. To give theoretical interpretation of the results obtained by external heating and optical tuning shown in Fig 3.3.2-1 and Fig 3.3.2-3 respectively, we assume that where higher temperature and intensity appears is where the LC in isotropic state locates, i.e. in the axial area of the beam, while for where far away from the axis, the LC is in nematic state. The simplest approach is to assume that isotropic state is in a channel around optical axis, with the thickness depending on the beam intensity. More detailed approach is to assume the refractive index distribution with several geometric designs: cylindrical channel or ellipsoid profiles. We further simplify such graded indices distribution into: rectangle (for 3D cylindrical channel profile) and ellipse (for 3D ellipsoid profile) shapes in our 2D calculations.

In order to mimic the intensity profile of the exciting green beam, we vary the diameter of cylindrical channel profile (which corresponds to the width of rectangle in 2D calculations) filled by the isotropic refractive index while the rest background areas remain in the nematic state. In the ellipsoid case, we describe the refractive indices by the intensity decay distances of Gaussian beam (which corresponds to the major axes of 1-fold and 2-fold ellipse) along *z*-axis to approach the experimental results.

<u>The calculation for rectangle design</u>

The first assumption of intense pump beam profile is its cylinder shape propagating without broadening all the way through the sample. As considered in 2D simulation, the design background index profile is in rectangle shape. The central rectangle area is filled by the isotropic refractive index n_i = 1.588. In Fig 3.3.3-1 the typical near fields obtained from numerical calculation are presented for the dimension of the central rectangle's width 10 μm and height 68 μm. The far fields are presented in Fig 3.3.3-2 for various widths w_x = 5, 8, 9, 10, 12, 15, 18, 20, 25, 30, 35, 40 μm and the same height h_z = 68 μm of the rectangle areas, which corresponds to different intensities of the incident beam.

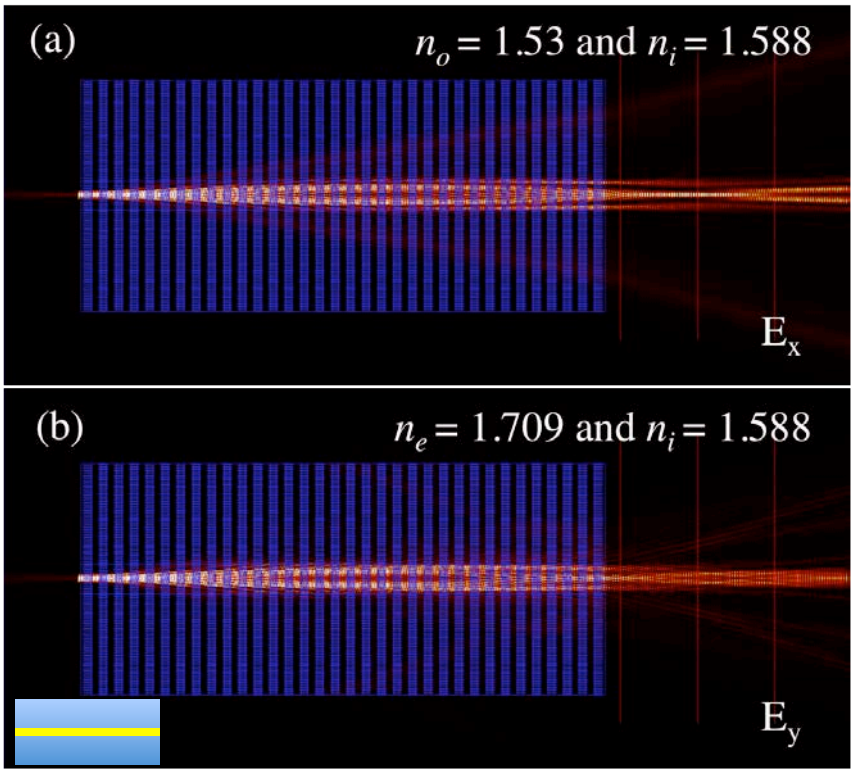

Fig 3.3.3-1 The FDTD calculations of near field distribution for TE (o-wave) (a), and TM (e-wave) (b) polarizations at 633 nm. The incident beam waist is 2 μm and its waist is placed 0.3 μm in front of woodpile PhC. The refractive index of polymer woodpile remains n_p = 1.54. The indices for LCs background are set in 2-fold rectangle design shown as inset on bottom left corner.

In Fig 3.3.3-2 we found for the Y-polarized incident beam, the angular transmission patterns are very sensitive to the average effective index of the sample medium. For the width of the rectangular area w_x = 5 μm, the filtering lines become vague as observed in Fig 3.3.2-3 (c). The ellipse beam profiles observed near the transition point in the optical tuning measurement appear when the central rectangle width increases to 9 - 10 μm observed before for LC-PhC. When the rectangle width increases to 40 μm, similar square symmetric pattern appears as in isotropic phase.

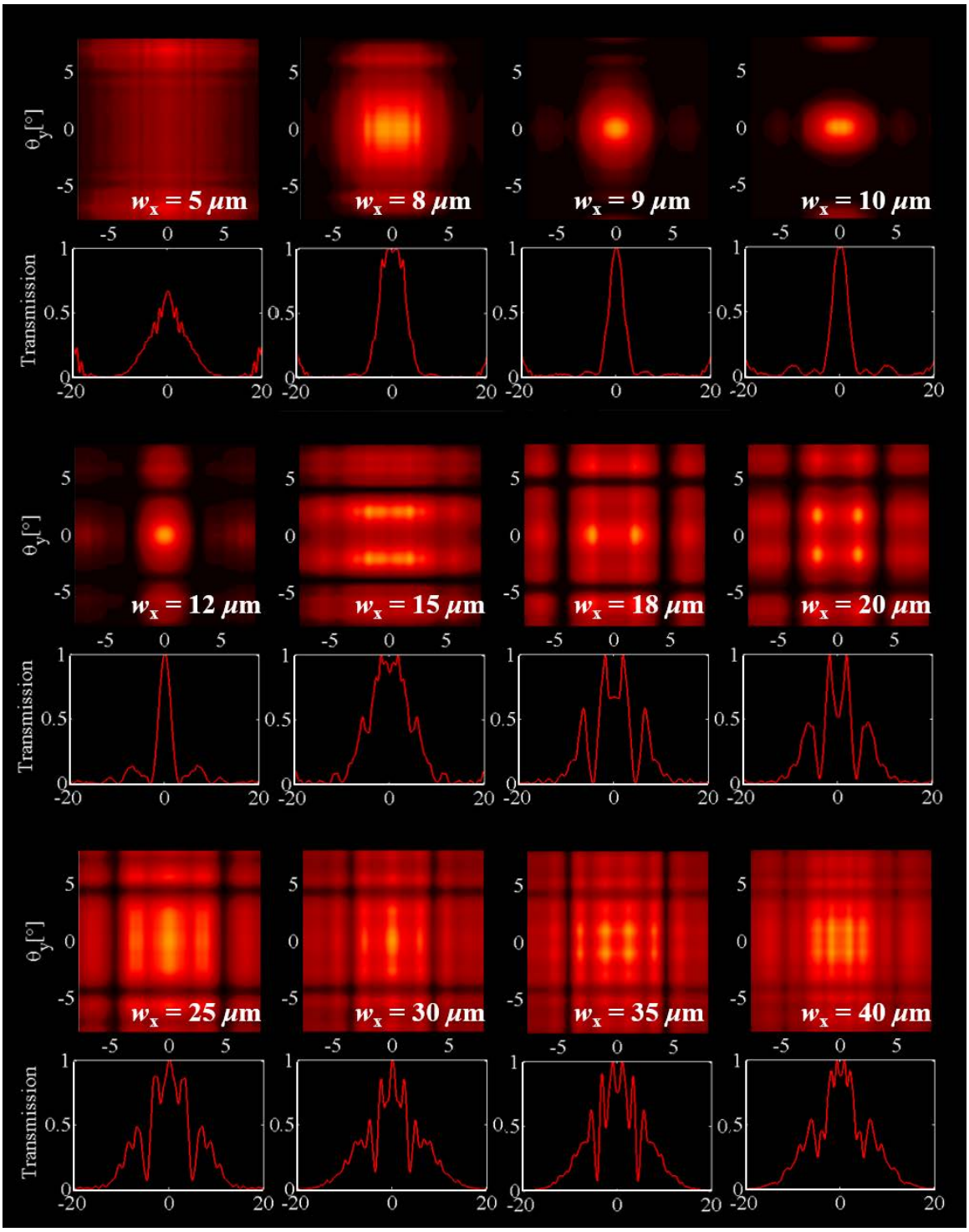

Fig 3.3.3-2 2D far field distributions of the central part beam as obtained by FDTD calculations (1st, 3rd, 5th rows) and 1D intensity distributions along the *x* direction (integrated along the *y* direction) obtained from numerics (2nd, 4th, 6th rows) for the 2-fold rectangle indices design by varying the rectangle widths from 5 μm to 40 μm.

The calculation for ellipse design

The second more realistic design follows from the assumption of the tightly focused intense beam profile in Gaussian shape. In such case the Gaussian beam switches the LC not along the cylindrical tube, but rather in ellipsoid area around the focal point of the focused beam. The ellipsoid is strongly elongated along propagation direction. As considered into 2D simulation, the design is in ellipse shape. The dimension of the central ellipse is: the minor axis 1.5 μm and the major axis 15 μm (at the intensity of injection beam equal to half maximum without presence of woodpile) with the isotropic refractive index n_i = 1.588. The results from numerical calculation are presented in Fig 3.3.3-3 and Fig 3.3.3-4.

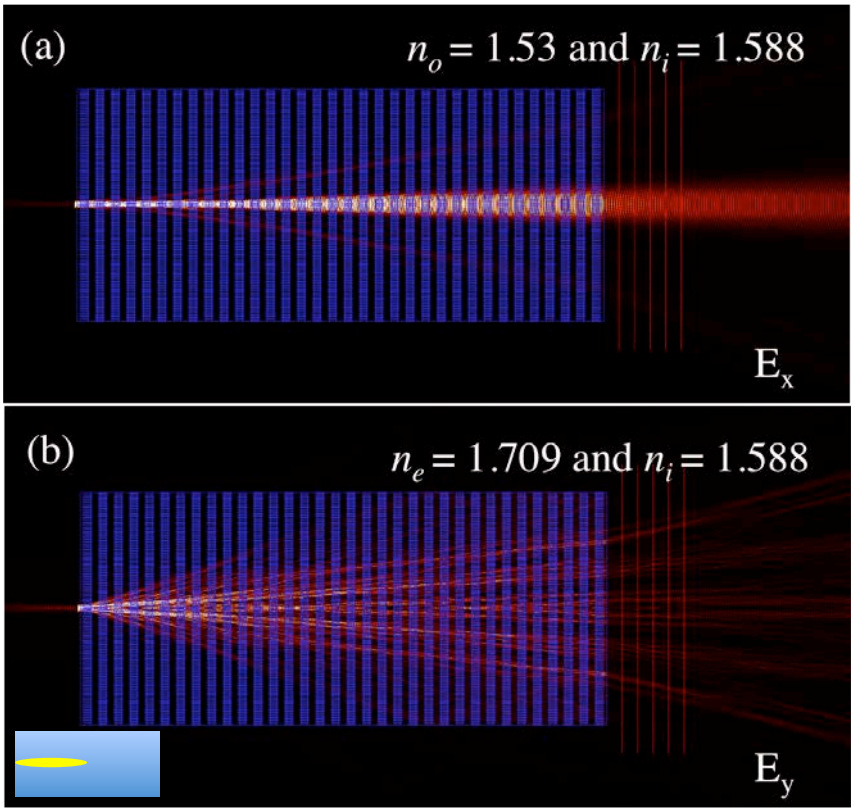

Fig 3.3.3-3 The FDTD calculations of near field distribution for TE (o-wave) (a), and TM (e-wave) (b) polarizations at 633 nm. The incident probe beam waist is set 2 μm and placed 0.3 μm in front of woodpile PhC. The indices of 1-fold ellipse and 1-fold rectangle design are shown as inset on bottom left corner.

In Fig 3.3.3-4 (b) we found the sharpness of the vertical dark lines decreases and the horizontal ones starts to split in good correspondence with Fig 3.2.2-1 (f). The square symmetric pattern for the isotropic state is shown as reference in Fig 3.3.3-4 (d).

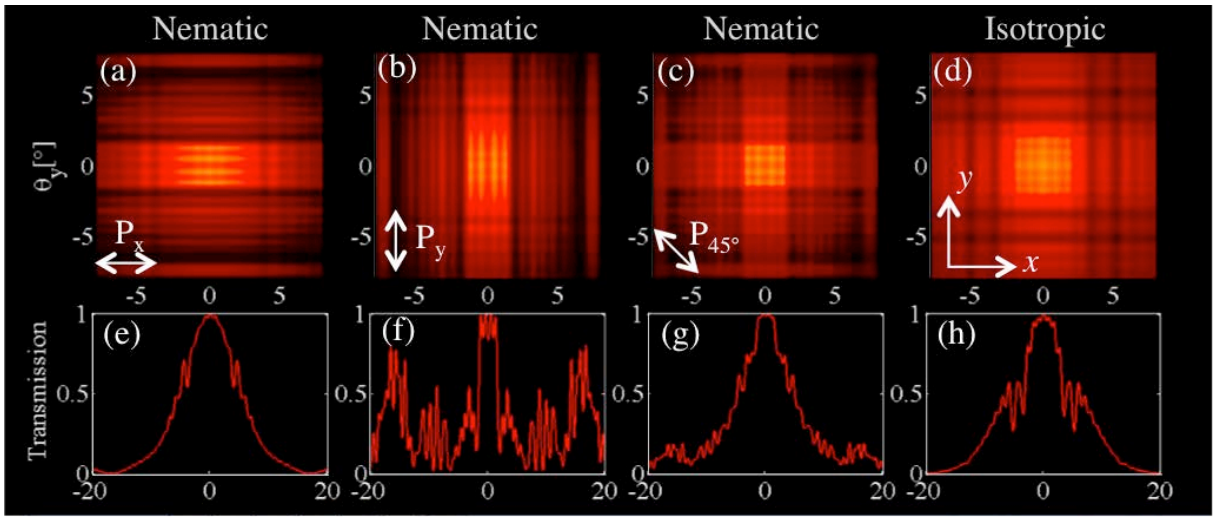

Fig 3.3.3-4 The far field transmission patterns for the 1-fold ellipse and 1-fold rectangle indices design, the top row shows 2D far field distributions of the central part beam as obtained by FDTD calculations (a,b,c,d) and the bottom row (e,f,g,h) demonstrates the 1D intensity distributions along the *x* direction (integrated along the *y* direction) obtained from numerics.

<u>The calculation for advanced ellipse design</u>

The third design assumes that the intense Gaussian beam profile is in 2-fold ellipse shape for 2D simulation. The dimension of the central ellipse is with the minor axis 1.5 μm and the major axis 15 μm (where the intensity of pump beam drops to half maximum without presence of woodpile) with the isotropic refractive index n_i = 1.588. The dimension of the 2nd layer ellipse is with the minor axis 2.5 μm and the major axis 35 μm (where the intensity of pump beam drops to a quarter maximum without presence of woodpile) with the medium index $n_{med.}$ = 1.649 or 1.559 by taking average between either n_e and n_i or n_o and n_i for e-wave and o-wave polarizations respectively. The results from numerical calculation are presented in Fig 3.3.3-5 and Fig 3.3.3-6.

In Fig 3.3.3-6 (a) the filtering angles become broader for the X-polarized incident beam. In Fig 3.3.3-6 (b) the sharpness of both the vertical and horizontal dark lines drop. Meanwhile the dark lines start to split (as those observed in the isotropic state). These tendencies indicate the transition stage where LCs are partially excited before entering the isotropic phase. The square symmetric pattern for the isotropic state is shown as reference in Fig 3.3.3-6 (d).

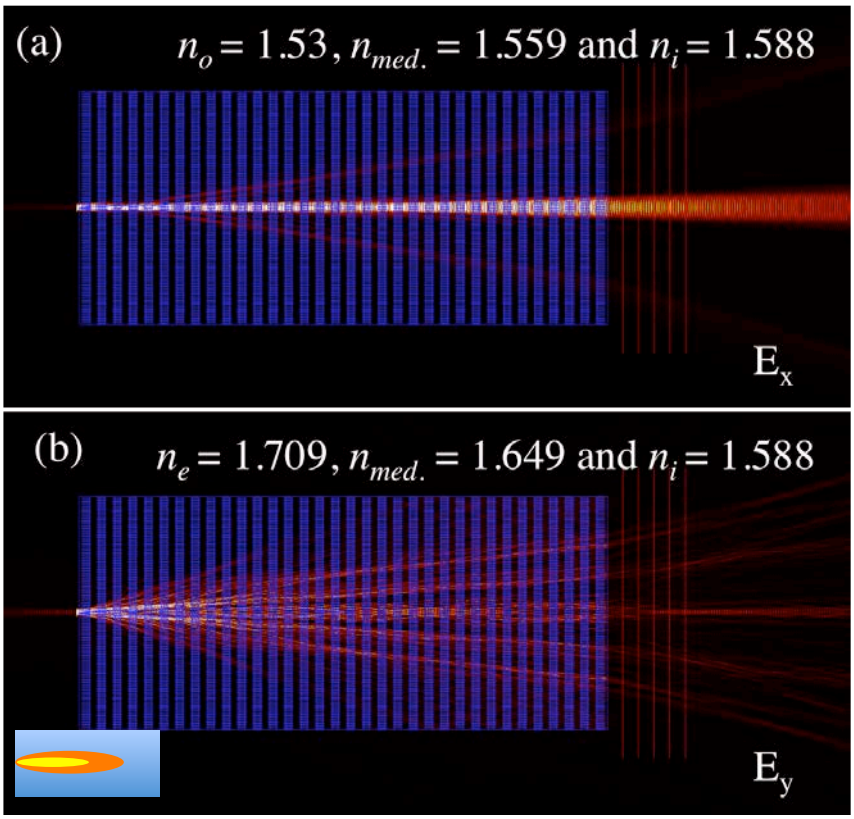

Fig 3.3.3-5 The FDTD calculations of near field distribution under TE (o-wave) (a), and TM (e-wave) (b) polarizations at 633 nm. The incident probe beam waist is set 2 μm and placed 0.3 μm in front of woodpile PhC. The indices of 2-fold ellipse and 1-fold rectangle design are shown as inset on bottom left corner.

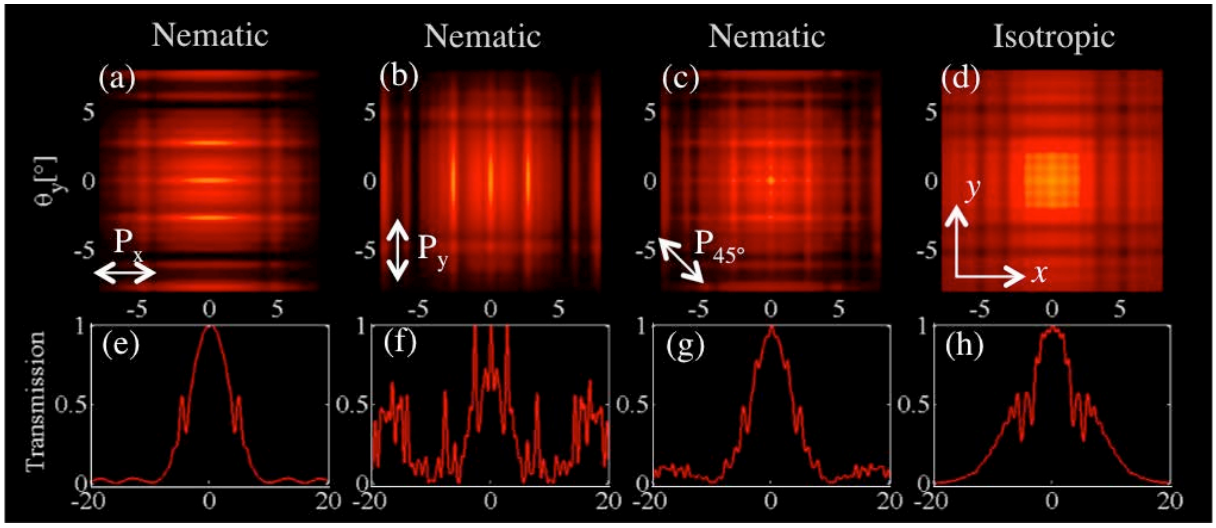

Fig 3.3.3-6 For the 2-fold ellipse and 1-fold rectangle indices design, the top row shows 2D far field distributions of the central part beam as obtained by FDTD calculations (a,b,c,d) and the bottom row (e,f,g,h) demonstrates the 1D intensity distributions along the *x* direction (integrated along the *y* direction) obtained from numerics.

3.4 Nonlinear effect controlled by single beam (self-collimation)

3.4.1 Review of single beam nonlinear effect

The results presented in 3.3.2 indicate weakly nonlinear propagation of green laser beam. In order to discuss purely nonlinearity achieved by self-interaction of light, we used single wavelength at 532 nm in this section as both pump and probe beam. Before the discussion upon our experimental observations, we introduce the concept of spatial solitons.

The light confinement in nonlinear medium could be described through the formation of optical waveguides [17]. Light propagation in homogenous medium tends to diffract and spread. In a nonlinear medium, the refractive index distribution in transverse direction follows the intensity of propagation beam. In self-focusing case it creates the high-index region at center but the low-index region at margin. This graded index gives self-confinement of light in analogy to optical fiber waveguide. Another interpretation is used comparing with lenses: the curved wavefront due to diffraction is similar to the beam spreading of light propagation after a concave lens. While the intensity dependence index resulted from reorientations of LC nonlinear medium generates the curved wavefront similar to the beam focusing after a convex lens. When these two effects compensate each other, the shape of phase front becomes plane and therefore spatial soliton is formed. Schematic illustration is presented in Fig 3.4.1.

Several related work on self-waveguiding and confinement are reported through various approaches. By coating homeotropic alignment layer in advance on glass substrate, unstable self-focusing is observed for TE wave while stable self-trapped beam is formed for TM wave in LC layer when incident beam power increases above threshold [18]. By doping either low or high dye concentration into the LC medium, the focusing effect and self-waveguiding are observed respectively. The high pump power of incident beam helps stabilize the reorientation of LC molecules and consequently a waveguide is formed due to the high refractive index in central region [19]. By adding bias electric field, the reorientational

nonlinearity also appears upon LCs and gives well confinement channel for both self-waveguiding and also co-launched probe beam [20] [21].

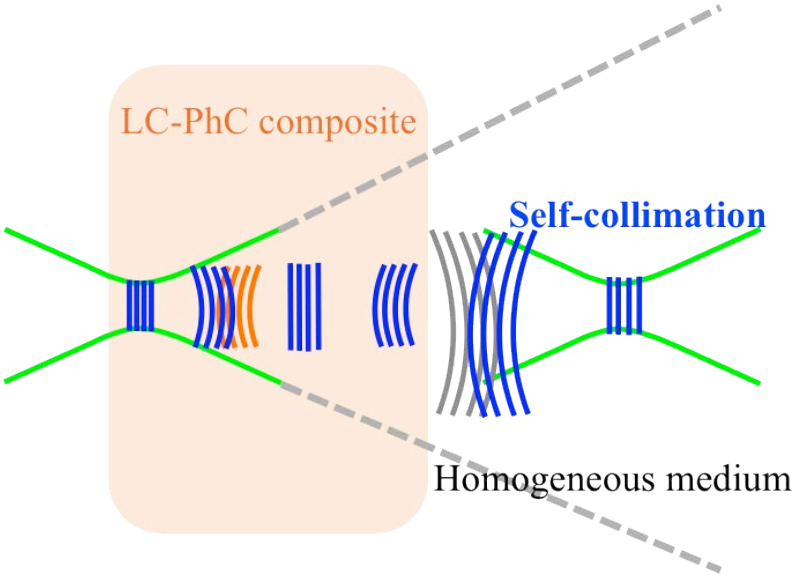

Fig 3.4.1 Schematic illustration of phase modulation when light propagates through LC-PhC composite, the wave front evolves from concave, flat, into convex shape. The orange curves refer to the opposite phase compensation given by the composite while the gray curves refer to the beam spreading occurred in homogeneous medium.

3.4.2 Experiment results

<u>The dark circular fringe appearing at transition</u>

The dark circular fringe observed in transmission results from the phase modulation of the dye doped LC-PhC composite. The refractive index distribution of the composite could be described as a rectangular function (high intensity of n_i and low intensity of n_e and n_o). When light propagates in the composite medium, the original concave phase front is gradually modulated into plane phase front according to the refractive index distribution. By making the Fourier transform of such plane phase front in near field, we can obtain *sinc* function in k-space, i.e. the circular dark fringe as intensity distribution in far field.

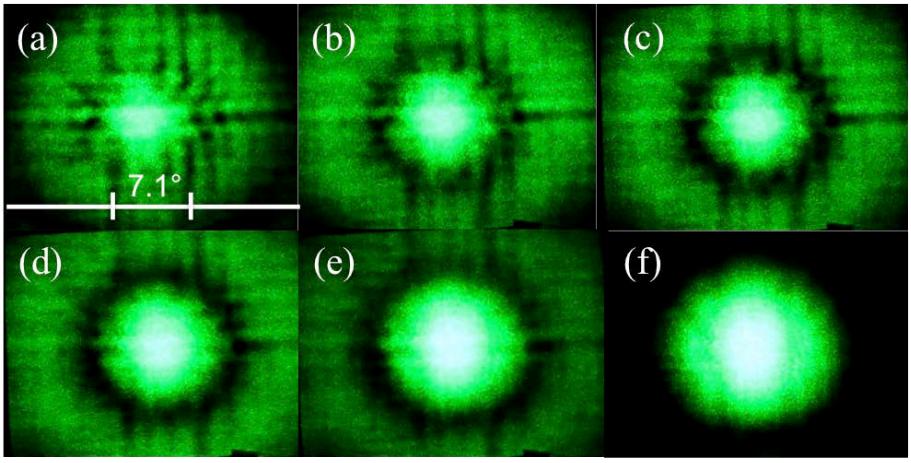

Fig 3.4.2-1 Snapshots taken from the video record filmed in correspondence to the gradual decrease of intensity. The dark circular fringe appears in far field transmission pattern at transition point and expands outward when decreasing the intensity of incident beam to switch from the isotropic (a) to the nematic state (f).

To explore the nonlinear effect (such as self-confinement or self-collimation) of the dye doped LC-PhC composite media, here we recorded the near field distributions with CCD camera in details. The optical system is mainly composed of an infinity-corrected apochromatic, long working distance 20x Mitutoyo objective (for focusing), the sample crystal and an infinity-corrected, apochromatic, long working distance Mitutoyo 50x objective (for imaging). The depth of focus of 50x objective is 0.9 μm (longitudinal resolution) with a resolving power of 0.5 μm (transverse resolution). To obtain the image at the working distance of the 50x objective at finite distance we used a tube lens of focal length 200 mm and the resulting intermediate image was projected into the CCD sensor (Spiricon SP620-U) with 4.4 pixel size using a 4x objective to get a magnification of around 100 on the CCD. Both the positions of the focusing and the imaging objectives are controlled by closed-loop step motors PI Micos PLS-85 with 0.5 μm precision [22].

To determine the interfaces precisely, we used a target bar (of a few micron tall) written during fabrication. By clearly imaging the target bar on CCD, the entrance of crystal was determined. By moving corresponding distance (of crystal height) away from the target bar, confirmed by clear image of grating on top surface on CCD, the exit of crystal was determined. The incident beam is tightly focused at the entrance of crystal, i.e. the interface between glass substrate and crystal. To retrieve the modulated beam profile inside the crystal, the focusing objective is moving 2 μm per step along z direction that makes the focal point enter the crystal while the focal plane of imaging objective is fixed at the exit of crystal. The beam profile inside crystal cannot be obtained by moving the focal plane of the imaging

objective into the crystal due to strong scattering inside composite medium. The original beam propagation profile in absence of LC-PhC composite is also measured as reference.

The Gaussian beam width equation [23] is introduced for the fitting curves along z axis,

$$w(z) = w_0 \sqrt{1 + \left(\frac{z - z_0}{z_\mathrm{R}}\right)^2} \tag{3.8}$$

where w_0 is the beam waist, z_0 indicates the location of the focal point inside crystal and z_R is the Rayleigh range defined by,

$$z_\mathrm{R} = \frac{\pi w_0^2}{\lambda} \tag{3.9}$$

The Rayleigh range z_R also corresponds to the propagation distance where the beam width $\sqrt{2}w_0$ appears.

<u>Self-collimation of dye-doped LC-PhC composite observed “inside” crystal</u>

The presence of a small amount of dye in LC-PhC composite decreases the laser threshold power needed to achieve phase transition point. Here we used the same strategy as described previously (fix the focal plane of the imaging objective at the exit of crystal but move the focusing objective along z- axis toward the crystal) to retrieve the modulated beam profiles inside crystal.

The measured dye-doped LC-PhC composite are with height h_z = 38 μm. The measured beam profiles along z- axis are demonstrated in Fig 3.4.2-2 with respect to the moving distance z of the focusing objective. The collimated region is observed when the focusing objective moves z = z_0 ± 6 μm near the location of the focal points. In nematic state, the focal point is located at z_0 = 22 μm. At transition point, the focal point is located at z_0 = 26 μm. The original beam is recorded from the entrance of crystal at z_0 = 0 μm as reference.

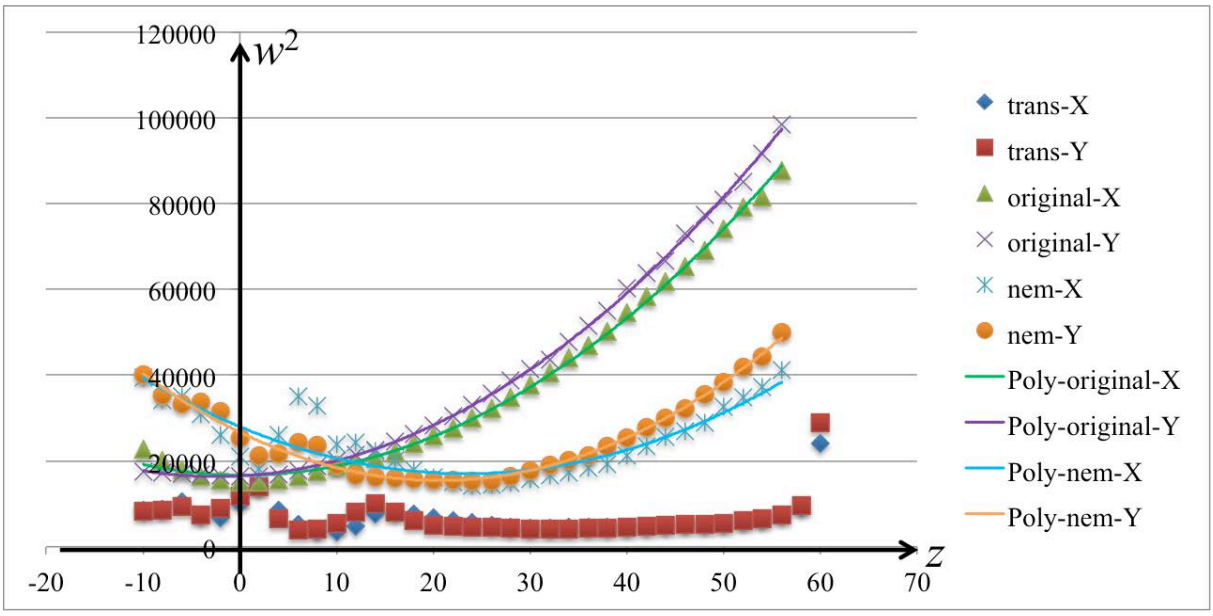

Fig 3.4.2-2 The quadratic beam widths (in *x* or in *y* direction) recorded when the imaging objective moves along *z*- axis with (nematic: light blue and orange dots; transition: dark blue and red dots) and without (green and purple dots) presence of dye-doped LC-PhC composite. The corresponding parabolas are fitting curves obtained from Gaussian beam width equation. The crystal height h_z = 38 μm.

From Fig 3.4.2-2 we find that in nematic state the beam width of focal point (w_0 = 127 arb. unit) remains similar to the original beam (w_0 = 128 arb. unit). The obvious shrinkage of focal point (w_0 = 66 arb. unit) is observed when laser intensity increases and reaches the transition point. The beam confinement remains quite a long distance (around 15 μm behind the exit) for LC at transition point. To give more clear picture, the transverse cross sections (in *xy*-plane) of the collimated beam are also presented in the range of $z_0 \pm 6$ μm, with 2 μm per step in Fig 3.4.2-3.

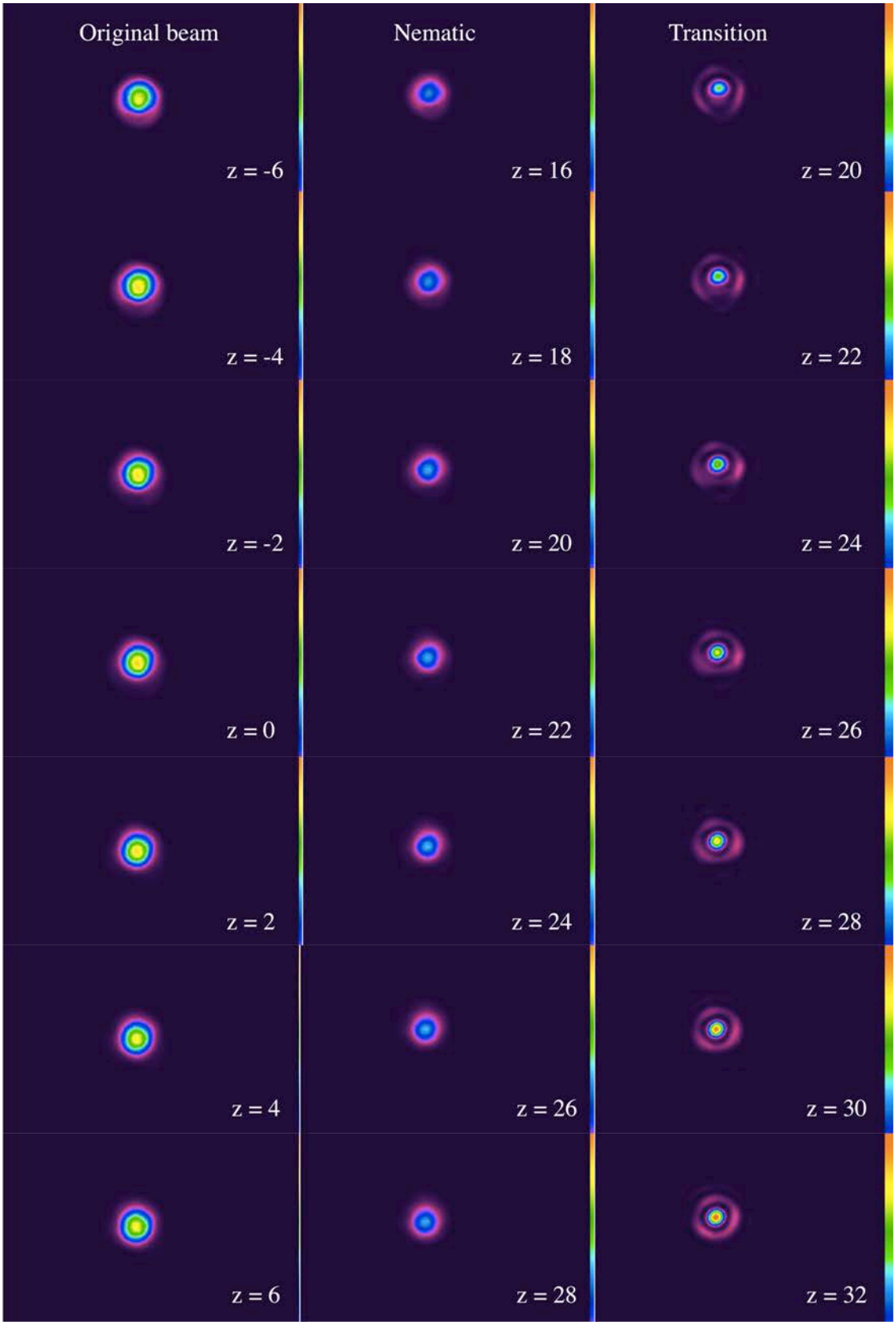

Fig 3.4.2-3 The collimated beam observed at the exit of dye-doped LC-PhC composite when the focusing objective moves ± 6 μm near the focal points of the original beam (left column), LC in nematic phase (middle column) and LC at transition (right column).

3.4.3 Numerical calculations

To give theoretical approach to our experimental results, here we performed the same FDTD calculations as before but modified the beam waist into 2.5 μm, wavelength 532 nm, and the refractive indices correspondingly. The calculated near field and far field distributions are presented in Fig 3.4.3-1 and Fig 3.4.3-2. The former is obtained by commercial FDTD software (CrystalWave, Photon Design). The later is obtained by making Fourier transform of the FDTD results in Matlab.

Although the numerics describe the general features of experimental observations, some quantitative differences are present. In Fig 3.4.3-2 (b) and Fig 3.2.2-3 (e) they show different rectangle symmetries, the elongated directions for the filtering patterns are in *y*- and *x*- axis respectively under the Y-polarized beam. As for the results obtained in the isotropic state, they appear the same square symmetric and the range of filtering angles becomes smaller when reducing wavelengths, See Fig 3.4.3-2 (d) and Fig 3.2.2-3 (f).

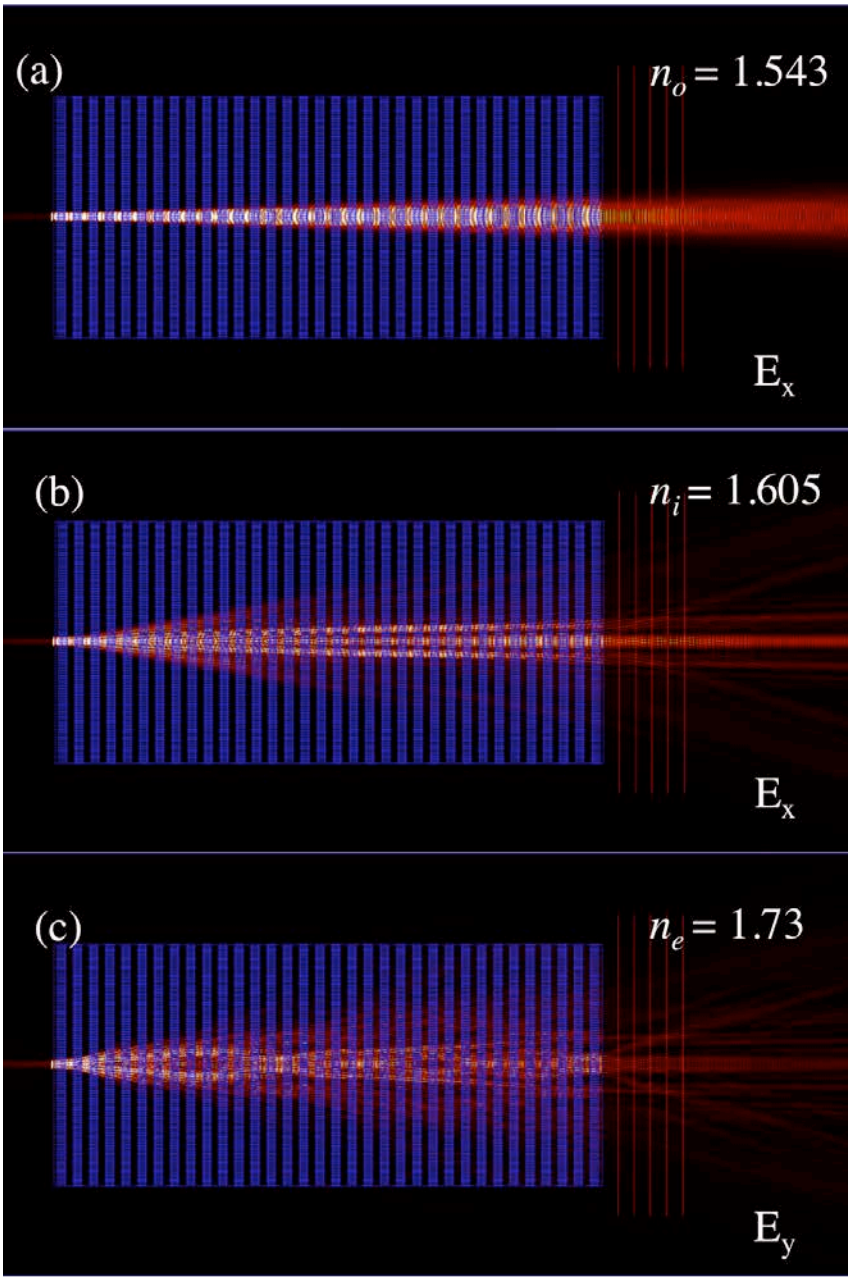

Fig 3.4.3-1 The FDTD calculations of near field distribution for TE (o-wave) (a-b), and TM (e-wave) (c) polarizations at 532 nm. The incident beam waist is set 2.5 μm and placed 0.3 μm in front of woodpile PhC. The refractive index of polymer woodpile remains n_p = 1.54 while the indices for LCs background vary from n_o = 1.543, n_i = 1.605 to n_e = 1.73 under the corresponding polarizations.

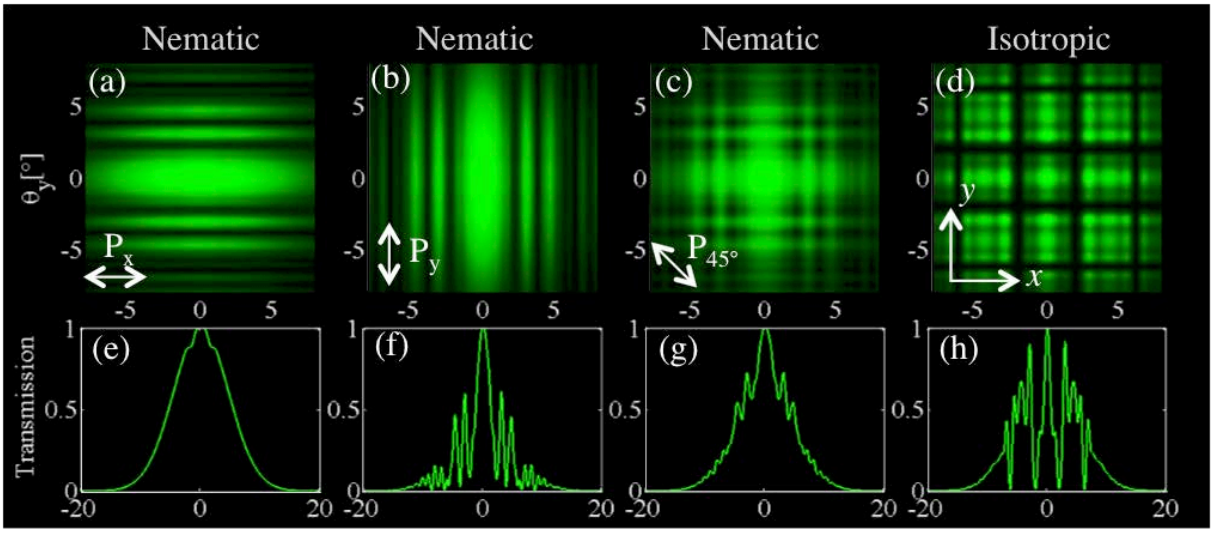

Fig 3.4.3-2 The top row shows 2D far field distributions of the central part beam as obtained by FDTD calculations (a,b,c,d). The bottom row (e,f,g,h) demonstrates the 1D intensity distributions along the *x* direction (integrated along the *y* direction) obtained from FDTD numerics.

Concerning the high power beam of green, the discrepancy is caused by the nonlinear reorientation of LCs located in high intensity regions where the refractive index needs to be corrected correspondingly. In order to approach the experimental results by numerical calculations, we modified into graded indices with various geometric designs.

<u>The calculation for rectangle design</u>

The first assumption of intense beam profile is in cylinder shape propagating all the way through the sample. As converted into 2D simulation, the design is in rectangle shape. The dimension of the central rectangle we used here is width 2.5 μm and height 68 μm with the isotropic refractive index n_i = 1.605. The results from numerical calculation are presented in Fig 3.4.3-3 and Fig 3.4.3-4.

In Fig 3.4.3-4 (b) we found the elongated direction for the filtering pattern now is in *x*- axis obtained from the Y-polarized incident beam yet the sharpness of the vertical dark lines stays low. The square symmetric pattern for the isotropic state is again shown as reference in Fig 3.4.3-4 (d).

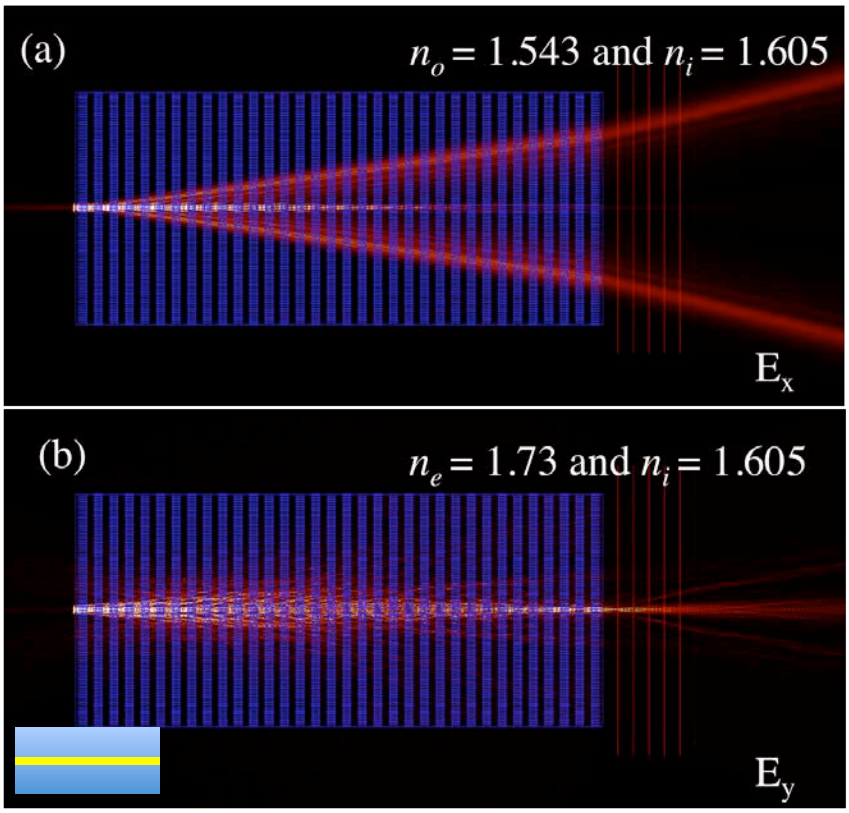

Fig 3.4.3-3 The FDTD calculations of near field distribution under TE (o-wave) (a), and TM (e-wave) (b) polarizations at 532 nm. The incident beam waist is set 2.5 μm and placed 0.3 μm in front of woodpile PhC. The refractive index of polymer woodpile remains n_p = 1.54. The indices for LCs background are set in 2-fold rectangle design shown as inset on bottom left corner.

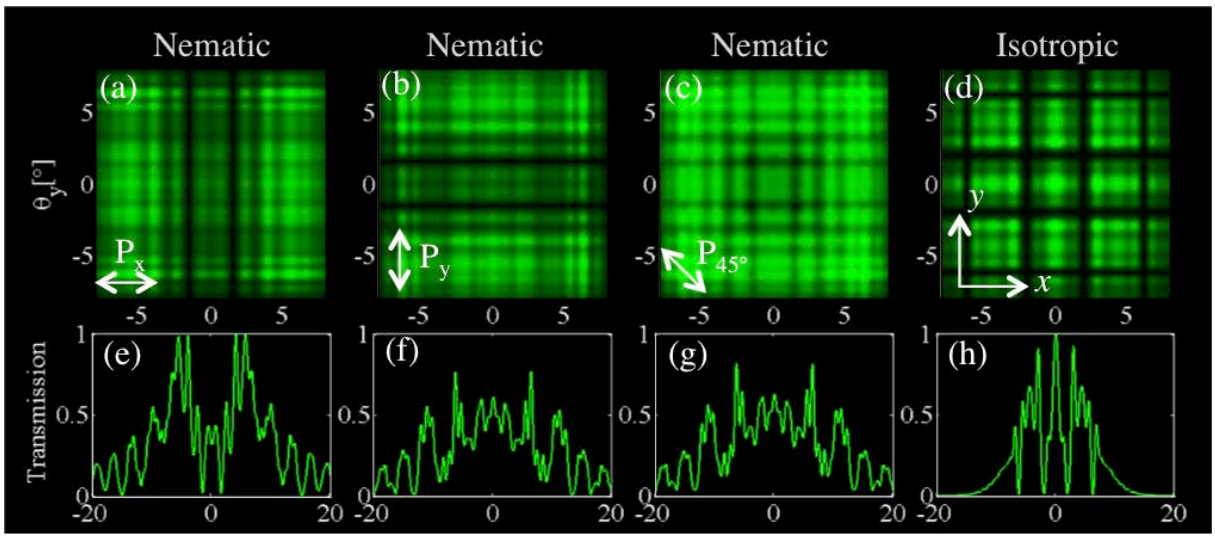

Fig 3.4.3-4 For the 2-fold rectangle indices design, the top row shows 2D far field distributions of the central part beam as obtained by FDTD calculations (a,b,c,d) and the bottom row (e,f,g,h) demonstrates the 1D intensity distributions along the *x* direction (integrated along the *y* direction) obtained from FDTD numerics.

The calculation for ellipse design

The second design is from the assumption of intense beam profile in Gaussian shape that does not penetrate through the sample. As converted into 2D simulation, the design is in ellipse shape. The dimension of the central ellipse is with the minor axis 1.5 μm and the major axis 15 μm (where the intensity drops to half maximum without presence of woodpile) with the isotropic refractive index n_i = 1.605. The results from numerical calculation are presented in Fig 3.4.3-5 and Fig 3.4.3-6.

In Fig 3.4.3-6 (b) we found not only the elongated direction for the filtering pattern is in *x*-axis obtained from the Y-polarized incident beam but also the sharpness of the vertical dark lines becomes much clear. The square symmetric pattern for the isotropic state is shown as reference in Fig 3.4.3-6 (d).

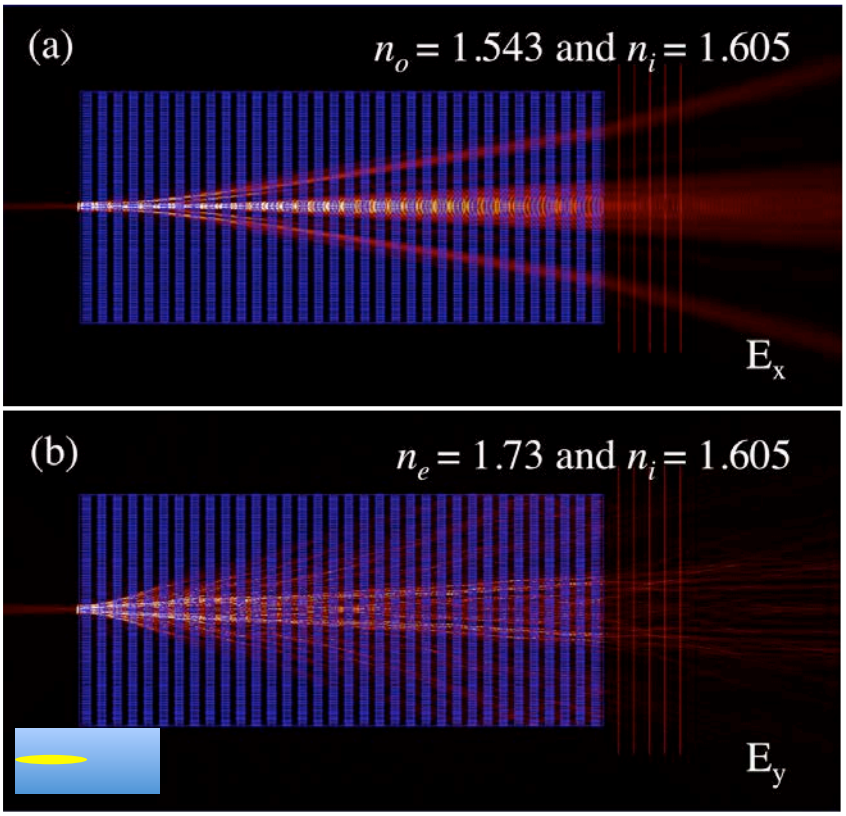

Fig 3.4.3-5 The FDTD calculations of near field distribution under TE (o-wave) (a), and TM (e-wave) (b) polarizations at 532 nm. The incident beam waist is set 2.5 μm and placed 0.3 μm in front of woodpile. The indices of 1-fold ellipse and 1-fold rectangle design are shown as inset on bottom left corner.

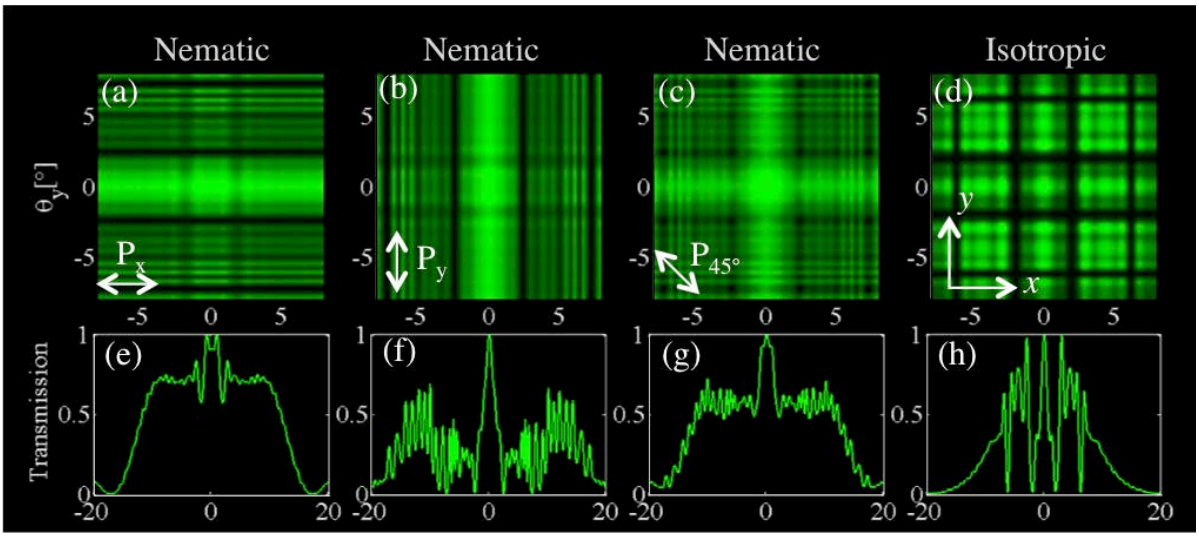

Fig 3.4.3-6 For the 1-fold ellipse and 1-fold rectangle indices design, the top row shows 2D far field distributions of the central part beam as obtained by FDTD calculations (a,b,c,d) and the bottom row (e,f,g,h) demonstrates the 1D intensity distributions along the *x* direction (integrated along the *y* direction) obtained from numerics.

<u>The calculation for advanced ellipse design</u>

The third design is also from the assumption of intense beam profile in Gaussian shape but in two graded levels. In 2D simulation, the design is in two-layer ellipse shape. The dimension of the central ellipse is with the minor axis 1.5 μm and the major axis 15 μm (where the intensity drops to half maximum without presence of woodpile) with the isotropic refractive index n_i = 1.605. The dimension for the 2nd layer ellipse is with the minor axis 2.5 μm and the major axis 35 μm (where the intensity drops to a quarter maximum without presence of woodpile) with the medium index $n_{med.}$ = 1.668 or 1.574 by taking average between either n_e and n_i or n_o and n_i for e-wave or o-wave polarizations respectively. The results from numerical calculation are presented in Fig 3.4.3-7 and Fig 3.4.3-8.

In Fig 3.4.3-8 (b) the elongated direction for the filtering pattern remains in *x*- axis for the Y-polarized beam and the filtering angles of the clear vertical dark lines becomes wider. The square symmetric pattern for the isotropic state is shown as reference in Fig 3.4.3-8 (d).

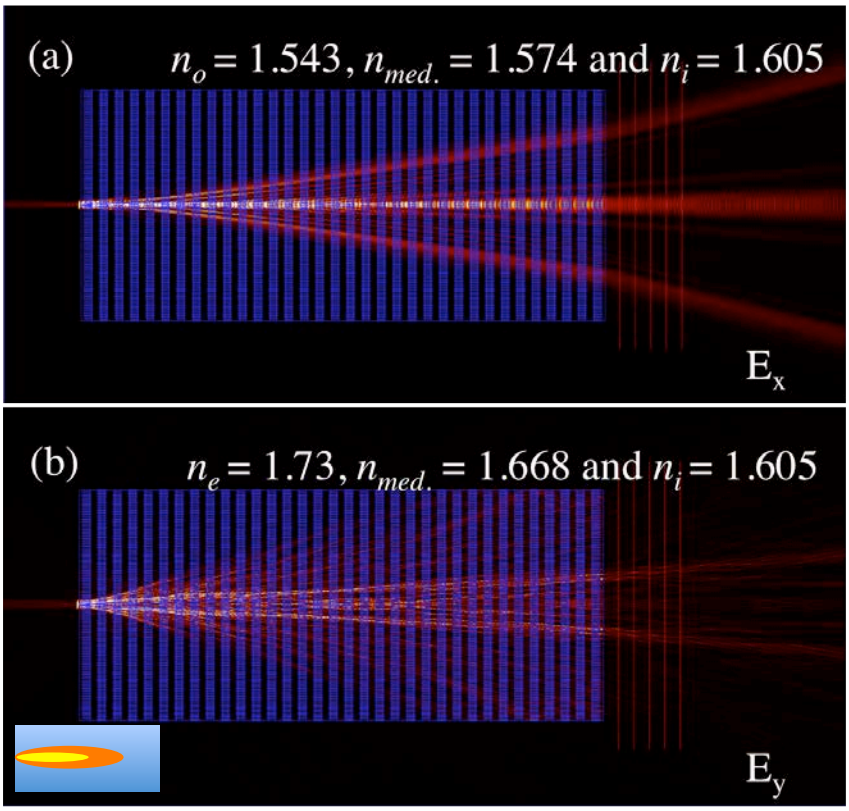

Fig 3.4.3-7 The FDTD calculations of near field distribution under TE (o-wave) (a), and TM (e-wave) (b) polarizations at 532 nm. The incident beam waist is set 2.5 μm and placed 0.3 μm in front of woodpile. The indices of 2-fold ellipse and 1-fold rectangle design are shown as inset on bottom left corner.

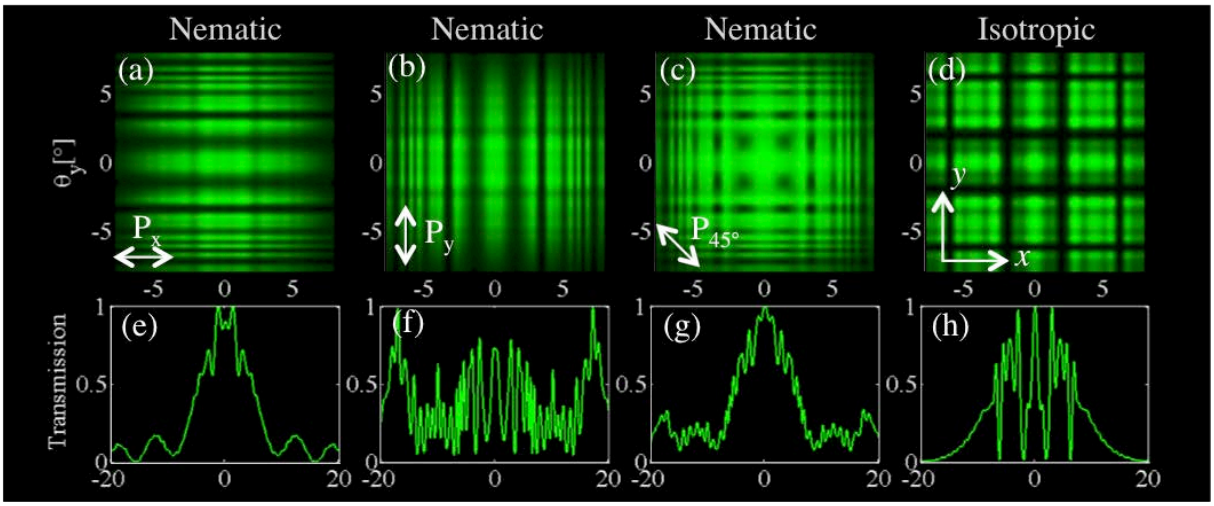

Fig 3.4.3-8 For the 2-fold ellipse and 1-fold rectangle indices design, the top row shows 2D far field distributions of the central part beam as obtained by FDTD calculations (a,b,c,d) and the bottom row (e,f,g,h) demonstrates the 1D intensity distributions along the *x* direction (integrated along the *y* direction) obtained from numerics.

3.5 Summary

In this chapter we mainly demonstrated our work upon the investigation of LC-PhC composite from fabrication, simulation and also measurement point of views. We introduced the lithography technique used in our fabrication; following several numerical calculations we conducted with different designs of the graded indices, and demonstrated the experimental results to compare.

The wavelengths we explored are mainly at 633nm and 532nm. The observations upon filtering patterns in far field at 633nm stay in linear regime by applying external heating and show good correspondence to numerical calculations. Those obtained by the green pump beam (optical tuning) show weak nonlinearity due to the intensity dependence of LC refractive index. Last but not least, the observations at 532 nm appear the nonlinear effect such as self-confinement and self-collimation.

References

[1] M. Peccianti, C. Conti, G. Assanto, A. De Luca, and C. Umeton, “Routing of anisotropic spatial solitons and modulational instability in liquid crystals,” *Nature*, vol. 432, no. 7018, pp. 733–737, 2004.

[2] L. Scolari, T. T. Alkeskjold, and A. Bjarklev, “Tunable Gaussian filter based on tapered liquid crystal photonic bandgap fibre,” *Electron. Lett.*, vol. 42, no. 22, pp. 1270–1271, 2006.

[3] M. Wahle and H.-S. Kitzerow, “Liquid crystal assisted optical fibres,” *Opt. Express*, vol. 22, no. 1, pp. 262–273, 2014.

[4] R. L. Sutherland, V. P. Tondiglia, L. V. Natarajan, T. J. Bunning, and W. W. Adams, “Electrically switchable volume gratings in polymer-dispersed liquid crystals,” *Appl. Phys. Lett.*, vol. 64, no. 9, pp. 1074–1076, 1994.

[5] A. K. Bhowmik, Z. Li, and P. J. Bos, *Mobile displays: technology and applications*, vol. 15. John Wiley & Sons, 2008.

[6] C.-H. Ho, Y.-C. Cheng, L. Maigyte, H. Zeng, J. Trull, C. Cojocaru, D. S. Wiersma, and K. Staliunas, “Controllable light diffraction in woodpile photonic crystals filled with liquid crystal,” *Appl. Phys. Lett.*, vol. 106, no. 2, p. 021113, 2015.

[7] C.-H. Ho, J. Trull, S. Nocentini, A. K. Tiwari, H. Zeng, Y. C. Cheng, D. Wiersma, and K. Staliunas, “Nonlinear beam propagation in photonic crystals filled with liquid crystal,” *In*

preparation, 2015.

[8] L. Maigyte, T. Gertus, M. Peckus, J. Trull, C. Cojocaru, V. Sirutkaitis, and K. Staliunas, "Signatures of light-beam spatial filtering in a three-dimensional photonic crystal," *Phys. Rev. A*, vol. 82, no. 4, p. 043819, 2010.

[9] L. Maigyte and K. Staliunas, "Spatial filtering with photonic crystals," *Appl. Phys. Rev.*, vol. 2, no. 1, p. 011102, 2015.

[10] J. Li, S. Gauza, and S.-T. Wu, "Temperature effect on liquid crystal refractive indices," *J. Appl. Phys.*, vol. 96, no. 1, pp. 19–24, 2004.

[11] L. Maigyte, "Shaping of light beams with photonic crystals: spatial filtering, beam collimation and focusing, PhD" *Universitat Politècnica de Catalunya*, 2014.

[12] A. Y.-G. Fuh, M.-S. Tsai, L.-J. Huang, and T.-C. Liu, "Optically switchable gratings based on polymer-dispersed liquid crystal films doped with a guest–host dye," *Appl. Phys. Lett.*, vol. 74, no. 18, pp. 2572–2574, 1999.

[13] T. Alkeskjold, J. Lægsgaard, A. Bjarklev, D. Hermann, A. Anawati, J. Broeng, J. Li, and S.-T. Wu, "All-optical modulation in dye-doped nematic liquid crystal photonic bandgap fibers," *Opt. Express*, vol. 12, no. 24, pp. 5857–5871, 2004.

[14] K.-Y. Yu, S.-H. Chang, C.-R. Lee, T.-Y. Hsu, and C.-T. Kuo, "Thermally tunable liquid crystal distributed feedback laser based on a polymer grating with nanogrooves fabricated by nanoimprint lithography," *Opt. Mater. Express*, vol. 4, no. 2, pp. 234–240, 2014.

[15] H. Coles and S. Morris, "Liquid-crystal lasers," *Nat. Photonics*, vol. 4, no. 10, pp. 676–685, 2010.

[16] G. New, *Introduction to Nonlinear Optics*. Cambridge University Press, 2011.

[17] Y. S. Kivshar and G. Agrawal, *Optical solitons: from fibers to photonic crystals*. Academic press, 2003.

[18] M. A. Karpierz, M. Sierakowski, M. Świłło, and T. Woliński, "Self focusing in liquid crystalline waveguides," *Mol. Cryst. Liq. Cryst.*, vol. 320, no. 1, pp. 157–163, 1998.

[19] M. Warenghem, J. Henninot, and G. Abbate, "Non linearly induced self waveguiding structure in dye doped nematic liquid crystals confined in capillaries," *Opt. Express*, vol. 2, no. 12, pp. 483–490, 1998.

[20] M. Peccianti, A. De Rossi, G. Assanto, A. De Luca, C. Umeton, and I. C. Khoo, "Electrically assisted self-confinement and waveguiding in planar nematic liquid crystal cells," *Appl. Phys. Lett.*, vol. 77, no. 1, pp. 7–9, 2000.

[21] A. Fratalocchi, G. Assanto, K. A. Brzdąkiewicz, and M. A. Karpierz, "Discrete light propagation and self-trapping in liquid crystals," *Opt. Express*, vol. 13, no. 6, pp. 1808–1815, 2005.

[22] Y. C. Cheng, “Flat Focusing Mirrors, PhD” *Universitat Politècnica de Catalunya*, 2015.
[23] O. Svelto and D. C. Hanna, *Principles of lasers*. Springer, 1976.

Chapter 4 Conclusion

In this thesis, we presented our work upon the LC embedded woodpile PhCs. By using various applied stimulations, we investigated its performance and showed the potential applications.

Photonic Crystals (PhCs) are periodic microstructures modulating light propagation behavior at wavelength scale. Such structure allows the light beam to shape its phase fronts and brings abundant optical effects like negative refraction/ diffraction, lensing, collimation, and photonic bandgaps. In addition to periodicity, frequency bandgap appears on occasion of large refractive index contrast media (air/ polymer) while angular bandgap appears in situation of low contrast media (polymer/ liquid).

Due to the high dielectric anisotropy, fluidic property, and the similar refractive index to polymer, Liquid Crystals (LCs) are one of the best candidates to provide tunability to PhC for controlling the location of bandgaps. Several approaches including external heating, applied electric/ optical field were carried out in our work.

This thesis showed our attempts to investigate light propagation through LC-PhC composite medium from linear, weakly nonlinear to nonlinear regimes. For the linear case, a band-stop filter with diverse diffraction patterns is demonstrated mainly at 633nm and 532 nm individually. By varying the temperature of external heater (22°C - 40°C), different symmetries upon filtering angles appear in the nematic and isotropic states. Polarization dependence of LC-PhC composite device is also found in the nematic phase. For the weakly nonlinear case, by adding DO3 dye into LC, the pump beam at 532 nm was first absorbed and later produced temperature gradient inside the composite after releasing heat. The diffraction patterns of the probe beam at 633nm were recorded and analyzed. For the nonlinear case, the monochromatic beam at 532 nm is used to create intensity dependent refractive index profile inside LC. We expected to observe phenomena like self-confinement or self-collimation based on the interaction between light itself and medium. The near field analysis was therefore implemented and some initial results were demonstrated.

Our work upon fabrication, simulations and measurements gives a promising vision of LC-PhC composite devices. Their rich physical properties and advantageous characteristics

open up the access to the real integrated optical systems.

4.1 Future work – controlled by deformation

According to the introduction in Section 2.1.3 and 2.4, the orientation of LCs is achieved by surface mechanical rubbing or chemical coating. In addition to these methods, the LC molecules could be aligned in a cell sandwiched with surface polymer gratings constructed by DLW lithography technique. As demonstrated in Fig 4.1.1-1, by designing the grating pattern with various tilted angles 0°, 45°, 90°, 135°, the different brightness is observed under POM. Several advanced designs such as concentric and radial gratings are also investigated as presented in Fig 4.1.1-2.

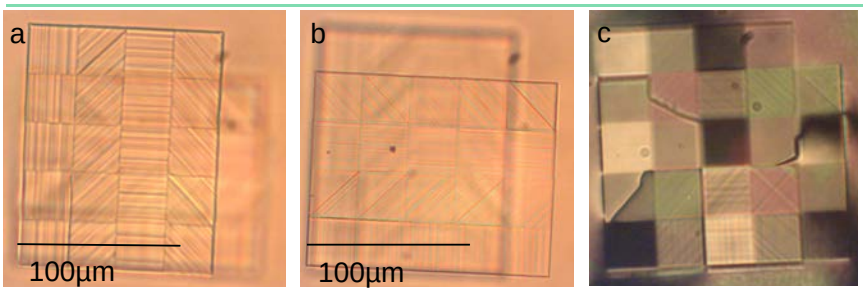

Fig. 4.1.1-1 The polymer line grating patterns on the upper (a) and the lower (b) inner surface of an empty cell. After infiltration with LC at room temperature (21°C), the various brightness change (c) under POM observation[1].

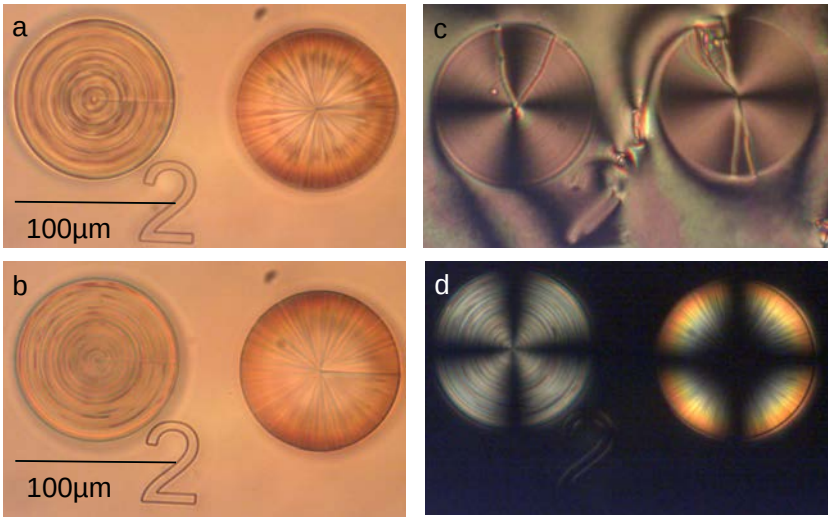

Fig. 4.1.1-2 The polymer grating arranged in concentric and radial configurations on the upper (a) and the lower (b) inner surface of an empty cell. After infiltration with LC at room temperature (21°C), the various brightness change (c) under POM observation[1]. The empty cell before infiltration (d) under POM observation.

Similar to polymer, the polymeric LCs like LCE with appealing light-induced deformation properties are also investigated. One of the main challenges for building up concrete structure with elastomer is the swelling. Although most of the LCE line structures are able to be constructed on the substrate by DLW, during the developing process they may collapse due to the swelling and shrinkage attributed to the developer solvent entering into and removing from the LCE network. Apart from the enhancement of mixing ratio with cross linker, the rigidity of LCE can also be determined by writing power and speed, i.e. the amount of exposed beam intensity and the density of dot to dot voxels. As demonstrated in Fig 4.1.1-3, based on our calibration with DLW power and speed, we could obtain the rigid LCE line structure with decent resolution (voxel width down to 0.3μm) by using writing power around 3mW under writing speed 15μm/s.

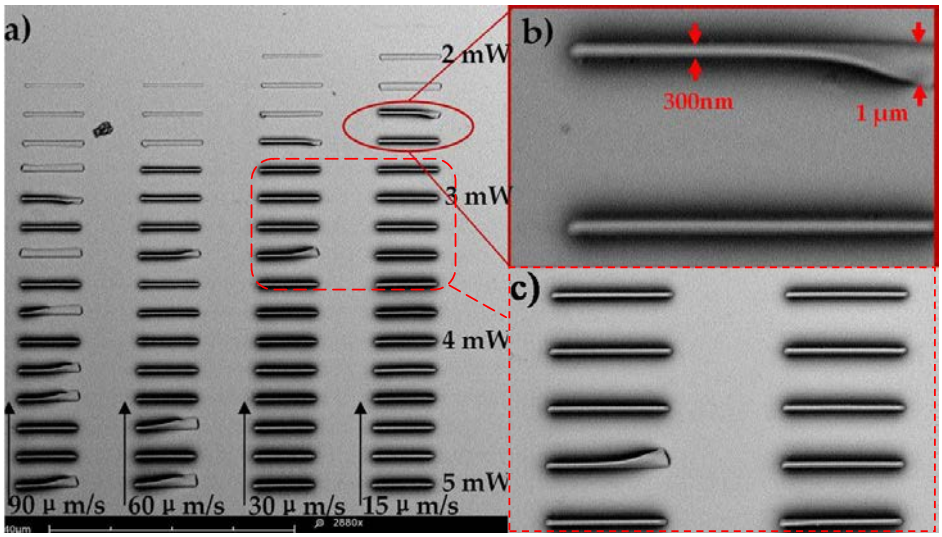

Fig 4.1.1-3 LCE structures constructed by DLW lithography technique on glass with pre-rubbed PI-130 coating. (a) the line structure is built under various power (from 1.6 mW to 5 mW) and speed (from 15μm/s to 90 μm/s) (b-c) zoom-in view of a single line with approximate voxel width and height[2].

With the previous work upon calibration of LCE structure, it gives quite promising indications to construct more complicated microstructures with elastomer. Referring to the high sensitivity on refractive index of the LC-PhC composite polymer woodpile, it is also quite feasible to extend the idea with LCE. After the elastomer woodpile is built by DLW without developing the structure, the LC-PhC hybrid elastomer sample is ready in one step process. By doping with azo-dye with absorption maximum at 530 nm in LC[2], the deformation of elastomer can be observed under 532 nm laser excitation.

The nonlinearity is further introduced by the deformation of LCE woodpile. By pre-alignment achieved with PI-1211 coating (homeotropic alignment), the LCE deformation is expected to shrink in longitudinal direction while expand in transverse direction [3]. When applying such deformation to elastomer woodpile, not only the lattice constants but also the average index within excited 532 nm laser beam cover region could be modified correspondingly. The complex nonlinear effects referring to both lattice constants and refractive indices are expected to appear in transmission.

References

[1] H. Zeng, P. Wasylczyk, G. Cerretti, D. Martella, C. Parmeggiani, and D. S. Wiersma, "Alignment engineering in liquid crystalline elastomers: Free-form microstructures with multiple functionalities," *Appl. Phys. Lett.*, vol. 106, no. 11, p. 111902, 2015.

[2] H. Zeng, D. Martella, P. Wasylczyk, G. Cerretti, J.-C. G. Lavocat, C.-H. Ho, C. Parmeggiani, and D. S. Wiersma, "High-resolution 3D direct laser writing for liquid-crystalline elastomer microstructures," *Adv. Mater.*, vol. 26, no. 15, pp. 2319–2322, 2014.

[3] A. M. Flatae, M. Burresi, H. Zeng, S. Nocentini, S. Wiegele, C. Parmeggiani, H. Kalt, and D. Wiersma, "Optically controlled elastic microcavities," *Light Sci. Appl.*, vol. 4, no. 4, p. e282, 2015.